# Circuit Model Design of Conical Transmission Line Power Combiners and Isolation of Reactive Combiners

by

Ryno Dawid Beyers

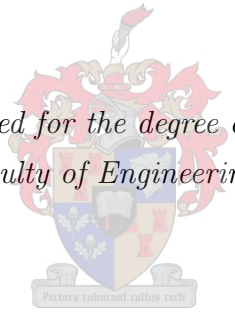

*Dissertation presented for the degree of Doctor of Philosophy in Engineering in the Faculty of Engineering at Stellenbosch University*

Department of Electrical And Electronic Engineering,
University of Stellenbosch,
Private Bag XI, Matieland, 7602, South Africa

Promotor: Dr. D. I. L. de Villiers

March 2015

# Declaration

By submitting this dissertation electronically, I declare that the entirety of the work contained therein is my own, original work, that I am the sole author thereof (save to the extent explicitly otherwise stated), that reproduction and publication thereof by Stellenbosch University will not infringe any third party rights and that I have not previously in its entirety or in part submitted it for obtaining any qualification.

R. D. Beyers: ..... Date: .....

# Abstract

*Keywords* – Combiners, Radial Combiners, Conical Combiners, $N$-way Combiners, Conical Transmission Lines, Coaxial Transmission Lines, Circuit Models, Transmission Line Transitions, Isolation

This dissertation presents a circuit-based design technique that leads to benefits in terms of the physical size, manufacturability, and flexibility in the design of $N$-way conical line power combiners. An equivalent circuit model for the peripheral input ports of conical line power combiners is extracted, as well as empirical equations that allow the circuit element values to be calculated directly from the physical dimensions of the combiner, and vice versa. This allows for rapid optimization of various dimensions of the combiner at a significantly reduced computational cost compared to full-wave simulations. A design procedure is presented and a conical combiner designed with a measured reflection coefficient of better than $-18$ dB over a 46 % bandwidth around 10 GHz. The designed prototype is much smaller compared to previous designs while exhibiting similar performance. Design procedures for single-section and multi-section impedance tapered conical to coaxial line transitions are also presented, which can be used to simplify the design of conical combiners and reduce the manufacturing effort. Two combiners are designed, one with a single-section and one with a multi-section transition, and output port reflection coefficients of $-23$ dB and $-17$ dB over bandwidths of 20 % and 43 % around 10 GHz are measured, respectively.

This dissertation additionally presents a method that can be used in general to improve the input port isolation of $N$-way power combiners without affecting their reciprocity. A simple S-parameter proof is presented, followed by a derivation of equations that can be used to estimate the worst-case performance. Some design examples are presented, showing that terminations can be used for isolation loads. A prototype based on microstrip transmission lines is manufactured and a much improved input port reflection and isolation performance of $-15$ dB and 20 dB is measured, respectively, compared to a simulated input port reflection coefficient of $-2.5$ dB and isolation of 2.5 dB before the method was applied.

# Opsomming

*Sleutelwoorde* – Kombineerders, Radiale Kombineerders, Koniese Kombineerders, $N$-rigting Kombineerders, Koniese Transmissielyne, Koaksiale Transmissielyne, Stroombaanmodelle, Transmissielynoorgange, Isolasie

Hierdie proefskrif stel 'n stroombaangebaseerde ontwerpsmetode voor wat lei tot voordele in terme van die fisiese grootte, vervaardigbaarheid, en vryheid in die ontwerp van koniese lyn kombineerders. 'n Ekwivalente stroombaanmodel vir die voerpoorte word onttrek, asook empiriese vergelykings wat gebruik kan word om die stroombaanelement waardes vanaf die afmetings van die kombineerder te bepaal. Dit laat die ontwerper toe om verskeie afmetings van die kombineerder te optimeer teen 'n beduidende laer koste in vergelyking met volgolf simulasies. 'n Ontwerpsprosedure word voorgestel en gebruik om 'n koniese kombineerder te ontwerp en 'n weerkaatskoëffisient van beter as $-18$ dB met 'n bandwydte van 46 % om 10 GHz word gemeet. Die prototipe is aansienlik kleiner as vorige ontwerpe, maar toon soortgelyke werkverrigting. Ontwerpsprosedures vir enkel en veelvoudige deel koniese na koaksiale lyn oorgange word ook voorgestel, wat gebruik kan word om die ontwerp en vervaardiging van koniese kombineerders te vereenvoudig. Twee kombineerders word ontwerp, een met 'n enkel deel oorgang en een met veelvoudige dele, en onderskeidelike uittree weerkaatskoëffisiente van $-23$ dB en $-17$ dB oor bandwydtes van 20 % en 43 % word gemeet.

Hierdie proefskrif stel ook 'n metode voor wat gebruik kan word om die intree poort isolasie van $N$-rigting kombineerders in die algemeen te verbeter, sonder om die wederkerigheid daarvan te beïnvloed. 'n Bewys van die metode word gelewer, gevolg deur 'n afleiding van vergelykings wat gebruik kan word om die slegste-geval werkverrigting af te skat. Verskillende voorbeelde van kombineerders word getoon waarop die metode toegepas is, en wys dat terminasies gebruik kan word vir die isolasie laste. 'n Prototipe gebaseer op mikrostrook transmissielyne word vervaardig en 'n verbeterde intreepoort weerkaatskoëffisient en isolasie van onderskeidelik $-15$ dB en 20 dB word gemeet, in vergelyking met 'n weerkaatskoëffisient van $-2.5$ dB en isolasie van 2.5 dB voordat die metode toegepas is.

# Acknowledgements

I would like to express my sincere gratitude to the following people and organisations:

- Dr. D.I.L. de Villiers, my promotor, for the opportunity to work on this project, his advice, support, guidance, and attention to detail.
- Dr. Werner Steyn, Prof. P.W. van der Walt and Prof. P. Meyer for their support and advice.
- Reutech Radar Systems for financial support of the project.
- Comar International for providing valuable feedback and insight on manufacturing processes.
- Wessel Croukamp and Lincoln Saunders for their advice and careful manufacturing and assembly of the prototypes.
- Everyone from the Radarlab and postgrad offices for their contributions, advice, and long conversations on random topics.
- My family and friends for encouraging me to persue my dreams and for understanding when I needed to work late into the night.

# Contents

# List of Tables

# List of Figures

# Chapter 1

# Introduction

Although conical transmission line combiners have been used for a number of decades [1], [2], detailed information on their design and performance is given for the first time in a relatively recent paper [3]. Note that reactive power combiners, such as conical types, are usually reciprocal and may therefore also be used as dividers, however, they will be referred to only as combiners throughout the dissertation for convenience. Conical combiners have many of the properties that are desired of a combiner in solid state power amplifiers (SSPAs), such as the abilities to support a large number of input devices and handle high power. A recent paper demonstrates a successful implementation using this technology by adding an impedance taper in the conical transmission line. This was needed in order to increase the spacing at the central output port for improved manufacturability, which has, unfortunately, also resulted in a significantly larger structure [4]. Some background information on power combiners will be given and the current design method for conical combiners will be discussed in more detail in Chapter 2. The first aim of this dissertation is to present a circuit-based design technique that leads to benefits in terms of the physical size, manufacturability, and flexibility in the design of conical line power combiners.

In SSPAs, the ability to tolerate the failure of multiple individual amplifiers while still producing usable output power is known as graceful degradation. The isolation between input ports of power combiners in SSPAs is an important quality that is needed in order to achieve graceful degradation as well as to prevent spurious oscillations. Isolation is also an important characteristic of combiners and dividers used in antenna array feeds. Hybrid combiners offering isolation while being able to support a large number of devices exist, however, they are generally difficult to design and manufacture and usually have limited power handling capabilities due to small spacings or isolation loads that cannot handle high power [5–10]. Although there are existing techniques that can be used to improve isolation, some of them are not applicable in general to power combiners [11],

while others, such as using isolators, have the drawback of removing the reciprocity of the device, which means that they cannot be used in, for example, transmit and receive antenna array feeds. Some background information on existing methods will be given and discussed in more detail in Chapter 3. The second aim of this dissertation is to present a new method that can be used in general to improve the input port isolation of power combiners, including reactive power combiners, without affecting their reciprocity.

## 1.1 Contributions

A circuit-based design technique is presented in this dissertation, allowing for the rapid design and optimization of conical line power combiners. This design method additionally enables the designer to set limits on the physical size of the combiner, as well as to study the sensitivity of its performance to changes in specific parameters. The presented technique is used to design a 10-way conical combiner with similar performance to previous designs, but with a significantly smaller physical size: An output port reflection coefficient of better than $-18$ dB over a bandwidth of 46% is achieved with the first manufactured prototype, which has a diameter of 49.8 mm. A design technique for a single-section impedance tapered conical to coaxial transmission line transition is presented in order to simplify the design and construction of conical combiners, and a measured output port reflection coefficient of better than $-23$ dB over a bandwidth of 20% is achieved for a 10-way combiner with a diameter of 51.8 mm. This design technique is expanded to allow for the design of a multi-section conical to coaxial line transition with more design flexibility. The expanded design technique is used to design a 10-way conical combiner with a diameter of 59.2 mm and an output port reflection coefficient of better than $-17$ dB over a bandwidth of 43% is measured.

This dissertation additionally presents a new method that can be used to improve the isolation of power combiners. This method is used to design a 4-way microstrip combiner with measured maximum input and output port reflection coefficients of better than $-15$ dB from 2.7 to 5.4 GHz, and a minimum input port isolation of better than 20 dB from 3.5 to 6 GHz and better than 25 dB from 3.7 to 5.8 GHz. The full-wave simulated maximum input port reflection coefficient and minimum input port isolation of the 4-way microstrip combiner on its own is $-2.5$ dB and 2.5 dB, respectively. This means that the new isolation method resulted in an improvement of roughly 12.5 dB in the input port reflection coefficient and up to 22.5 dB in the input port isolation.

The primary contributions of this dissertation are:

1. The development of an equivalent circuit model of shorted peripheral coaxial feeding

lines for conical transmission line power combiners [12].

2. The extraction of empirical equations that allow the equivalent circuit model element values to be calculated directly from the physical dimensions of the combiner and vice versa [13].

3. Techniques for the design of a single-section [14] and multi-section [15] impedance tapered conical to coaxial line transition.

4. A method that can be used in general to improve the input port isolation of power combiners [16].

## 1.2 Layout of the Dissertation

Some background information on conical line power combiners is given in Chapter 2, followed by the extraction of an equivalent circuit model for shorted peripheral coaxial input ports in conical combiners. Empirical equations are extracted for the circuit elements in the equivalent circuit model and a new design technique based entirely on circuit models is presented. The new design technique is validated by designing, constructing and measuring a prototype. Design techniques for single-section and multi-section impedance tapered conical to coaxial transitions are presented and validated by constructing and measuring prototypes.

Chapter 3 gives some background information on isolation techniques before describing a general method that can be used for the isolation of power combiners. A mathematical proof of the new method is given and shows that it is applicable to any power combiner. A design technique is presented, with a method to estimate the worst-case performance, and validated by completing some example designs and finally constructing and measuring a prototype.

The final chapter of the dissertation is a concluding discussion of the results obtained in Chapters 2 and 3, and future expansions that can be done on this work.

# Chapter 2

# Conical Combiners

## 2.1 Background on Power Combiners

### 2.1.1 Power Combiners in Solid State Power Amplifiers

A solid state power amplifier (SSPA) usually consists of a number of individual solid state amplifiers that are combined using a power combiner in order to overcome the limitations of the individual amplifiers. Significant technological advances have been made since the first solid state devices were combined to generate a few watts of microwave power. Recent reports show single-package Gallium Nitride (GaN) high electron mobility transistor (HEMT) amplifiers producing more than 30 W in the Ku-band [17] and more than 80 W in the X-band [18] under continuous wave (CW) operation. There are also multiple reports of GaN HEMT amplifiers with peak pulsed power outputs exceeding 100 W at X-band [19–21]. These amplifiers are relatively small ($\approx$ 20 mm$\times$20 mm) single-package devices consisting of many GaN HEMTs that are combined on a chip level. An SSPA such as in [22], which needed 208 amplifiers to produce 2 kW of CW power in the X-band, could theoretically be realised today with fewer than 40 individual amplifiers. The combination of today's high power solid state amplifiers with appropriate power combining techniques will lead to much higher power densities in SSPAs than before and increase their ability to compete with travelling wave tube amplifiers (TWTAs) and other microwave power sources.

Both the type and implementation of a power combiner in an SSPA have a significant impact on its overall performance. Not only does the combiner affect the physical size and efficiency, it also limits the maximum output power and often the number of amplifiers that can be combined. An SSPA can often exhibit the characteristic of graceful degradation in its output power if some of its individual amplifiers fail. This means that the SSPA

will still be able to produce usable output power even if some of its individual amplifiers fail. This characteristic is also attributed to the power combiner and is a very desirable feature, especially when a large number of amplifiers are combined, because it decreases the likelihood of catastrophic failure and improves reliability. It is, however, only possible to achieve graceful degradation if the individual amplifiers are sufficiently isolated from each other by the power combiner.

High power densities can be achieved by combining solid state amplifiers on a device (or chip) level in an electrically small package, as is shown in [17–21]. However, this can only be done efficiently for a limited number of devices [23]. In contrast, circuit level power combining is done using much larger structures and can be used to overcome the limitations of single chip devices to achieve even higher power levels and improved reliability.

Circuit level power combining approaches can generally be categorized as being either 2-way or $N$-way. $N$-way combiners are able to combine $N$ devices in a single step, whereas with 2-way combiners a corporate (tree) or chain (series) network is needed to combine more than two devices. Corporate and chain combiners are highly effective in many cases and usually have the advantages of being realisable using almost any transmission line medium, having matched and isolated input ports, and having well-known design procedures [23]. However, corporate and chain networks are not suitable for combining a large number of devices: With each added stage, the obtainable efficiency decreases [23, 24].

It has been shown that using a large number of amplifiers in SSPAs may be beneficial, because it can can lead to reduced phase noise and improved graceful degradation performance, and in some cases even improved overall efficiency [24]. However, the insertion loss in a corporate or chain network of combiners scales with $N$, and will therefore most likely result in inhibitive losses when a large number of amplifiers are combined. In comparison, $N$-way combiners, specifically axially symmetric types, have the ability to exhibit almost constant insertion losses with increasing $N$, and are thus better suited for combining a large number of amplifiers [7]. In addition, compared to corporate and chain combining networks with many input ports ($N > 8$), axially symmetric $N$-way combiners generally have a smaller physical size and superior amplitude and phase balance due to their structural symmetry, resulting in increased combining efficiency.

### 2.1.2 Axially Symmetric Power Combiners

Axially symmetric power combiners have input ports that are placed symmetrically around an output port, usually with equal spacings between them and at a constant radius from

the axis of symmetry. Radial, coaxial, and conical transmission lines are commonly used for the transmission medium between the input ports and output port.

Power combiners utilizing radial transmission lines have been used for a number of decades and design strategies based on electromagnetic field analysis [25], measurement techniques [26], and more recently, circuit models and full-wave optimization [7] have been proposed. Some of the notable radial power combiners found in literature include a 20-way combiner with a measured output port reflection coefficient of better than $-17$ dB over a 57 % bandwidth around 14 GHz [25], 8-way and 16-way combiners with reflection coefficients of better than $-20$ dB over 33 % and 25 % bandwidths, respectively, around 10 GHz [27], and a 30-way combiner with a reflection coefficient of better than $-13$ dB over a 25% bandwidth around 12.5 GHz [7]. Radial power combiners have successfully been used in various applications, such as in [28,29], however, the fundamental transverse electromagnetic (TEM) mode supported by a radial transmission line has a characteristic impedance that varies with radial distance and a complex input impedance when the transmission line has a finite length. This limits the performance and complicates the design, which usually requires full-wave optimization.

Coaxial transmission lines, in contrast to radial transmission lines, support a TEM mode with a constant characteristic impedance, and do not have a complex input impedance for a finite transmission line length. This means that simple transmission line theory can be used to design the impedance and size matching sections between the coaxial lines at the peripheral input ports and at the central output port. Some of the notable coaxial line power combiners found in literature include an 8-way combiner with an output port reflection coefficient of better than $-12$ dB over a 112 % bandwidth around 1.2 GHz [30], a 16-way combiner with a reflection coefficient of better than $-20$ dB over a 20 % bandwidth around 1.3 GHz [31], and the variety of coaxial line combiners in [32], including a 4-way combiner with a reflection coefficient of better than $-15$ dB over a 70 % bandwidth around 11.5 GHz.

The conical line implementation of $N$-way power combiners is a relatively new technology offering some advantages over the more conventional coaxial line and radial line structures. One advantage of conical power combiners over radial power combiners is that conical transmission lines support a TEM mode with a constant characteristic impedance versus radial distance, whereas radial transmission lines do not support a constant impedance TEM mode. Coaxial combiners also support a constant impedance TEM mode, but they have the drawback of generally having a significantly longer common path length compared to conical combiners, in order to accommodate a taper or matching sections between the larger coaxial line where the input ports are located and the smaller coaxial output port. Another drawback of coaxial combiners is that the coaxial line becomes

increasingly difficult to manufacture as the impedance is reduced to accommodate more input ports.

Even though the conical transmission line supports a fundamental TEM mode, full-wave simulations are still needed to model the conical combiner accurately, because higher order evanescent modes are excited at discontinuities in the peripheral port transitions. The design of conical combiners may therefore be time-consuming and expensive if optimization or parameter sweeps are needed, due to the relatively high computational cost of full-wave simulations. The conical combiners in [3] and [4] are designed using a hybrid technique where the number of full-wave simulations are reduced by performing circuit-based optimization on some parts of the structure. This method reduces the computational cost of designing conical combiners, but also restricts the flexibility and possibly the performance of conical combiners, because not all the parameters can be optimized together effectively.

The designs in [3] and [4] utilize a smooth constant impedance conical to coaxial transition [33] at their central output ports. This transition is challenging to manufacture for low impedances, as pointed out in [4], due to the small spacing between the inner and outer conductors of the coaxial transmission line. The solution in [4] is to increase the impedance of the transition by adding an impedance taper in the conical transmission line, resulting in improved manufacturability, but also a significantly larger structure in order to accommodate the impedance taper. Additionally, the physical specification of the profile of the impedance tapered conical line requires a large number of data points. This increases the manufacturing effort as well as the probability for errors to be made while programming the computer numerically controlled (CNC) machines.

The peripheral input port transitions in [3] and [4] utilize probes that apply an axial force to the centre conductors of the SMA connectors in order make electrical contact between the connectors and the conical transmission line. However, the axial force required to ensure proper electrical contact compromises the structural integrity of the SMA connectors and may damage them.

This chapter introduces an equivalent circuit model for shorted coaxial peripheral input lines in conical power combiners with feeding pins that are connected directly to the conical line conductor without applying any axial force. Empirical equations are presented that can be used to calculate the circuit model element values from the physical dimensions of the combiner and vice versa, allowing for the rapid design and optimization of conical power combiners without the need for any full-wave simulations. The design and manufacturing of conical combiners are further simplified by introducing an impedance tapered conical to coaxial line transition that eliminates the need for an impedance taper in the conical transmission line of the combiner.

## 2.2 Equivalent Circuit Model

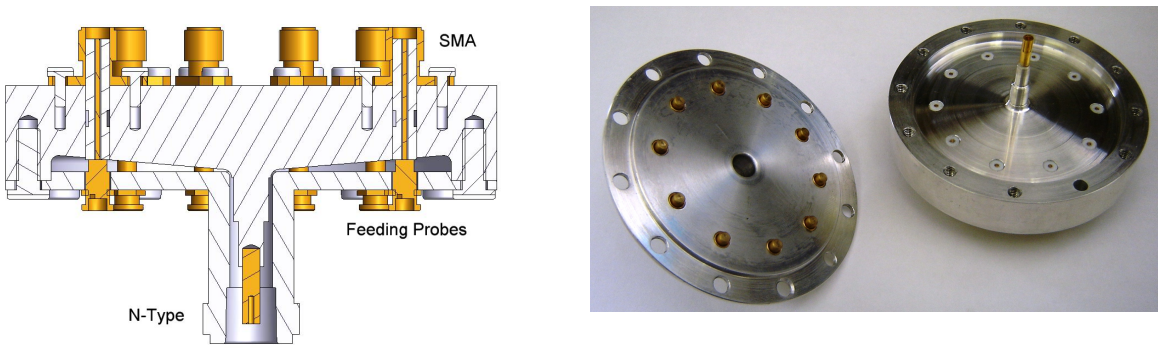


(a) (b)

Figure 2.1: A 3D CAD model of the conical combiner in [3] is shown in (a), and its constructed top and bottom halves in (b). These images are duplicated, with permission, from [34].

An example of a conical transmission line power combiner is shown in Fig. 2.1. This conical combiner utilizes tuning posts in the peripheral feeding port transitions, and has a constant 5 Ω characteristic impedance throughout the conical transmission line.

### 2.2.1 Input Port Equivalent Circuit Model

A simple yet accurate equivalent circuit model for the shorted coaxial feeding network of conical combiners is presented in this section. The circuit model is used to illustrate the effect of the tuning post in the stepped feed [Fig. 2.3(a)] by comparing its scattering parameters to the scattering parameters of the extended centre conductor feed without the tuning post [Fig. 2.3(b)]. These models may also be extended over a wide parameter range to aid in the design of other similar structures, as is done in [30] for coaxial combiners.

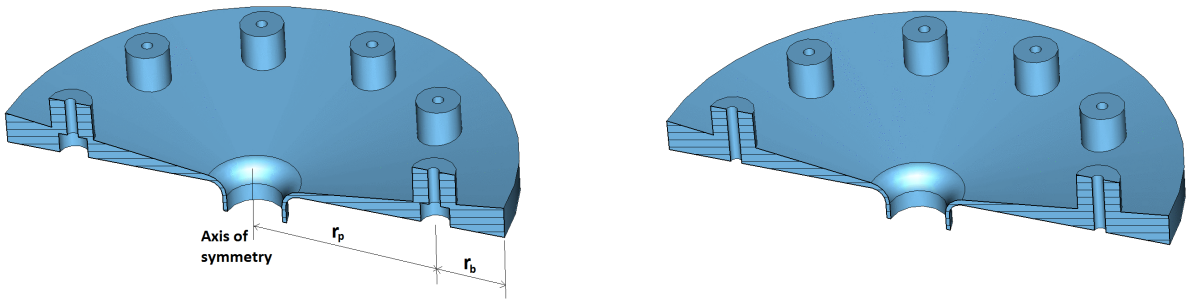


(a) (b)

Figure 2.2: 3D models of constant impedance conical combiners: (a) With tuning posts, (b) without tuning posts.

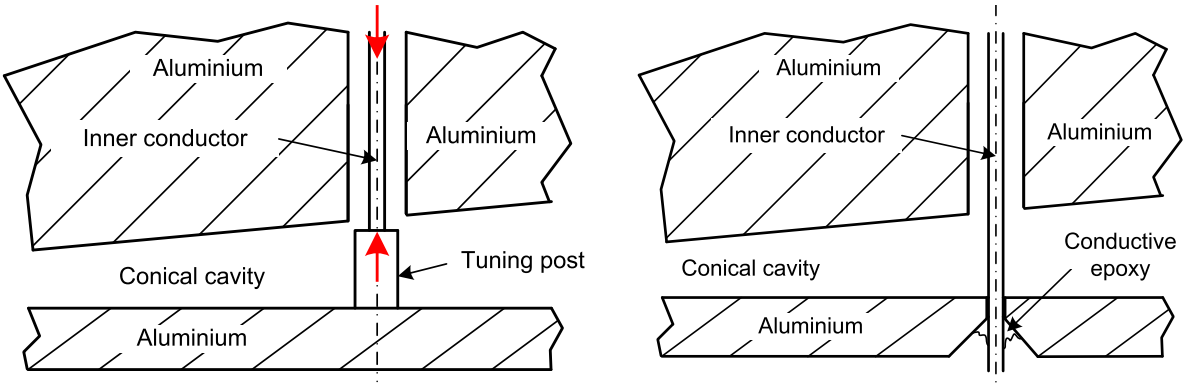


(a) (b)

Figure 2.3: Input ports of conical combiners: (a) With tuning posts, (b) without tuning posts. The red arrows in (a) indicate the axial forces needed to create electrical contact between the centre conductor of the SMA connector and the tuning post.

A design method based on circuit theory and full-wave simulations is presented in [3], where ideal stepped impedance coaxial transmission line sections are added to the output and input ports of the full-wave simulated S-parameter block of the conical combiner and optimized using a circuit simulator. Even though undesired higher order modes may propagate in larger conical transmission lines, as pointed out in [35] and is the case in both [3] and [4], this design method can still be used, since the higher order modes are taken into account in the full-wave simulation of the combining structure. However, unless the higher order modes are explicitly modelled, a circuit model representation of the entire combining structure is expected to be valid only when the combiner is operating in the TEM mode, and thus where the ratio

$$\frac{r_{max}}{r_{cutoff}} \leq 1, \tag{2.1}$$

with

$$r_{max} = r_p + r_b. \tag{2.2}$$

In (2.2), $r_p$ is the peripheral port placement radius, $r_b$ is the back-short length as shown in Fig. 2.2(a), and

$$r_{cutoff} = Nr_b/\pi, \tag{2.3}$$

as defined in [35]. The ratio in (2.1) describes the maximum size of the combiner that the circuit model is expected to model accurately. Additionally, the circuit model that is presented here is only valid for the symmetrically driven case, where the fields at all of the input ports have the same amplitude and phase, because the unsymmetrical modes are not TEM modes [36, 37].

An equivalent circuit model is extracted for a combiner similar to the design in [3], but

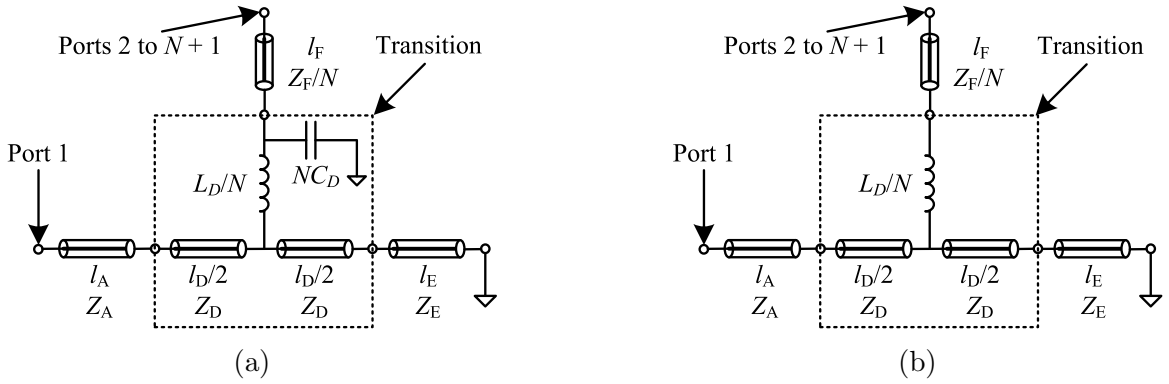


Figure 2.4: Equivalent circuit models for conical combiners: (a) With tuning posts, (b) without tuning posts.

with 80 Ω air-filled coaxial peripheral input ports, as is used in [4], and an increased conical line impedance of 8 Ω in order to maintain a constant impedance throughout the structure. Since $r_p = 25$ mm in [3] results in $r_{max} \,/\, r_{cutoff} \approx 1.36$, the size is reduced slightly to $r_p = 20$ mm ($r_{max} \,/\, r_{cutoff} \approx 1.15$) for a more accurate circuit model representation. Note that the condition in (2.1) is still not satisfied, however, accurate results are still obtained due to the gradual cutoff exhibited by conical transmission lines [38]. The final structure is shown in Fig. 2.2(a) with a cutplane to show the tuning posts in the peripheral input port transition. Fig. 2.3(a) shows the peripheral port transition using tuning posts, where the forces required to create a reliable electrical contact between the centre conductor of the SMA connector and the tuning post are indicated using red arrows. These forces may damage the SMA connectors. The combiner in Fig. 2.2(b) is identical to the combiner in Fig. 2.2(a), except that the centre conductors of the coaxial input ports are extended to make electrical contact with the bottom conductor of the conical transmission line instead of using tuning posts. The centre conductors are fixed to the conical line conductor from the outside using conductive epoxy, as shown in Fig. 2.3(b). This method does not apply any axial force to the centre conductor pin of the coaxial input ports.

#### 2.2.1.1 Equivalent Circuit Model Extraction

In the circuit diagrams shown in Fig. 2.4, the circuit elements inside the dotted boxes labelled with the subscript D represent the peripheral port transition into the conical transmission line. The rest of the elements represent the coaxial and conical transmission line sections: The subscript A is used for the central coaxial line, the smooth conical to coaxial transition [33] and the conical line up to where the peripheral coaxial lines are inserted; the transmission line labelled E is the back-short; and the peripheral coaxial input lines are labelled F.

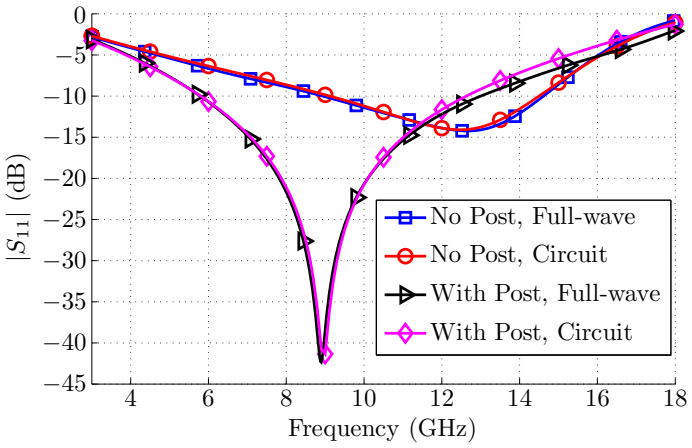


Figure 2.5: The output port reflection coefficients ($S_{11}$) of the circuit models and full-wave simulations of conical combiners with and without tuning posts at the input ports.

The transition from the parallel combination of the peripheral input ports (ports 2 to $N+1$) into the conical transmission line is modelled by a series inductor, a shunt capacitor, and two short transmission line sections. The two short transmission line sections model the effect of removing some of the conical line conductor where the coaxial lines are inserted, as shown in Fig. 2.10. This effectively increases the characteristic impedance of the conical line in the vicinity of the feeding pins. The series inductor models the stored evanescent mode energy at the transition and is strongly dependent on the feeding pin length. The effect of the stepped feeding post in the peripheral input port transition of the combiner shown in Fig. 2.2(a) is modelled by a shunt capacitor as shown in Fig. 2.4(a). A similar equivalent circuit model in Fig. 2.4(b) is used for the combiner shown in Fig. 2.2(b) without the tuning posts, the only difference being that the shunt capacitor is removed.

The equivalent circuit models are extracted by fitting the central output port (Port 1) reflection coefficient of the models onto the reflection coefficients calculated by full-wave simulations. Close agreement between full-wave simulations and measurements on similar combiners is reported in [3] and [4]. Agreement to within 1 dB between the full-wave and circuit model reflection coefficients is shown for both combiners in Fig. 2.5, confirming the validity of the presented circuit models.

#### 2.2.1.2 Feeding Network Inductance

The obtained element values for the circuits in Fig. 2.4 are listed in Table 2.1. The tuning posts reduce the inductance in the circuit model by more than a factor 10 and improve the reflection coefficient, and thus also the transmission coefficient, of the combiner. A similar effect is observed in larger combiners where the size may be increased to the point where higher order modes may begin to propagate within the operating band, as is done in [4].

Table 2.1: A summary of extracted element values for the equivalent circuits.

| Value | With Post | | No Post | |
|---|---|---|---|---|
| $l_A$ | 16 | mm | 16 | mm |
| $Z_A$ | 8 | Ω | 8 | Ω |
| $l_D$ | 3.69 | mm | 3.69 | mm |
| $Z_D$ | 8.125 | Ω | 8.125 | Ω |
| $L_D$ | $0.43 \times 10^{-10}$ | H | $7.1 \times 10^{-10}$ | H |
| $C_D$ | $4.63 \times 10^{-14}$ | F | — | |
| $l_E$ | $7.5 - l_D/2$ | mm | $7.5 - l_D/2$ | mm |
| $Z_E$ | 8 | Ω | 8 | Ω |
| $l_F$ | 5 | mm | 5 | mm |
| $Z_F$ | 80 | Ω | 80 | Ω |

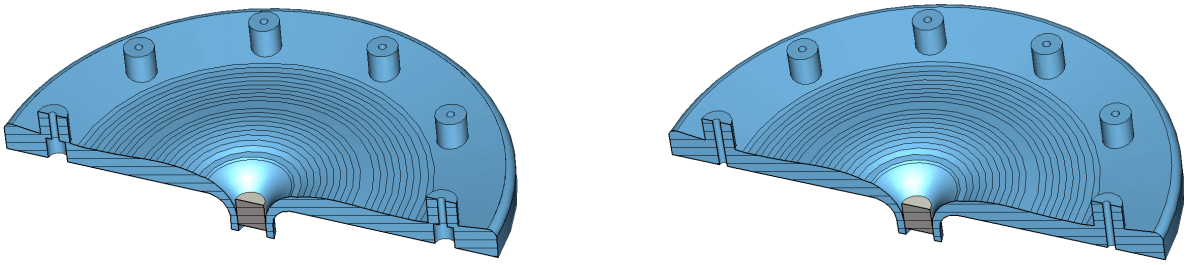

(a) (b)

Figure 2.6: 3D models of electrically large conical combiners with tapered conical lines: (a) With tuning posts, (b) without tuning posts.

Fig. 2.6 shows two variations of the combiner in [4] without any external coaxial matching networks: one with tuning posts in the peripheral input port transition [Fig. 2.6(a)] and one without [Fig. 2.6(b)]. The peripheral input coaxial lines have an impedance of 80 Ω and transition into an 8 Ω conical line. The conical line impedance is tapered up to 25 Ω near the centre using a Klopfenstein [39] taper and transition into a 25 Ω output coaxial line.

The full-wave simulated reflection coefficient of the central output port ($S_{11}$) is shown in Fig. 2.7, where a good impedance match for the combiner with tuning posts is observed around 10 GHz. The full-wave simulated reflection coefficient for the combiner without tuning posts is also shown in Fig. 2.7 with a deteriorated central port reflection coefficient. Even though the full circuit model may not strictly be valid for these oversized conical combiners, the same effect as with the smaller combiners is observed for the feeding network without the tuning post. The capacitance introduced by the tuning posts tunes out the inductance in the circuit model, and improves the reflection coefficient of the combiner. Note that the reflection coefficient of the uncompensated electrically large conical combiner in Fig. 2.6(b) is worse when compared to the smaller combiner in Fig. 2.2(b). This is due to the dependence that the series inductance in the circuit model has on

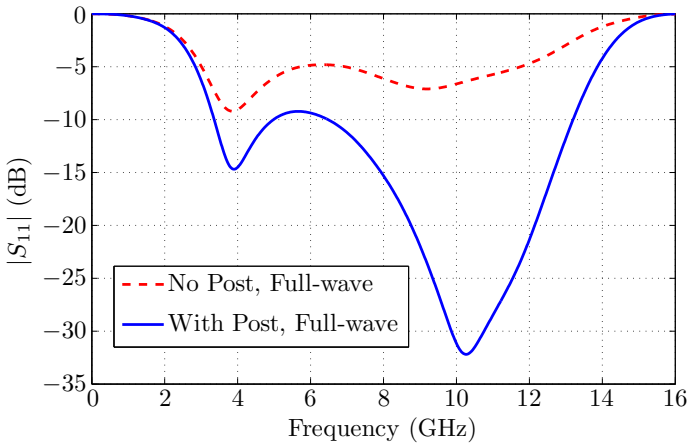


Figure 2.7: The output port reflection coefficients ($S_{11}$) of the full-wave simulations of the combiners shown in Fig. 2.6.

the feeding pin length, and the fact that the feeding pin is much longer in the oversized combiner ($\approx 4.2$ mm) when compared to the smaller combiner ($\approx 2.7$ mm).

#### 2.2.1.3 Conclusion

The presented equivalent circuit model shows that the tuning posts in the feeding networks of conical line power combiners effectively reduce the inductance of the extended centre conductors. However, the tuning posts complicate the construction of the combiner and compromise the structural integrity of the input SMA connectors due to the axial force required to create electrical contact between the centre conductor pins and the tuning posts. Although the widest bandwidth may be achievable by using a tuning post due to its proximity to the problem area, other methods may be used where the inductance is not reduced, but rather compensated for in a different part of the combiner at the potential cost of some bandwidth. This work (Section 2.2.1) has been peer-reviewed and accepted for oral presentation at an international conference, and is published in [12].

### 2.2.2 Empirical Equations

The equivalent circuit model presented in the previous section may be used to aid in the design of conical combiners, similar to the method used in [30] for a coaxial combiner, by optimizing the circuit model and performing parameter sweeps to find the equivalent physical dimensions of the combiner. However, this may be difficult in conical combiners, since the distance between the conical line conductors is dependent on their angles as well as radial distance from the axis of symmetry, compared to coaxial lines where it is only dependent on the inner and outer conductor radii. The distance between the transmission

line conductors is significant due to the dependence that the inductance in the model has on the feeding pin length.

Equivalent circuit models have previously been used to model different parts of various types of combiners, including in some cases the peripheral port transitions, but not in conical combiner types. Most of these circuit models do not offer a means to relate the circuit element values to physical dimensions [30, 40], or they are not accurate enough to be used exclusively and full-wave optimization or parameter sweeps are still needed afterwards to obtain the final dimensions of the structures [3, 4, 7, 41, 42]. The reactive elements in the equivalent circuit models introduced in Section 2.2.1 are similar to other models that have been used to model the stored evanescent mode energy in similar types of transmission line transitions or transmission lines with similar discontinuities [43, 44]. The two short transmission line sections in the equivalent circuit model that model the removal of some of the conical line conductor, as well as the empirical equations introduced in this section, are new contributions.

A set of general empirical equations based on full-wave simulations, which describe the equivalent circuit model for shorted coaxial peripheral feeding ports as presented in the previous section, is presented in this section. The empirical equations allow the designer to determine the equivalent circuit element values accurately and directly from the physical dimensions of conical combiners and vice versa. In many cases the empirical equations are accurate enough to allow the circuit model to be used exclusively during the design process, eliminating the need for full-wave analyses. This allows for rapid optimization of various dimensions of the combiner at a significantly reduced computational cost compared to full-wave optimization together with matching networks that may be required for wide band operation. This method also enables the designer to minimize the total transmission length and thus the physical size of the combiner.

#### 2.2.2.1 Physical Description and Empirical Equation Extraction

The circuit model presented in the previous section is extended by subdividing the combiner into more regions. The region containing the peripheral port transition, region D, remains unchanged. The basic layout of a conical combiner is shown in Fig. 2.8(a), where the different regions that will be used in the circuit model description are indicated by dotted boxes. Note that the figure is rotationally symmetric around the vertical axis on the left. The equivalent circuit model for the combiner and the location of external matching networks that may be added is shown in Fig. 2.8(b), where the equivalent circuit for each region of the combiner is contained within its corresponding box. The peripheral feeding port transition used here is the version without tuning posts, as defined in the

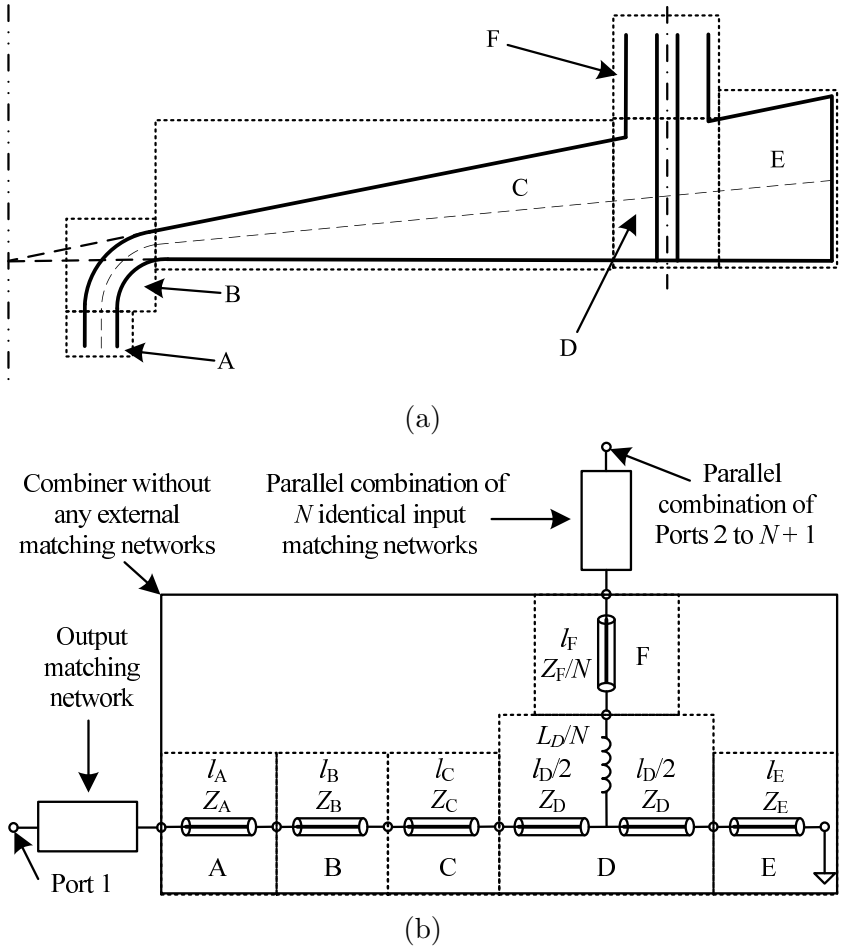


Figure 2.8: (a) A cut plane view of the combiner showing how it is divided into regions, and (b) the circuit model of the whole combiner with the regions corresponding to (a)

previous section, and is different from what is used in [3] and [4]. Note that the circuit model is only valid for the symmetrically driven case where the fields at the peripheral input ports have the same amplitude and phase.

In Fig. 2.8, regions A and F are coaxial lines, regions C and E are conical lines, and region B is a constant impedance conical to coaxial line transition, as shown in Fig. 2.9, and presented in [33]. These regions are all simple TEM transmission lines and can thus be modelled by ideal transmission lines with lengths and impedances derived from the physical geometry of the structure, whereas region D includes some reactive elements to compensate for the stored evanescent mode energy around the peripheral coaxial feeding port to conical line transition. Note that the transmission line in region F and the inductor in region D represent a parallel combination of $N$ of those components for an $N$-way combiner.

A complete and accurate physical description of the combining structure is required so that the transmission line lengths and impedances needed for the circuit model extraction

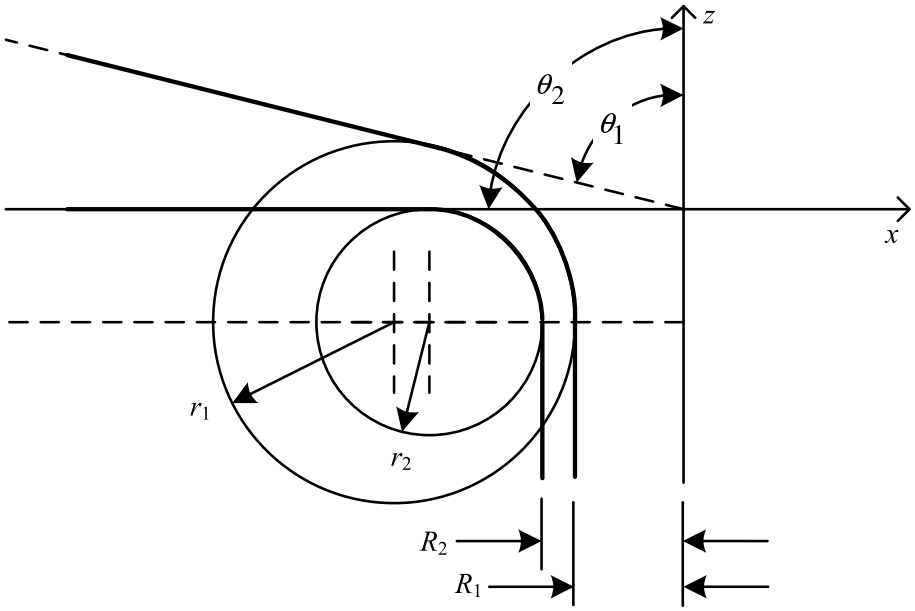


Figure 2.9: A smooth constant impedance conical to coaxial transmission line transition.

as well as the circuit model based design procedure can be calculated. The equations describing regions A, B, C, E and F will be given, followed by the extraction process for the empirical equations for region D. Note that no external matching networks are used during the extraction process.

1. **Central Output Coaxial Line (Region A):**
   Region A contains a constant impedance coaxial line with inner and outer conductor radii of $R_1$ and $R_2$, respectively. The coaxial line in region A will have the same length $l_A$ as used in the ideal transmission line model. The impedance $Z_A$ can be calculated using
   $$Z_A = 60\ln\left(\frac{R_2}{R_1}\right). \tag{2.4}$$

2. **Central Transition (Region B):**
   The central transition from conical to coaxial line is designed using the smooth transition presented in [33] and shown in Fig. 2.9. The radii of the two arcs ($r_1$ and $r_2$) used to construct the transition are obtained using
   $$r_2 = 3.5 \times (R_2 - R_1), \tag{2.5}$$
   $$r_1 = \frac{R_1\cos\theta_{1B} + r_2\sin\theta_{1B}}{1 - \cos\theta_{1B}}, \tag{2.6}$$
   where $\theta_{1B}$ is the conical line angle as defined in Fig. 2.9. The mean transmission

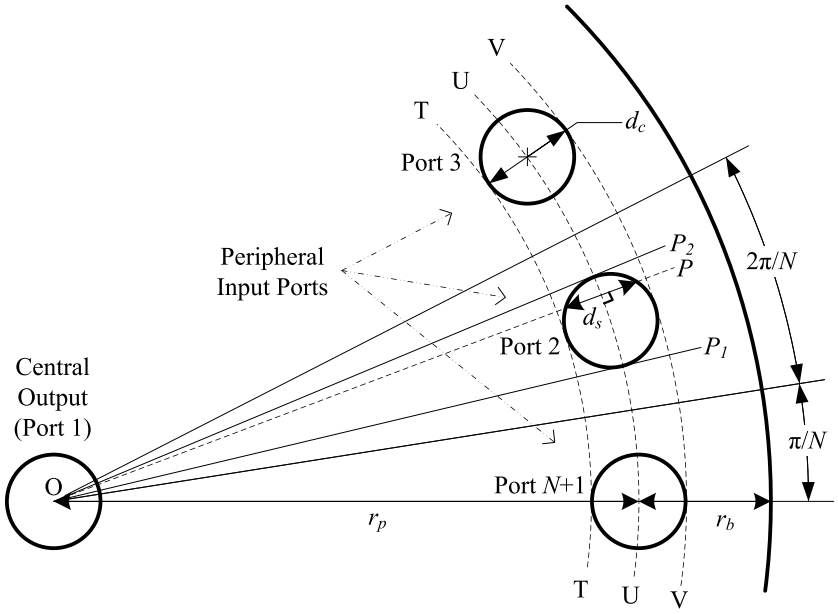


Figure 2.10: A sector of the combining structure showing the parts of the top conductor being removed where the coaxial lines are placed, as well as the port numbering used throughout this work.

length – the dashed line in region B, Fig. 2.8(a) – can be calculated using

$$l_B = \frac{r_1 + r_2}{2} \times \frac{\theta_{2B} + \theta_{1B}}{2}, \tag{2.7}$$

where $\theta_{2B}$ is the conical line angle as defined in Fig. 2.9, and usually $\theta_{2B} = 90°$. A more general version of this transition is presented in Section 2.3.1, and expanded in Section 2.3.2. The impedance of the transition is shown to be constant in [33] and can be determined by calculating either the coaxial or conical transmission line impedances:

$$Z_B = Z_A = 60 \ln\left(\frac{R_2}{R_1}\right), \tag{2.8}$$

or

$$Z_B = 60 \ln\left[\frac{\cot(\theta_{1B}/2)}{\cot(\theta_{2B}/2)}\right], \tag{2.9}$$

for air-filled coaxial and conical lines, respectively.

3. **Conical Transmission Line (Region C):**
The mean transmission length for this region is calculated from the edge separating regions D and C to the edge separating regions C and B. The length – the dashed line in region C, Fig. 2.8(a) – can be calculated using

$$l_C = \frac{r_p}{\cos\left(\pi/4 - \theta_{1D}/2\right)} - l_n - \overline{d_s}/2, \tag{2.10}$$

where

$$l_n = \frac{1}{2}\left[R_1 + R_2 + r_2 + r_1\left(1 - \cos\theta_{1B}\right)\right] \tag{2.11}$$

is the average length of conical transmission line removed from the central part of the conical line where the transition to the central coaxial line is inserted. In (2.10) $r_p$ is the peripheral input port placement radius as defined in Fig. 2.10, $\overline{d_s}$ is the arithmetic mean of $d_s$ in Fig. 2.10 as the line $OP$ is moved from the position $OP_1$ to $OP_2$ and can be approximated using (2.16). The same definition as in region B is used for $\theta_{1D}$ except that it is the angle of the conical line in region D. The conical line angles need to be defined as separate variables for each region, since they may generally have different impedances and thus different angles, as is the case, for example, in [4]. The length $l_C$ is exact when region C is a constant impedance conical line, where $\theta_{1B} = \theta_{1D}$, and is a reasonable approximation if region C is an impedance tapered conical line, where $\theta_{1B} \neq \theta_{1D}$. If region C is a constant impedance conical line, then $Z_C = Z_B$, since $\theta_{1B} = \theta_{1D}$ and $\theta_{2B} = \theta_{2D} = 90°$. If region C is an impedance tapered conical line then the conical line angle $\theta_{1C}$ required to realize the desired impedance function $Z_f$ versus distance can be approximated as a function of radial distance from the axis of symmetry of the conical line $\rho$, using

$$\theta_{1C}(\rho) = 2\arctan\left[\frac{\tan(\theta_{2B}/2)}{e^{Z_f(\rho - l_n)/60}}\right]. \tag{2.12}$$

The impedance function $Z_f$ can be an impedance taper of the designer's choice, such as an exponential or a Hecken [45] taper.

4. **Conical Transmission Line (Region E):**
The length – the dashed line in region E, Fig. 2.8(a) – can be calculated using

$$l_E = \frac{r_b}{\cos\left(\pi/4 - \theta_{1D}/2\right)} - \overline{d_s}/2, \tag{2.13}$$

where $r_b$ is the back-short length as defined in Fig. 2.10. The impedance $Z_E$ can be calculated using

$$Z_E = 60\ln\left[\frac{\cot(\theta_{1D}/2)}{\cot(\theta_{2D}/2)}\right], \tag{2.14}$$

since $\theta_{1D} = \theta_{1E}$ and $\theta_{2D} = \theta_{2E}$.

5. **Coaxial Transmission Line (region F):**
Region F contains a constant impedance coaxial line with an inner conductor radius $r_{inner}$ and an outer conductor diameter of $d_c$. The coaxial line in region F will have the same length $l_F$ as used in the ideal transmission line model. The impedance $Z_F$

can be calculated using

$$Z_F = 60\ln\left(\frac{d_c}{2r_{inner}}\right). \tag{2.15}$$

6. **Empirical Equation Extraction (region D):**
The length $l_D$ in the circuit model is calculated directly from the combiner dimensions, whereas empirical equations will be used to calculate the impedance $Z_D$ and inductance $L_D$. The empirical equations are extracted so that they are applicable to a wide range of conical line combiners.

A sector of an $N$-way combiner is shown in Fig. 2.10 where the dimensions used to derive the expression for the length $l_D$ are defined. The outer conductors of the peripheral ports are formed by drilling holes through one of the conical transmission line conductors and are represented by the circles between the dashed arcs T and V.

The drilling of the holes results in the removal of some of the conical line conductor, causing a change in impedance between arcs T and V. The change in impedance is approximated using two short transmission lines. It is assumed that $r_p$ is large relative to the outer conductor diameter of the peripheral coaxial lines $d_c$, so that the arc U will be approximately straight inside the removed circle area. As a result, the average of $d_s$ and thus the length $l_D$, can be approximated simply by using

$$l_D = \overline{d_s} = \frac{d_c\pi}{4}. \tag{2.16}$$

The value of $Z_D$ is calculated by scaling the impedance of the conical transmission line to model the effect of removing some of the conductor from the conical line. This modification is expected to increase the impedance of the conical line between arcs T and V, resulting in a scaling factor for $Z_D$ that is larger than 1. Furthermore, the value of $Z_D$ is expected to be dependent on the ratio of the amount of conductor along the circumference of the conical line at radius $r_p$ before the holes are made to the amount remaining after the holes are made. This ratio is defined as $x_1$, so that the empirical equation for $Z_D$ can be defined as

$$Z_D = g_1(x_1)Z_{sys}, \tag{2.17}$$

where

$$x_1 = \frac{2\pi r_p}{2\pi r_p - N\overline{d_s}} = \frac{r_p}{r_p - \frac{Nd_c}{8}}, \tag{2.18}$$

$Z_{sys}$ is the impedance of the unperturbed conical line between arcs T and V before the peripheral ports are inserted ($Z_{sys} = Z_E$), and $N$ is the number of peripheral

feeding ports of the combiner.

The inductor in region D models the extended centre conductor pin of the peripheral coaxial lines and its value is expected to be dependent on the pin length. Thus,

$$L_D = g_2(x_2), \tag{2.19}$$

where

$$x_2 = r_p \cot\theta_{1D} \tag{2.20}$$

is the length of the coaxial pin extending into the conical transmission line.

A simple constant impedance conical combiner as shown in Fig. 2.11 is used to extract the empirical equations that describe $Z_D$ and $L_D$. This is done by fitting the scattering parameters of the circuit model onto the corresponding ones produced by full-wave simulations. All full-wave simulations are performed using the time domain solver in Computer Simulation Technology (CST) Microwave Studio (MWS) [46]. A mean square error function is defined in order to measure how well the model matches the full-wave simulations:

$$\varepsilon = \sum_{k=1}^{K} \frac{1}{K} |S_{11}^f(f_k) - S_{11}^c(f_k)|^2 \ . \tag{2.21}$$

$S_{11}^f$ and $S_{11}^c$ are the S-parameters of the full-wave and circuit simulations, respectively, and $f_k$ is the $k$th frequency sample of a total of $K$ samples. Port 1 is the central port and ports 2 to $N+1$ are the peripheral ports, as defined in Fig. 2.10. A Nelder-Meade based Simplex search [47] is used to minimize $\varepsilon$ over a wide bandwidth ($> 100\%$) around a chosen centre frequency by adjusting the values of $Z_D$ and $L_D$ in the circuit model. The centre frequency is determined by the length of the back-short in the conical line $r_b$ (also defined in Fig. 2.10), which is equal to a quarter wavelength at that frequency. A centre frequency of 10 GHz is used to extract the empirical equations. First order polynomials fit the resulting values of $Z_D$ and $L_D$ well, however, the coefficients of the best fitting functions change for different peripheral port dimensions. A first order polynomial is thus

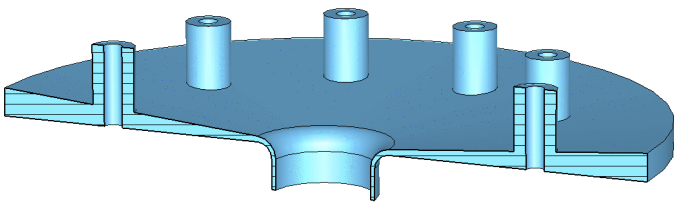

Figure 2.11: The constant impedance 10-way conical combiner used to extract the model. The shaded part of the model is vacuum and the background material is perfect electrical conductor (PEC).

Table 2.2: Extracted Polynomials For The Empirical Equations

| Function | Units |
|---|---|
| $g_1(x_1, \Delta r) = -0.054x_1\Delta r + 0.48x_1 + 0.072\Delta r + 0.38$ | $\Omega/\Omega$ |
| $g_2(x_2, \Delta r) = 62x_2\Delta r + 320x_2 - 230\Delta r - 5.7$ | pH |

fitted to each set of data points sharing the same peripheral port dimensions, resulting in a number of different equations. These equations are combined by fitting polynomials to the obtained coefficients for different peripheral port dimensions versus $\Delta r$, with

$$\Delta r = d_c/2 - r_{\text{inner}}, \tag{2.22}$$

where $r_{\text{inner}}$ is the inner conductor radius, and $d_c$ is the outer conductor diameter of the peripheral coaxial feeding ports. This normalization is chosen, because the effect of removing some of the conical line conductor as well as the feeding pin inductance is expected to be dependent on the spacing between the inner and outer conductors of the coaxial input lines. The resulting empirical equations are the simple bivariate polynomials given in Table 2.2. Note that all dimensions should be specified in millimetres.

### 2.2.3 Parameter Study

A parameter study is performed to test the accuracy of the model. Equivalent circuit models for various combiners are built using the information presented in Section 2.2.2 (a detailed design procedure is given in Section 2.2.4). Combiners with centre frequencies of 6 GHz (C-Band) and 10 GHz (X-Band) and input ports with the same inner and outer conductor radii as the standard 50 Ω 3.5 mm and N-type connectors are used to generate the data shown in Fig. 2.12. A combiner with 85.6 Ω input ports with the same inner conductor radius as the standard SubMiniature version A (SMA) connector is also used, similar to what is used in [4], with a different outer conductor radius from the standard 50 Ω SMA connector. Each contour plot in Fig. 2.12 was generated using data from more than 200 full-wave simulations. The parameters $Z_{sys}$, $Z_F$, $N$, $r_p$, and $r_b$ in Fig. 2.12 are defined in Section 2.2.2.

The error function defined in (2.21) is used to show how well the scattering parameters of the circuits match their corresponding full-wave simulations for different combiner dimensions over a larger than 100% bandwidth. These contour plots may be of interest to the designer when using the model. The need for full-wave simulations can be eliminated by limiting the combiner dimensions to regions where $\varepsilon$ is small, however the model could still serve well as a coarse model for space mapping techniques [48] in situations where

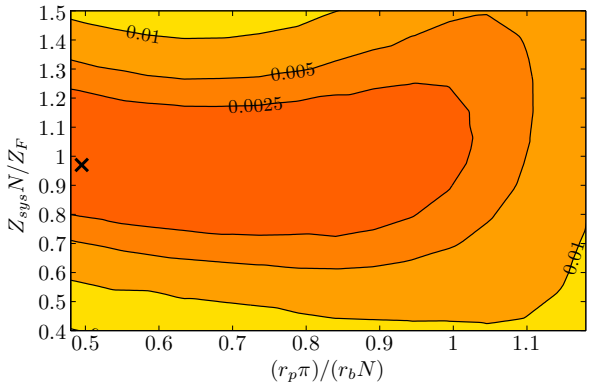


(a) 10 GHz (X-Band) combiners with 3.5 mm peripheral ports.

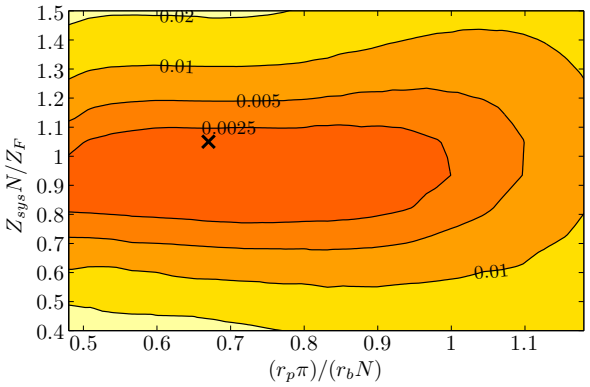


(b) 10 GHz (X-Band) combiners with 85.6 Ω peripheral ports.

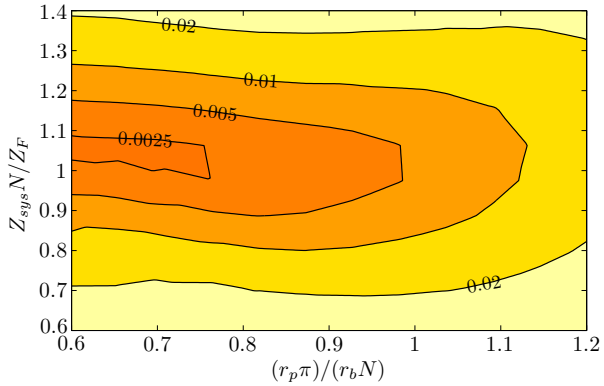


(c) 10 GHz (X-Band) combiners with N-type peripheral ports.

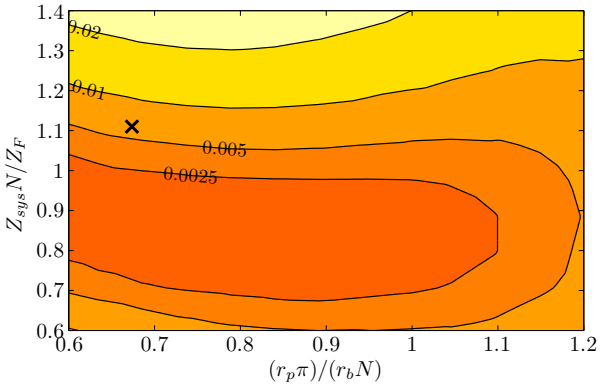


(d) 6 GHz (C-Band) combiners with N-type peripheral ports.

Figure 2.12: Contour plots of the mean square error, as defined in (2.21), between full-wave simulations and their equivalent circuit models. The accuracy of the circuit models used for the designs in Section 2.2.5 are indicated by ×-markers on the contour plots: The 30 port X-Band combiner is shown in (a), the 10 port X-Band combiner in (b) and the 15 port C-Band combiner in (d).

the combiner dimensions cannot be limited to the higher accuracy regions, or when the results are not satisfactory.

Fig. 2.12 has been generated using data for 10-way combiners. However, similar data for 15-way and 20-way combiners with 85.6 Ω SMA feeding ports has been generated and compared to the data for $N = 10$. A statistical analysis of the data reveals that the model accuracy is relatively independent of $N$: The mean error function variance for the three values of $N$ is

$$\mathrm{Var}(\varepsilon)_{\mathrm{mean}} = 3.19 \times 10^{-7}, \tag{2.23}$$

and the maximum error function variance is

$$\mathrm{Var}(\varepsilon)_{\mathrm{max}} = 1.42 \times 10^{-5}. \tag{2.24}$$

A comparison of the results for combiners with N-type input ports operating at X-Band [Fig. 2.12(c)], where $d_c/r_b \approx 0.9$, and at C-Band [Fig. 2.12(d)], where $d_c/r_b \approx 0.5$, shows that the electrical size of the peripheral ports influences the accuracy of the circuit model: The region with higher accuracy ($\varepsilon < 2.5 \times 10^{-3}$) is much larger at C-Band than at X-Band. The same effect can be seen by comparing Figs. 2.12(a) and 2.12(c), which are for combiners with the same centre frequency, but with different peripheral port sizes. As a general rule, the outer conductor diameter of the peripheral ports should be less than a quarter of a wavelength at the centre frequency, thus $d_c/r_b < 1$, and increased accuracy is expected for smaller diameters.

### 2.2.4 Design Procedure

The physical description, equivalent circuit model, empirical equations, and parameter study presented in Sections 2.2.1, 2.2.2, and 2.2.3 are used to compile a step-by-step design procedure so that the designer may use the presented information in a systematic way. The number of input ports $N$, the wavelength at the centre frequency of the operating band $\lambda_c$, and the type of connectors to be used for the peripheral input ports and central output port should be selected before starting the design procedure. The first part of the design consists of setting up initial values and/or constraints for the parameters that can be optimized. The optimizable parameters are all either physical dimensions or can be directly related to physical dimensions of the combiner. The parameter study performed in Section 2.2.3 is used to create a set of recommendations that will assist the designer in obtaining more accurate results. The second part of the design consists of optimizing the equivalent circuit model for one or more design goals. When satisfactory results are obtained, the design can be verified by constructing a 3D model of the combiner and performing a single analysis using full-wave simulation software such as CST MWS.

#### 2.2.4.1 Recommended initial values or constraints for optimizable parameters

1. For the back-short length $r_b$, it is recommended that

$$r_b \approx \frac{\lambda_c}{4}, \tag{2.25}$$

   since the back-short will present an open circuit a quarter wavelength away, at the input port transitions.

2. For the outer conductor diameter $d_c$, of the peripheral input coaxial lines it is

recommended that

$$d_c < r_b, \tag{2.26}$$

because this will result in a more accurate equivalent circuit model representation of the transition. It also needs to be taken into account that the coaxial lines modelled by region F need to interface with matching networks or – if the matching networks are omitted – directly with the input connectors. Calculate the resulting values for $Z_F$ using $d_c$ and the radius of the inner conductor $r_{inner}$ that will be used for the peripheral input ports using (2.15).

3. It is recommended, in general, that for the impedance of the unperturbed conical line in region D, as described in Section 2.2.2.1,

$$Z_{sys} \approx \frac{Z_F}{N}. \tag{2.27}$$

This will result in a more accurate equivalent circuit model representation of the transition.

4. For the peripheral input port placement radius $r_p$, improved accuracy of the circuit model can be obtained, in general, when

$$r_p < \frac{N r_b}{\pi}, \tag{2.28}$$

while also keeping $r_p$ large enough to accommodate all of the input connectors for ports 2 to $N + 1$.

5. The outer conductor radius $R_2$ of the coaxial line in region A should be selected based on the fact that this coaxial line will need to interface either directly with the chosen output connector or with an output matching network.

6. The inner conductor radius $R_1$ of the coaxial line in region A also affects the conical to coaxial line transition in region B, since $Z_A = Z_B$. Furthermore, if region C is a constant impedance conical line, then $Z_A = Z_B = Z_C = Z_{sys} = Z_E$. However, using a constant impedance conical line in region C may lead to manufacturing difficulties and inaccuracies due to the small spacing $(R_2 - R_1)$ that is required in order to realize a low impedance coaxial transmission line, as pointed out in [4]. It is thus recommended to use a tapered conical line in region C that tapers the impedance from $Z_{sys}$ up to a higher impedance in regions A and B, resulting in a larger spacing and thus improved manufacturability. In this case, $R_1$ should be chosen or optimized and constrained to provide adequate spacing, and $r_p$ will affect the taper length.

#### 2.2.4.2 Calculation of equivalent circuit model element values

The equivalent circuit model of the entire combining structure, as shown in Fig. 2.8(b), can now be constructed in a circuit simulator. Fig. 2.8(b) shows the location of external matching networks, for example stepped impedance coaxial lines, that may be added. The designer will need to find or derive the equivalent circuit models for any added external matching networks needed for a specific combiner design. Circuit element values of the equivalent model can now be calculated using the parameters described in Section 2.2.4.1 as variables, by using the following procedure:

1. Calculate $Z_B$ from (2.8).
2. Calculate $\theta_{1B}$ using (2.9) where typically $\theta_{2B} = 90°$.
3. $l_B$ can be calculated using (2.7).
4. $l_A$ can be optimized together with an external output matching network, or if region A is already matched to the desired output port impedance and dimensions, $l_A$ can be zero.
5. $Z_A = Z_B$.
6. $l_C$ can be calculated using (2.10).
7. If region C is a constant impedance conical line then $Z_C = Z_B$, otherwise the profile of the desired impedance taper, such as an exponential or a Hecken [45] taper, with a length of $l_C$ can be approximated using (2.12).
8. Calculate $\Delta r$ using (2.22).
9. $l_D$ can be calculated using (2.16).
10. $Z_D$ can be calculated by combining (2.17), (2.18), and the function $g_1(x_1, \Delta r)$ listed in Table 2.2.
11. Calculate $\theta_{1D}$ using (2.14) where typically $\theta_{2D} = 90°$.
12. $L_D$ can be calculated by combining (2.19), (2.20), and the function $g_2(x_1, \Delta r)$ listed in Table 2.2.
13. $l_E$ can be calculated using (2.13).
14. $Z_E = Z_{sys}$, and thus with $\theta_{2E} = \theta_{2D}$, $\theta_{1E} = \theta_{1D}$.
15. $l_F$ can be optimized together with an external input matching network, or if region F is already matched to the desired input port impedance and dimensions, $l_F$ can be zero.

16. $Z_F$ can be calculated using (2.15).

The entire circuit model including external matching networks and an impedance tapered conical line in region C can now be optimized for one or more chosen design goals.

### 2.2.5 Design Examples

The circuit model is further validated by completing some example designs with external input and output matching networks and comparing the S-parameters of the model with the full-wave simulations. Three different combiners are designed with stepped impedance central coaxial ports to match them to 50 Ω, similar to the combiner in [3], using [49] to calculate the step capacitances. In each of the combiners, the impedance of the conical lines are tapered up to higher values near the central port, as is done in [4], except that a smooth Hecken taper [45] is used instead of a Klopfenstein taper [39]. These examples also serve as an indication of how well the circuit model S-parameters match the full-wave simulations for combiners that fall into different accuracy regions as shown in Fig. 2.12 and explained in section 2.2.3. The starting parameters for each design example, before being optimized to the final design parameters, are obtained using the recommendations and constraints described in Section 2.2.4.

The first design is for an X-Band 30-way combiner, with a centre frequency of 10 GHz, that has 50 Ω peripheral ports with the same inner conductor radius as the standard 3.5 mm connector. The 3D model used for the full-wave simulation is shown in Fig. 2.13(a), and a difference of less than 2 dB between the circuit model and full-wave simulation is shown in Fig. 2.13(b). This level of accuracy is achieved by limiting the combiner dimensions to the higher accuracy and thus lower error regions as indicated by the ×-marker in Fig. 2.12(a). The final parameters of the optimized combiner are: $R_2 = 3.5$ mm, $Z_A = Z_B = 20\ \Omega$, $l_A = 0$ mm, $Z_E = Z_{sys} = 1.61\ \Omega$, $d_c = 3.5$ mm, $r_{inner} = 0.76$ mm, $r_p = 38.7$ mm,

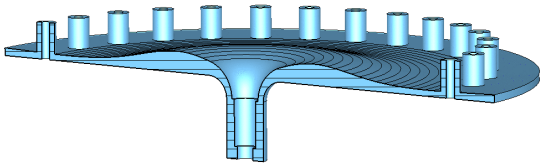

(a)

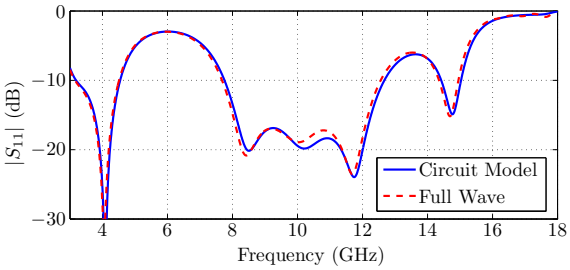


(b)

Figure 2.13: (a) The full-wave simulation model of the 30-way X-Band combiner with standard 3.5 mm connector dimension peripheral ports, and (b) the comparison between the full-wave and equivalent circuit model output port reflection coefficients ($S_{11}$).

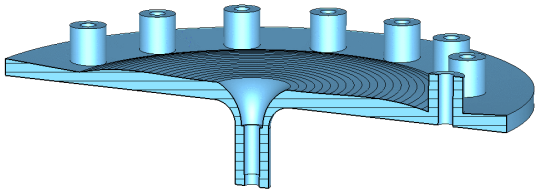

(a)

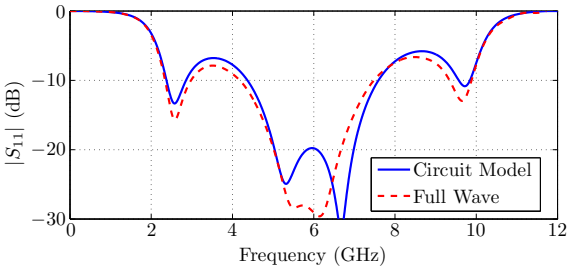


(b)

Figure 2.14: (a) The full-wave simulation model of the 15-way C-Band combiner with standard N-type connector dimension peripheral ports, and (b) the comparison between the full-wave and equivalent circuit model output port reflection coefficients ($S_{11}$).

$r_b = 8.1$ mm, $Z_F = 50\ \Omega$. The stepped coaxial output matching network has an impedance level of 32.46 Ω, and a length of 7.6 mm, followed by a 50 Ω coaxial line. The Hecken taper in region C has $B = 5.78$, with $B$ defined in [45].

The second design is for a C-Band 15-way combiner, shown in Fig. 2.14(a), with a centre frequency of 6 GHz and 50 Ω peripheral ports with inner conductor radii corresponding to the standard N-type connector dimensions. A comparison between the circuit model and full-wave simulation results is shown in Fig. 2.14(b), with slightly deteriorated but still relatively good agreement considering that this combiner falls into a much lower accuracy region [see Fig. 2.12(d)] compared to the previous design. This example demonstrates that the model is valid for a different frequency range. The final parameters of the optimized combiner are: $R_2 = 3.5$ mm, $Z_A = Z_B = 27\ \Omega$, $l_A = 0$ mm, $Z_E = Z_{sys} = 3.7\ \Omega$, $d_c = 7$ mm, $r_{inner} = 1.52$ mm, $r_p = 40.2$ mm, $r_b = 12.5$ mm, $Z_F = 50\ \Omega$. The stepped coaxial output matching network has an impedance level of 46.56 Ω, and a length of 9.4 mm, followed by a 50 Ω coaxial line. The Hecken taper in region C has $B = 0 + j0.9280$, with $B$ defined in [45].

The third design is for an X-Band 10-way combiner, with a centre frequency of 10 GHz, that has stepped impedance peripheral ports with a constant inner conductor radius equal to that of the standard SMA connector. The peripheral ports are stepped into a 65.4 Ω partially-filled coaxial transmission line followed by a 85.6 Ω section that transitions into the conical transmission line, as shown in Fig. 2.15(a). This is similar to the peripheral ports used in [4], but without the tuning post to compensate for the feeding pin inductance. The stepped impedance feeding lines add degrees of freedom, namely the lengths of the 65.4 Ω ($l_{par}$) and 85.6 Ω ($l_F$) lines, that can be optimized. The impedance step introduces a small shunt capacitance in the external matching network that can be omitted due to its small effect. The central port reflection coefficient ($S_{11}$) is shown in Fig. 2.15(b) and the circuit model is in agreement to within 2 dB with the full-wave simulation over most

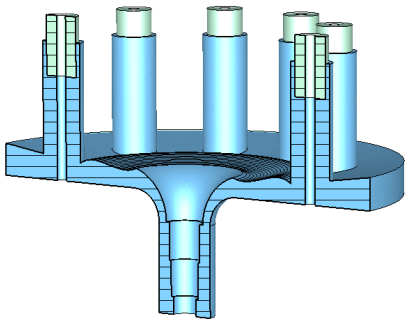

(a)

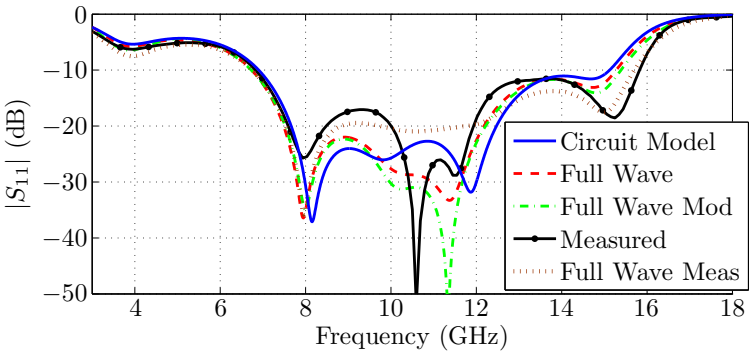


(b)

Figure 2.15: (a) The full-wave simulation model of the 10-way X-Band combiner with standard SMA connector dimension peripheral ports, and (b) the comparison between the circuit model, full-wave, modified full-wave and measured output port reflection coefficients ($S_{11}$). The full-wave simulated $S_{11}$ using the measured physical profile of the manufactured combiner (shown in Fig. 2.16) is also shown in (b).

of the band, and within 8 dB where the reflection coefficient is below −22 dB. For this design $r_p + r_b = 25.9$ mm compared to $r_p + r_b = 40$ mm in [4], while exhibiting similar performance. The reduction in size is mainly due the fact that the impedance taper in the conical line no longer needs to be designed as in [4], where the taper length is maximized in order to achieve the best possible reflection coefficient in the passband. This was required since the combining structure, and thus the taper, was not included in the optimization parameter space since full-wave analysis was used to find the response. The circuit model approach used here allows the taper to be optimized together with the impedance levels and transmission line lengths throughout the entire combiner, and it can consequently have a shorter length. The final parameters of the optimized combiner are: $R_2 = 3.5$ mm, $Z_A = Z_B = 20.18\ \Omega$, $l_A = 0$ mm, $Z_E = Z_{sys} = 9\ \Omega$, $d_c = 5.164$ mm, $r_{inner} = 0.62$ mm, $r_p = 17$ mm, $r_b = 7.9$ mm, $Z_F = 85.6\ \Omega$, $l_F = 9.5$ mm, $l_{par} = 4$ mm. The stepped coaxial output matching network has impedance levels of 32.89 Ω and 38.62 Ω, and lengths of 4.4 mm and 4.2 mm, in that order, followed by a 50 Ω coaxial line. The Hecken taper in region C has $B = 0 + j2.47$, with $B$ defined in [45]. This design is chosen for construction and measurement.

### 2.2.6 Construction and Measurement

A CNC lathe is usually able to machine conical structures, such as conical transmission lines, with ease. There are, however, a few limitations that need to be considered. The finite radius of the cutting tool tip limits the size of the smallest concave feature of the structure. The tool tip radius is taken into account by blending all concave corners with a radius equal to or larger than the tip radius. For this design, this modification has very little effect on the combiner performance, since the tip radius (0.4 mm in this case) is much smaller than the guided wavelength at X-Band ($\lambda_g \approx 30$ mm). Additionally, all the areas in the combiner requiring this modification have relatively low local field intensities, further reducing its effect. The full-wave simulation results of the modified combiner in Fig. 2.15(b) show that while these modifications significantly reduce the manufacturing effort, the combiner performance is barely affected at all. For full-wave simulation purposes, the physical profile of the impedance taper in the conical line is defined by a series of coordinates connected by short straight lines, whereas for construction purposes, the profile is much more conveniently defined by a series of tangential circle sections passing through or near the series of coordinates. The specification of the physical profile of the impedance tapered conical line was changed to tangential circle sections as a last step before manufacturing and there was no need to recalculate the S-parameters, since the two representations matched very closely.

The size, shape, and angle of the cutting tool holder and/or toolpost that is used impose limitations on the realizable shape of the structure. The goal is to use the least number of different cutting tools, since each interchanging of tools increases the cost and introduces a degree of uncertainty, as well as visible and often palpable step discontinuities. If necessary, it is desirable to change the cutting tool at a large radius in this type of structure, since any discontinuities or uncertainties will have less of an effect where the energy is spatially more dispersed. The shape and angle of the cutting tool also influence the amount of effort needed during fabrication and whether a certain shape is realisable at all. For example, if the structure has a profile that does not increase or decrease monotonically in height versus radius, as is the case with the chosen design example, the cutting tool needs to be sufficiently narrow and its holder appropriately shaped so that it has enough clearance of the rest of the structure at all times.

The physical profile of the machined part is measured using a Coordinate Measuring Machine (CMM) and compared to the 3D CAD model dimensions in Fig. 2.16 showing excellent agreement with the design. The largest errors can be seen in the coaxial to conical transition and the impedance taper in the conical line. A photo of the manufactured top and bottom halves of the combiner is shown in Fig. 2.17.

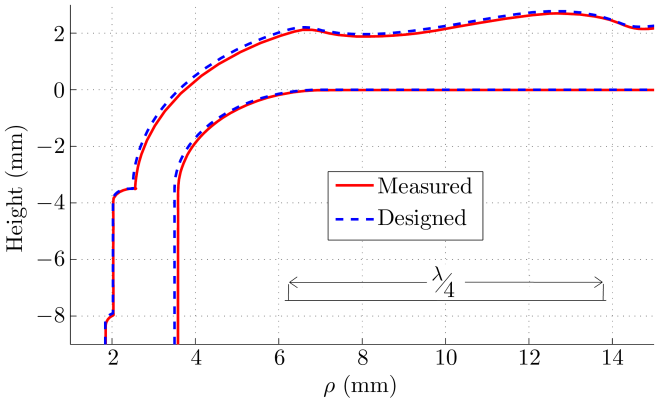


(a)

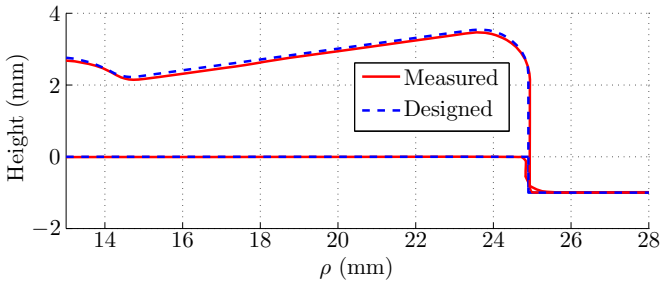


(b)

Figure 2.16: The measured profile of the manufactured device is compared to the CAD model dimensions in (a) and (b). The scale in (a) is shown for a quarter wavelength at 10 GHz.

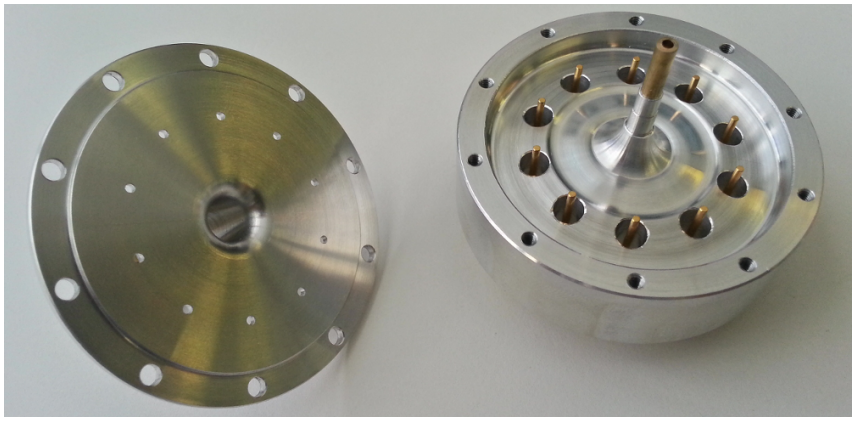

Figure 2.17: A photo of the manufactured top and bottom halves of the combiner.

The measured central port reflection coefficient is shown in Fig. 2.15(b) and the difference between the simulated and measured results is less than 3 dB over most of the operating band, and less than 8 dB where the reflection coefficients are below −10 dB. A full-wave simulation is performed using the measured dimensions of the manufactured combiner and the resulting central port reflection coefficient is shown in Fig. 2.15(b). The remaining difference between the measured and simulated $S_{11}$ could be due to a number of factors,

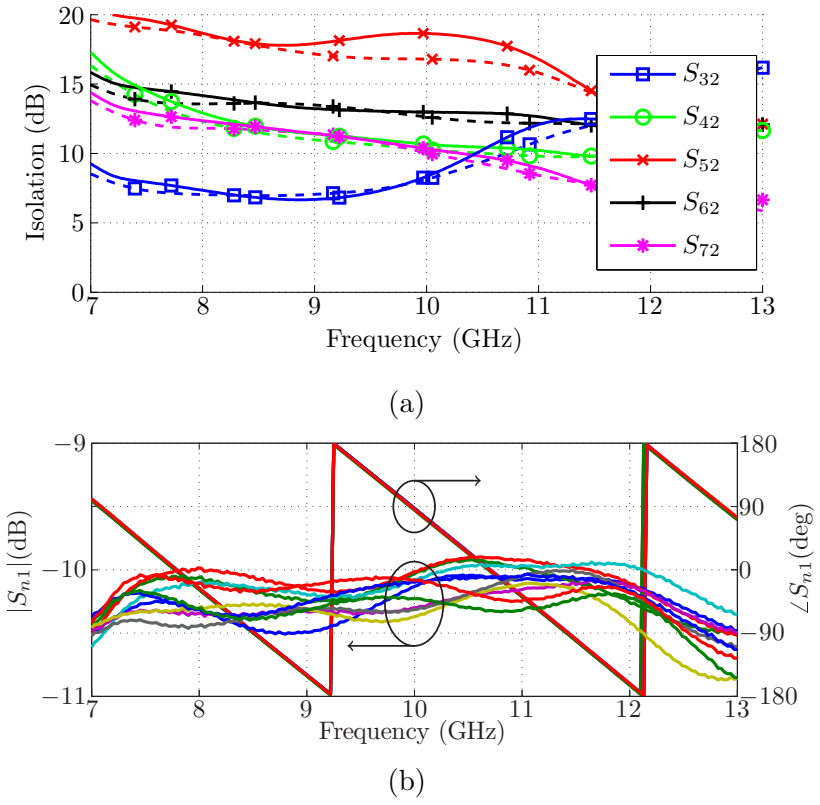


Figure 2.18: (a) The full-wave simulated isolation (dashed lines) compared to the measured isolation (solid lines) of the combiner in its operating band. The measured phase and amplitude balance is shown in (b), where $n$ is the peripheral port number with $n = 2, ..., N + 1$.

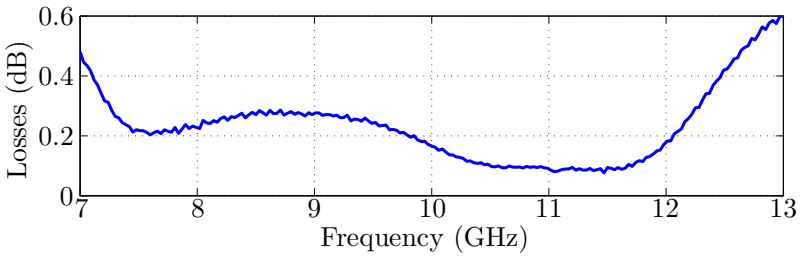


Figure 2.19: The total insertion loss of the combiner.

such as the SMA to N-type adaptor, which was not taken into account during calibration, or the non-ideal SMA terminations used during the measurements. The SMA terminations used for these measurements have reflection coefficients of no better than −25 dB, and the N-type to SMA adaptor a reflection coefficient of no better than −26 dB according to its datasheet. The central port return loss and fractional bandwidth is shown in Table 2.3 for comparison with other work. The measured peripheral port isolation, shown in Fig. 2.18(a) is better than 6 dB compared to roughly 6 dB in [4] and 5 dB in [3]. The maximum measured amplitude and phase imbalance, shown in Fig. 2.18(b) is ± 0.6 dB

Table 2.3: Comparison With Other Recent Work

| Ref. | Type | N | Return Loss (dB) | Bandwidth | Frequency Band |
|---|---|---|---|---|---|
| This Work | Conical | 10 | 18 | 46% | X-Band |
| [4] | Conical | 10 | 18.5 | 47% | X-Band |
| [3] | Conical | 10 | 14.7 | 74% | X-Band |
| [7] | Radial | 30 | 14 | 15% | Ku-Band |
| [29] | Radial | 10 | 15 | 35% | Ku-Band |
| [30] | Coaxial | 8 | 12 | 112% | L-Band |
| [41] | Coaxial | 10 | 15 | 30% | Ku-Band |

and $\pm$ 3°, respectively, versus $\pm$ 0.7 dB and $\pm$ 5° in [4], and $\pm$ 1.5 dB and $\pm$ 10° in [3]. The insertion loss, shown in Fig. 2.19, is calculated by substituting the measured values for $S_{j1}$, $j = 2, 3, ..., N + 1$ into

$$Losses = -10\log_{10}\left(\sum_{j=2}^{N+1} |S_{j1}|^2\right). \tag{2.29}$$

The maximum insertion loss in the operating band is 0.28 dB, which is the same as in [4], and an improvement compared to [3], where a stepped impedance matching network is used.

### 2.2.7 Conclusion

A simple equivalent circuit model is presented, with empirical equations, allowing for rapid circuit-based design and optimization of conical combiners with shorted coaxial input ports, without the need for any full-wave simulations, whereas previous methods all required full-wave simulations. The results of a parametric study on the accuracy of the circuit model are presented in a format that may be helpful to the designer. The effectiveness of the circuit model is demonstrated by using it to design a significantly smaller combiner with performance comparable to previously published designs. The work in Sections 2.2.2 to 2.2.6 is published in the IEEE Transactions on Microwave Theory and Techniques [13].

## 2.3 Impedance Tapered Conical to Coaxial Line Transition

### 2.3.1 Single-Section Transition

A smooth conical to coaxial transition with a constant characteristic impedance, capable of handling a much higher peak power compared to sharp cornered transitions, was presented for the first time in [33]. The smooth transition has subsequently been used successfully in the design of conical line power combiners [3], [4].

The conical combiner designed in [3] is difficult to manufacture due to the small spacing between the inner and outer conductors at the centre of its conical line, and additionally has a limited peak power handling capability due to its stepped matching sections at the central output port, as pointed out in [4]. These problems are addressed in [4], resulting in a design with improved power handling and manufacturability, at the cost of additional design complexity and an increase in the size of the combiner.

A method is presented here for designing and determining the resulting impedance taper of a conical to coaxial line transition similar to the one presented in [33], except that the conical and coaxial lines may now have different impedances. When they have different impedances, an impedance taper is formed that provides a match between the conical and coaxial lines. This transition can be used to significantly simplify the design of conical combiners by replacing the tapered conical line section, constant impedance transition, and the coaxial matching sections of previous designs by a single component.

A combiner is designed with the new transition using the circuit model presented in Section 2.2.1 for the peripheral feeding ports together with empirical equations presented in Section 2.2.2. This allows the entire combiner to be designed and optimized using circuit theory. When compared to the previous designs, this design can be manufactured with significantly reduced effort, since the transition has a relatively large spacing between the inner and outer conductors and is defined by two arcs with constant radii, compared to the smaller spacings and many dimensions needed to define the tapered conical line and coaxial matching sections.

#### 2.3.1.1 Analysis and Design Equations

The transition is formed by two arcs with constant radii, as shown in Fig. 2.20. Note that Fig. 2.20 is rotationally symmetric around the $z$-axis. An arc with radius $r_1$ joins the conical line conductor defined by $\theta_{1,1}$ with the coaxial inner conductor, and an arc with

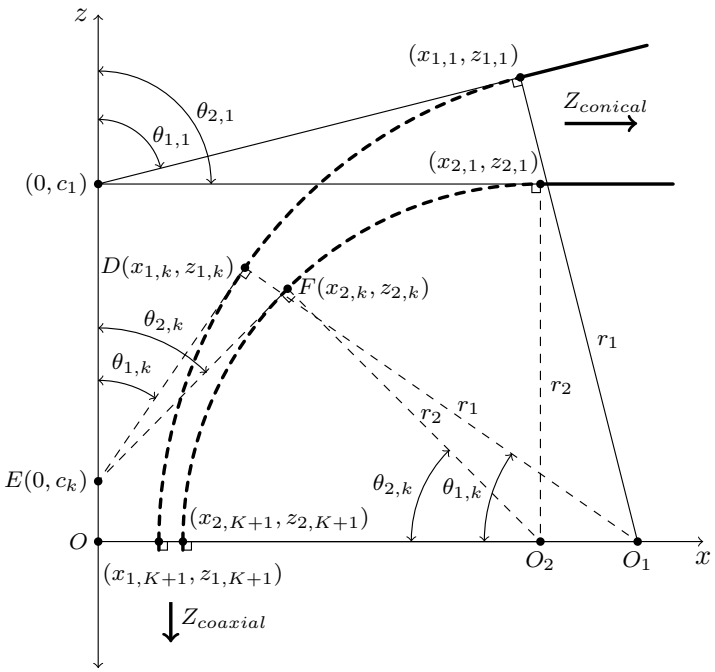


Figure 2.20: A sketch of the profile of the conical to coaxial transition.

radius $r_2$ joins the conical line conductor defined by $\theta_{2,1}$ with the coaxial outer conductor. The transition is divided into $K$ sections, with

$$\theta_{2,k} = \frac{k}{K+1}\theta_{2,1}, \quad k = 0, 1, ..., K+1, \tag{2.30}$$

in order to calculate the impedance throughout the transition along the constant radius arcs. An auxiliary conical line with conductors tangential to the arcs that form the transition, as indicated by the dashed lines $DE$ and $FE$ in Fig. 2.20, is constructed for each $\theta_{2,k}$. From the definition of a conical line, the two lines representing its two conductors must cross at the same point on its axis of symmetry, in this case $E(0, c_k)$. The equations for lines $DE$ and $FE$ can be combined by rearranging them to make $c_k$ the subject. This leads to

$$c_k = -x_{1,k}\cot\theta_{1,k} + z_{1,k} = -x_{2,k}\cot\theta_{2,k} + z_{2,k}. \tag{2.31}$$

Using (2.31) and setting

$$x_{1,k} = x_{1,K+1} + r_1(1 - \cos\theta_{1,k}), \tag{2.32}$$

$$z_{1,k} = z_{1,K+1} + r_1\sin\theta_{1,k}, \tag{2.33}$$

$$x_{2,k} = x_{2,K+1} + r_2(1 - \cos\theta_{2,k}), \tag{2.34}$$

$$z_{2,k} = z_{2,K+1} + r_2\sin\theta_{2,k}, \tag{2.35}$$

results in

$$r_1\left[\sin\theta_{1,k} - \cot\theta_{1,k}\left(1-\cos\theta_{1,k}\right)\right] = r_2\left[\sin\theta_{2,k} - \cot\theta_{2,k}\left(1-\cos\theta_{2,k}\right)\right] + x_{1,K+1}\cot\theta_{1,k} - x_{2,K+1}\cot\theta_{2,k}. \tag{2.36}$$

This can be simplified using an identity for half-angle cotangents and written in the form

$$(a^2+b_k^2)\sin^2\theta_{1,k} + 2r_1 b_k \sin\theta_{1,k} + (r_1^2 - a^2) = 0, \tag{2.37}$$

with

$$a = x_{1,K+1} + r_1, \tag{2.38}$$

and

$$b_k = \cot\theta_{2,k}[x_{2,K+1} + r_2(1-\cos\theta_{2,k})] - r_2\sin\theta_{2,k}. \tag{2.39}$$

Equation (2.37) can be solved for $\theta_{1,k}$ using

$$\theta_{1,k} = \arcsin\left[\frac{-2r_1 b_k \pm \sqrt{4r_1^2 b_k^2 - 4(a^2+b_k^2)(r_1^2-a^2)}}{2(a^2+b_k^2)}\right]. \tag{2.40}$$

Since $\theta_{1,k}$ has multiple possible answers, the appropriate one must be chosen: If the problem is set up as in Fig. 2.20, $0° < \theta_{1,k} \leq \theta_{1,1}$.

Once $\theta_{1,k}$ is known for each corresponding $\theta_{2,k}$, which can be determined beforehand using (2.30), the characteristic impedance of each section of conical line along the transition can be calculated using

$$Z_k = 60\ln\left[\frac{\cot(\theta_{1,k}/2)}{\cot(\theta_{2,k}/2)}\right]. \tag{2.41}$$

Note that for the last section where $\theta_{2,k} = 0°$, $c_k \to -\infty$ and in the limit the conical line becomes a coaxial line. The impedance for the last section should thus be calculated using

$$Z_k = 60\ln\left(\frac{x_{2,K+1}}{x_{1,K+1}}\right) \tag{2.42}$$

instead of (2.41). The transmission length $l_k$ of each section can be approximated using

$$l_k = \frac{\overline{r}}{2}\left[(\theta_{1,k+1} + \theta_{2,k+1}) - (\theta_{1,k} + \theta_{2,k})\right], \tag{2.43}$$

with

$$\overline{r} = \frac{1}{2}\left(r_1 + r_2\right). \tag{2.44}$$

Equations (2.38) - (2.44) can be used to determine the impedance taper of the transition after it has been designed. As a test, a constant impedance taper is designed using the

information in [33] and the impedance level throughout the transition calculated using (2.38) - (2.44), and it is found that the impedance does indeed remain constant throughout and equal to the coaxial and conical lines on either side of the transition.

The design equations for the impedance tapered transition are derived by substituting the initial conical line angles $\theta_{1,1}$ and $\theta_{2,1}$, as well as the coaxial line inner and outer conductor radii, $x_{1,K+1}$ and $x_{2,K+1}$ into (2.36). Simplifying after performing the substitution results in an equation describing the relationship between $r_1$ and $r_2$:

$$r_1 = ABr_2 + A(C - D), \tag{2.45}$$

with

$$A = \cot(\theta_{1,1}/2), \tag{2.46}$$
$$B = \tan(\theta_{2,1}/2), \tag{2.47}$$
$$C = x_{1,K+1}\cot\theta_{1,1}, \tag{2.48}$$

and

$$D = x_{2,K+1}\cot\theta_{2,1}. \tag{2.49}$$

Equation (2.45) implies that either $r_1$ or $r_2$ can be chosen. Alternatively, the total transmission length of the transition $l_t$ can be chosen using

$$\overline{r} = \frac{l_t}{\overline{\theta}}, \tag{2.50}$$

with

$$\overline{\theta} = \frac{1}{2}\left(\theta_{1,1} + \theta_{2,1}\right), \tag{2.51}$$

substituting $\overline{r}$ into (2.44), and solving simultaneously with (2.45) for $r_1$ and $r_2$. In short, if the total length $l_t$ is chosen, $r_2$ can be found using

$$r_2 = \frac{2\overline{r} - A(C - D)}{1 + AB}, \tag{2.52}$$

and afterwards $r_1$ can be found by substituting $\overline{r}$ and $r_2$ into (2.44) and rearranging.

#### 2.3.1.2 Transition Taper Characteristics

It can be shown that (2.45) can be reduced to (2.6) if the impedances of the conical and coaxial transmission lines are chosen to be equal. Setting $x_{1,K+1} = R_1$, $x_{2,K+1} = R_2$,

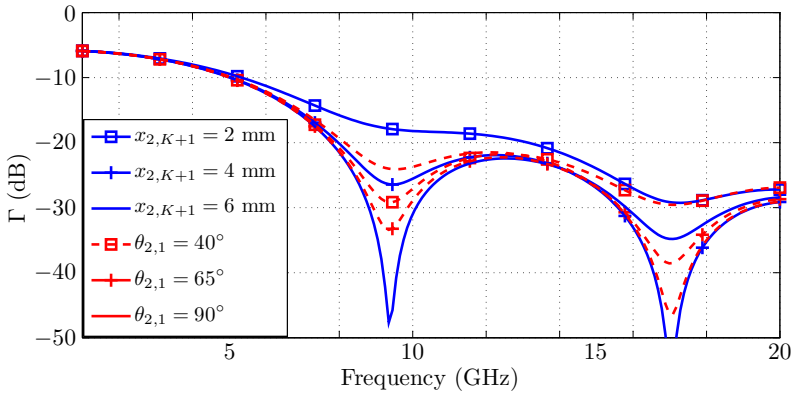


(a)

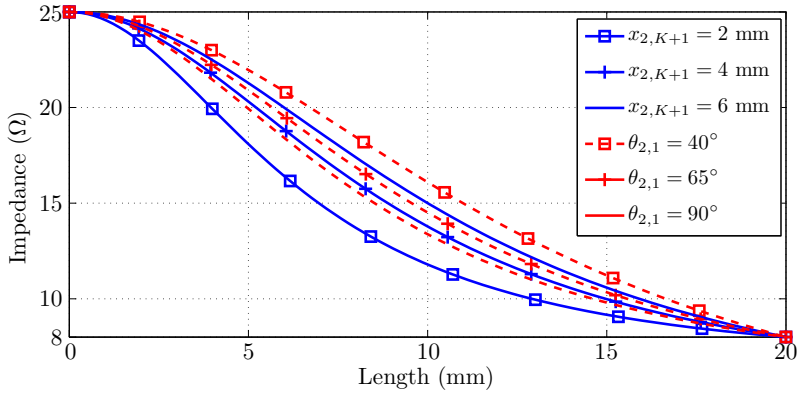


(b)

Figure 2.21: Examples showing how the impedance taper changes when different dimensions are adjusted. In (a) and (b) $l_t = 20$ mm, for the solid lines $\theta_{2,1} = 90°$, and the dashed lines $x_{2,K+1} = 3.5$ mm.

$\theta_{1,1} = \theta_{1B}$ and $\theta_{2,1} = 90°$ in (2.45), and rewriting the half-angle cotangents results in

$$\begin{aligned} r_1 &= r_2 \frac{\sin\theta_{1B}}{1-\cos\theta_{1B}} \times 1 + \frac{\sin\theta_{1B}}{1-\cos\theta_{1B}} R_1 \cot\theta_{1B} \\ &= \frac{R_1\cos\theta_{1B} + r_2\sin\theta_{1B}}{1-\cos\theta_{1B}}, \end{aligned} \tag{2.53}$$

which is exactly (2.6).

It should be stressed again that the transition is designed purely from a geometrical standpoint to provide a simple and smooth conical to coaxial transition between lines of, in general, different characteristic impedances. The resulting impedance profile of the transition is thus fixed by the geometry, and not specifically and explicitly designed. A transition between an 8 Ω conical line and 25 Ω coaxial line is investigated as an example, since these levels are encountered in some previous designs [4].

It is possible to scale the frequency response by scaling all the dimensions of the transi-

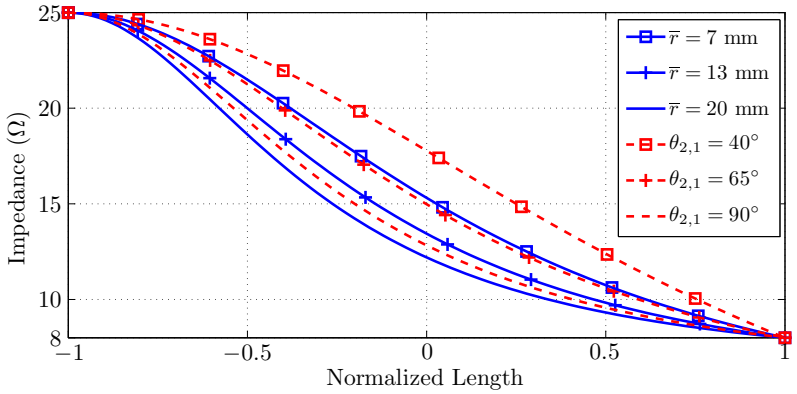


(a)

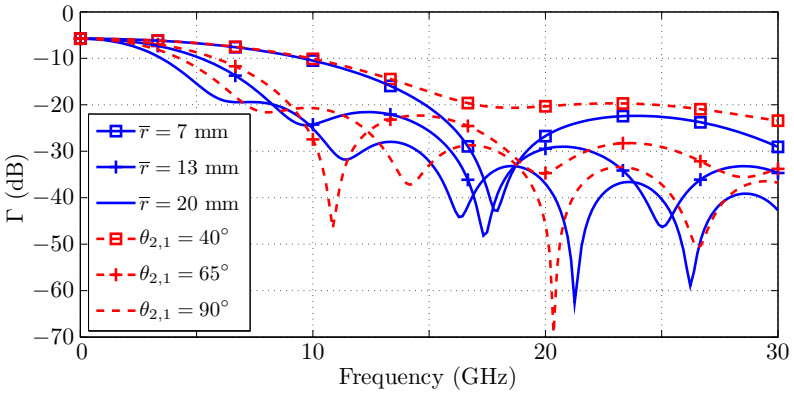


(b)

Figure 2.22: In (a) and (b) $x_{2,K+1} = 3.5$ mm, for the solid lines $\theta_{2,1} = 90°$, and the dashed lines $\overline{r} = 16$ mm.

tion using the same scaling factor. In Fig. 2.21 the transition length $l_t$ is kept constant at 20 mm and $\theta_{2,1}$ and $x_{2,K+1}$ are varied to show the resulting impedance profiles and reflection coefficients. Note that $\theta_{1,1}$ and $x_{1,K+1}$ are fixed by the chosen impedance levels. Fig. 2.22 shows the effect of changing the length, $l_t$, by varying $\theta_{2,1}$ and $\overline{r}$. There are two tapers in Fig. 2.22, $\overline{r} = 7$ mm and $\theta_{2,1} = 65°$, with different lengths and almost identical normalized impedance profiles, resulting in frequency scaled versions of the same reflection coefficient. Interestingly, an increase in $l_t$ does not necessarily result in the same normalized taper with a wider matched bandwidth, whereas it does with other well-known tapers such as the exponential, triangular, near-optimal Hecken [45] and optimal Klopfenstein [39] tapers. This is due to the fact that it is not the impedance profile that is designed, but rather the physical profile, which changes with $l_t$, and thus causes the impedance taper to change as well. Also note that unlike these well-known tapers, the impedance in the middle of the transition taper is not necessarily equal to the geometric mean of the start and end impedance levels.

Some dimensions, such as the outer conductor radius of the central coaxial port, $x_{2,K+1}$,

and the conical angle, $\theta_{2,1}$, may need to be fixed or limited to the dimensions of standard components when using the transition in a conical combiner. The performance of the taper is thus best judged when it is used in a combining structure, and the length and impedance levels are designed with the rest of the combiner network and not in isolation. This is illustrated in the next section by a design example.

#### 2.3.1.3 Design Example

A 10-way conical combiner with a centre frequency of 10 GHz is designed, utilizing the same peripheral feeding port configuration as in [4], except that the partially-filled coaxial lines are 65.4 Ω followed by 85.6 Ω air-filled coaxial lines, and the uncompensated shorted feeding method is used as described in Section 2.2. The conical angle $\theta_{2,1}$ is fixed to 90°, and the inner and outer conductor radii of the central coaxial port are fixed to the

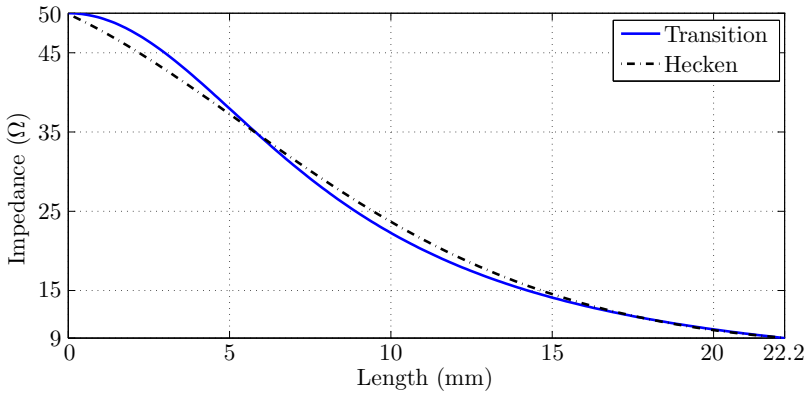


(a)

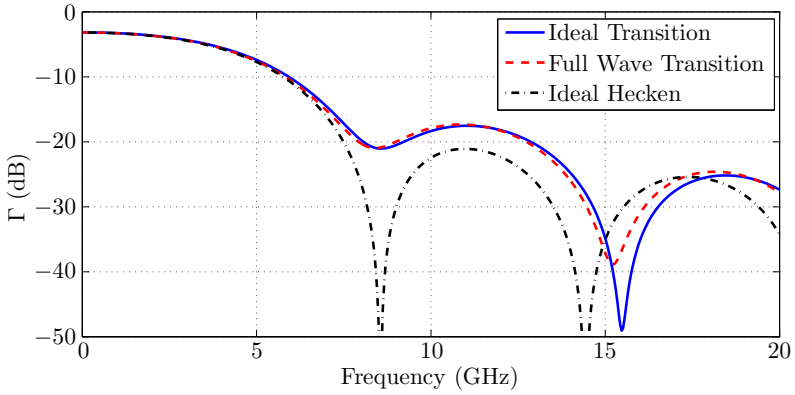


(b)

Figure 2.23: A transition taper compared to a Hecken taper with the same length, 22.2 mm and minimum frequency, 7.5 GHz. The Impedance levels are shown in (a) and the reflection coefficient in (b), where the equivalent circuit model of the transition taper is also compared to full-wave simulation results.

Table 2.4: Dimensions of the optimized transition.

| Parameter | Value | Parameter | Value |
|---|---|---|---|
| $\theta_{1,1}$ | 81.44° | $x_{2,K+1}$ | 3.5 mm |
| $\theta_{2,1}$ | 90° | $r_1$ | 16.06 mm |
| $x_{1,K+1}$ | 1.52 mm | $r_2$ | 13.6 mm |

standard 50 Ω N-type connector dimensions and the peripheral ports to the standard 50 Ω SMA connector dimensions. The lengths of the 65.4 Ω and 85.6 Ω lines together with their placement radius, $r_p$, the conical line impedance, the conical line back short length, $r_b$, and the transmission length of the conical to coaxial transition, $l_t$, are the optimization parameters. These parameters are optimized using a Nelder-Mead [47] based Simplex search to achieve a good central port ($S_{11}$) match to 50 Ω. The resulting parameters of the transition are listed in Table 2.4. The impedance taper and reflection coefficient of the resulting transition are compared to a Hecken taper with the same length and bandwidth in Fig. 2.23. It turns out that the optimal transition in this case has a similar impedance profile to the Hecken taper, which is the optimal smooth impedance taper. Note that this is as a result of optimisation, and this transition will generally not have an impedance taper similar to a Hecken taper. A difference of roughly 4 dB in the maximum reflection coefficient is observed: The transition has a maximum reflection coefficient of −17.5 dB compared to the Hecken taper with −21.5 dB. Fig. 2.23 also shows that the circuit model and full-wave simulation of the transition agree to within 1 dB over the simulated frequency band, except where the reflection coefficient is below −25 dB.

A CAD model of the combiner together with its circuit model, full-wave simulation, and measured results is shown in Fig. 2.24. Fig. 2.24(a) shows that the smallest spacing between the inner and outer conductors is now at the 50 Ω central coaxial port, which is significantly larger and thus easier to manufacture compared to both [3] and [4]. The manufacturability of this design is confirmed by the agreement between the full-wave simulated and measured results to within 2 dB over the operating band, as shown in Fig. 2.24(b). A minimum isolation between the peripheral input ports of 7.5 dB is measured between ports on opposite sides of the combiner. A maximum phase and amplitude imbalance of ±3.2° and ±0.25 dB is measured, respectively, and an insertion loss of better than 0.28 dB is measured in the operating band of the combiner. The measured $S_{11}$ is better than −20 dB with a 24 % bandwidth and better than −23 dB with a 20 % bandwidth around 10 GHz, compared to the measured results of previous designs in [3] and [4], where −14.7 dB with 74 % and −18 dB with 47 % was obtained, respectively. Although the design with the tapered transition does not have the same bandwidth performance compared to the previous designs, the obtained 24 % is sufficient for many applications.

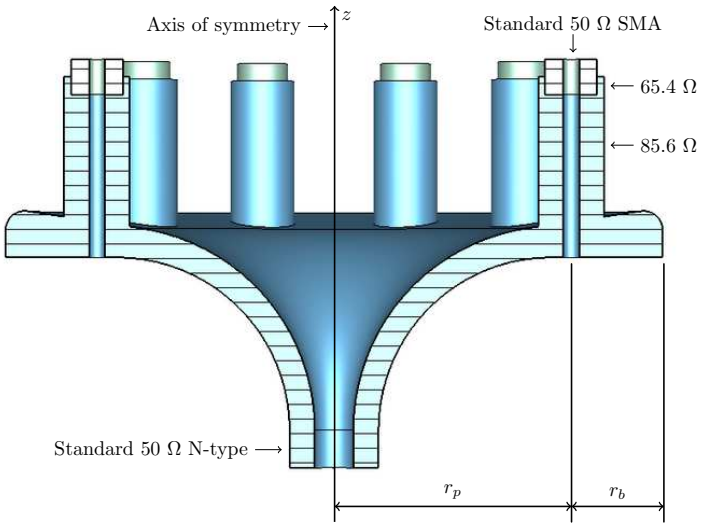


(a)

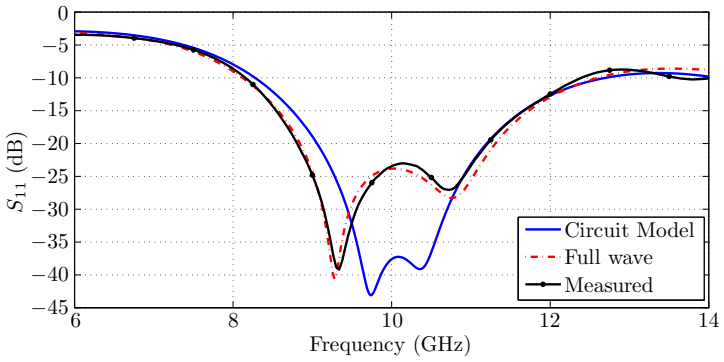


(b)

Figure 2.24: (a) A 3D CAD model of the conical combiner designed using the impedance tapered transition, and (b) its circuit model and full-wave simulation results.

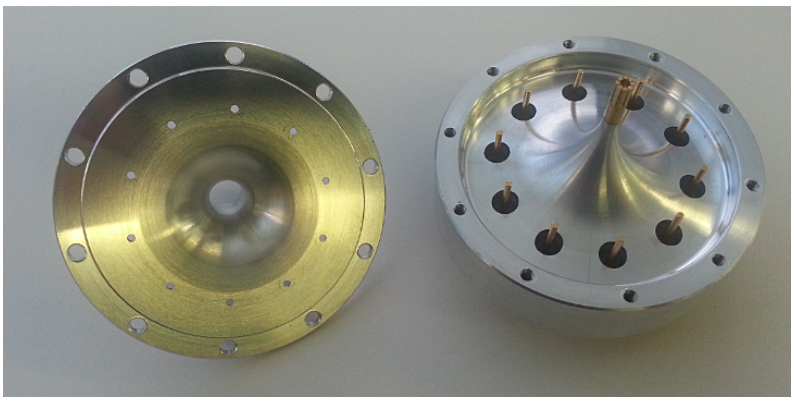

Figure 2.25: A photo of the manufactured top and bottom halves of the conical combiner.

Note that $S_{11}$ around the centre frequency of the combiner is better than the reflection coefficient of the transition over the same frequency range. This is possible due to additional compensation provided by the rest of the network in the combiner, which could be optimized together with the combiner dimensions using the equivalent circuit model and

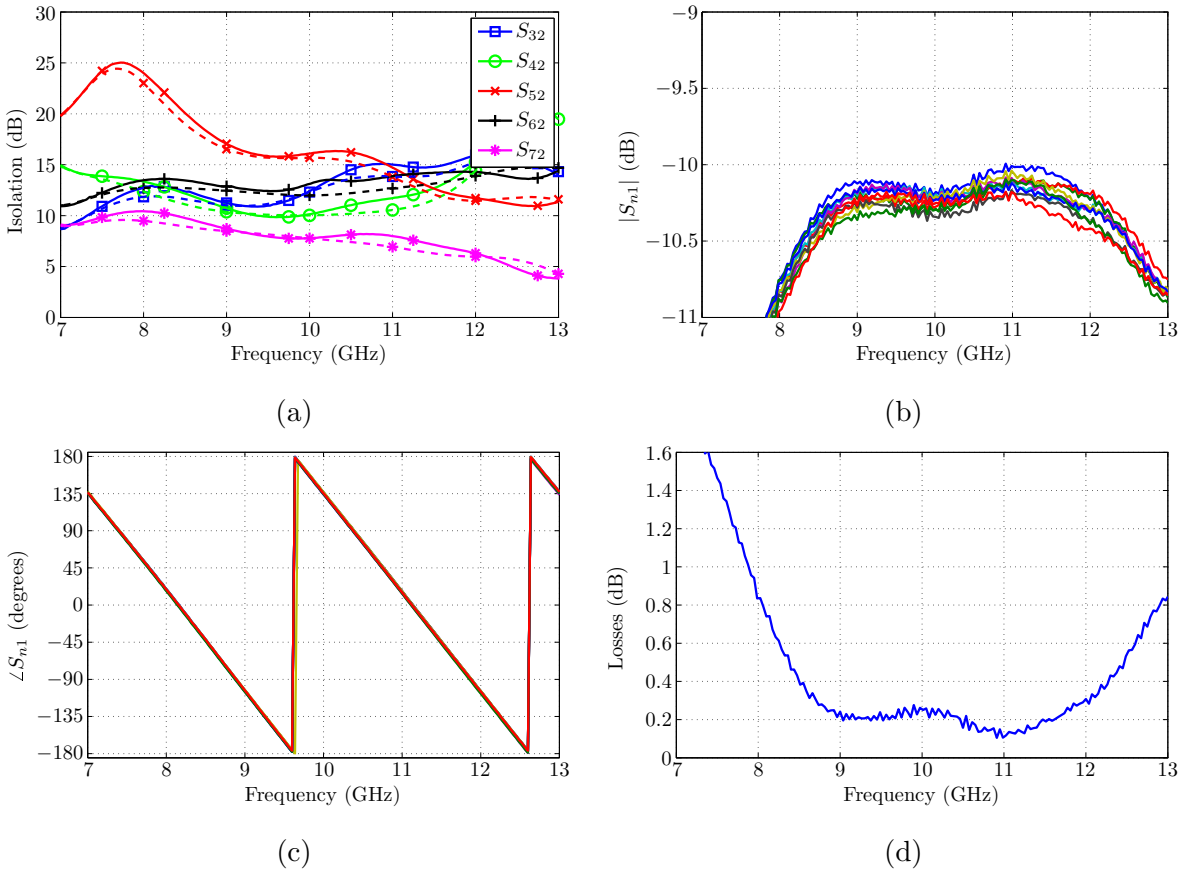


Figure 2.26: The measured isolation (solid lines) and full-wave simulated isolation (dashed lines) is shown in (a), the measured amplitude and phase balance in (b) and (c), and the measured total insertion loss of the combiner in (d).

empirical equations of Section 2.2. Although this design has a narrower bandwidth compared to previous designs, it is significantly simpler to manufacture, and this is reflected in the agreement between the full-wave simulated and measured results.

### 2.3.2 Multi-Section Transition

The design and analysis of an impedance tapered conical to coaxial line transition consisting of a single constant radius section is presented in Section 2.3.1. In Section 2.3.1, the transition is formed by a pair of constant radius arcs with radii $r_1$ and $r_2$ joining the conical line conductors defined by $\theta_1$ and $\theta_2$ to the inner and outer conductors of the coaxial line, respectively. This idea is extended here so that the transition may now consist out of many such sections, each with a pair of constant radius arcs joining the conical line conductors at the end of the previous transition section to those at the beginning of the next transition section. The goal is to add degrees of freedom to the impedance profile of the taper, so that it may be optimized to the specifications of the designer.

#### 2.3.2.1 Analysis and Design Equations

The analysis of the multi-section transition is similar to the method presented in Section 2.3.1, except that the analysis needs to be repeated for each section. As previously explained, the conductor formed by the arc with radius $r_2$ in the single-section transition can be divided into $K$ equal length arcs, subtended by equal angle subsections. Each of these subsections is approximated using a constant impedance conical transmission line, the first of which is equal to the initial conical line before the transition starts, and the last ($K$-th) subsection ending in the coaxial line where the transition ends. The impedance of each conical line section can then be determined by first calculating the angle $\theta_1$ corresponding to its $\theta_2$ angle, and then using the formula for the characteristic impedance of a conical transmission line. Similarly, for a transition consisting of $M$ sections, and thus $M$ constant radius arc pairs, each $m$-th section is divided into $K$ constant impedance conical transmission lines from the starting angle, $\theta_{2,1}^{(m)}$, up to the ending angle, $\theta_{2,K+1}^{(m)}$, of that particular section. Fig. 2.27 shows an example of a multi-section transition with $M = 3$. Similar to (2.30),(2.38) - (2.40) for the single-section transition, the conical line conductor

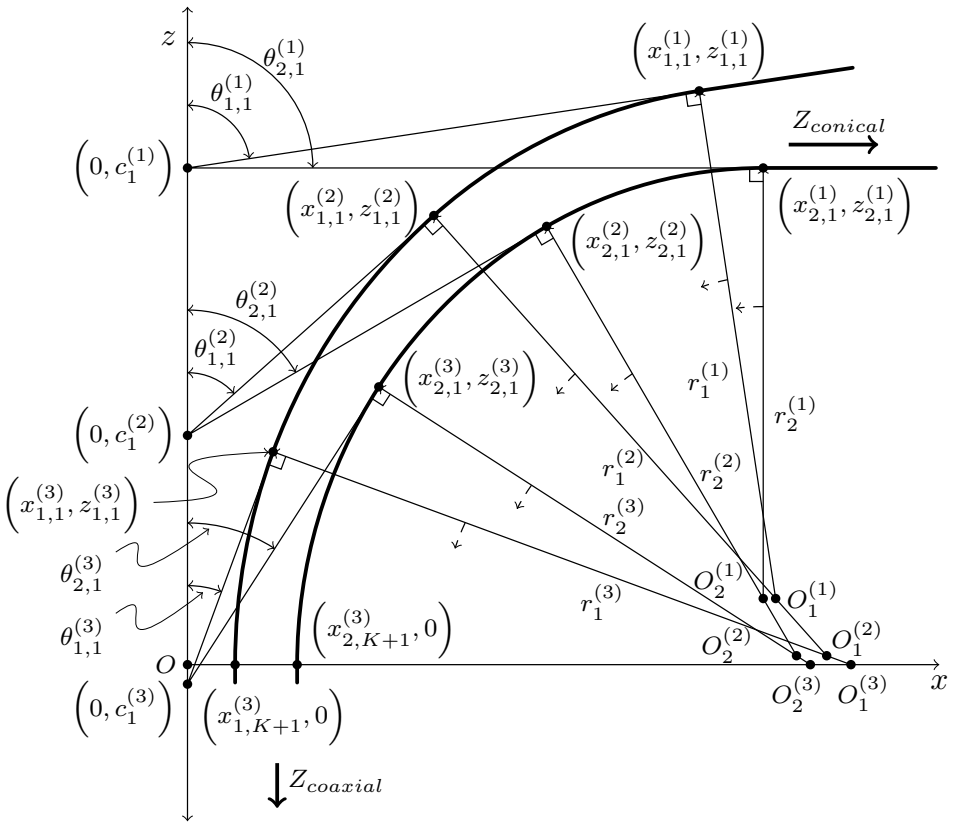


Figure 2.27: A sketch of the profile of a multi-section conical to coaxial transition with $M = 3$. The dashed arrows indicate the direction of validity for the radii of the different constant radius arcs.

angles of the $k$-th subsection of the $m$-th constant radius transition section are

$$\theta_{2,k}^{(m)} = \frac{k}{K+1}\left(\theta_{2,1}^{(m)} - \theta_{2,K+1}^{(m)}\right), \tag{2.54}$$

and

$$\theta_{1,k}^{(m)} = \arcsin\left[\frac{-2r_1^{(m)}\beta_k^{(m)} \pm \sqrt{\Delta_k^{(m)}}}{2(\alpha^{(m)})^2 + 2(\beta_k^{(m)})^2}\right], \tag{2.55}$$

with

$$\Delta_k^{(m)} = 4\left(r_1^{(m)}\beta_k^{(m)}\right)^2 - 4\left[\left(\alpha^{(m)}\right)^2 + \left(\beta_k^{(m)}\right)^2\right]\left[\left(r_1^{(m)}\right)^2 - \left(\alpha^{(m)}\right)^2\right], \tag{2.56}$$

$$\alpha^{(m)} = x_{1,K+1}^{(m)} + r_1^{(m)}\cos\theta_{1,K+1}^{(m)}, \tag{2.57}$$

$$\beta_k^{(m)} = x_{2,k}^{(m)}\cot\theta_{2,k}^{(m)} - r_2^{(m)}\sin\theta_{2,k}^{(m)}, \tag{2.58}$$

and

$$x_{2,k}^{(m)} = x_{2,K+1}^{(m)} + r_2^{(m)}\left(\cos\theta_{2,K+1}^{(m)} - \cos\theta_{2,k}^{(m)}\right). \tag{2.59}$$

Note that for all $m < M$:

$$\theta_{1,1}^{(m+1)} = \theta_{1,K+1}^{(m)}, \tag{2.60}$$

$$\theta_{2,1}^{(m+1)} = \theta_{2,K+1}^{(m)}, \tag{2.61}$$

$$x_{1,1}^{(m+1)} = x_{1,K+1}^{(m)}, \tag{2.62}$$

$$x_{2,1}^{(m+1)} = x_{2,K+1}^{(m)}. \tag{2.63}$$

Once these angles are known, the impedance throughout the transition can be calculated using

$$Z_k^{(m)} = 60\ln\left[\frac{\cot(\theta_{1,k}^{(m)})}{\cot(\theta_{2,k}^{(m)})}\right]. \tag{2.64}$$

The impedance at the end of the last section should rather be calculated using

$$Z_{K+1}^{(M)} = 60\ln\left(\frac{x_{2,K+1}^{(M)}}{x_{1,K+1}^{(M)}}\right), \tag{2.65}$$

since $\theta_{1,K+1}^{(M)} = \theta_{2,K+1}^{(M)} = 0°$, because the transition ends in a coaxial line.

If $M = 1$, as in Section 2.3.1, then $\theta_{2,K+1}^{(1)} = \theta_{1,K+1}^{(1)} = 0°$, $x_{1,K+1}^{(1)}$ and $x_{2,K+1}^{(1)}$ are the inner and outer conductor radii of the coaxial line, and $\theta_{2,1}^{(1)}$ is chosen (usually 90°). The equations needed to design and determine the impedance taper of the transition where $M = 1$ are presented in Section 2.3.1, however, they are not applicable when $M > 1$. The design equations are thus extended so that they are valid for $M > 1$, when some of the constant

radius transition sections do not end in a coaxial line, and thus $\theta_{1,K+1}^{(m)} \neq \theta_{2,K+1}^{(m)} \neq 0°$. A similar derivation as for the single-section transition is followed, and the transition radii $r_1^{(M)}$ and $r_2^{(M)}$ can be designed using the resulting equations:

$$r_1^{(m)} = A^{(m)} B^{(m)} r_2^{(m)} + A^{(m)} \left( C^{(m)} - D^{(m)} \right), \tag{2.66}$$

where

$$A^{(m)} = \frac{\sin\theta_{1,1}^{(m)}}{1 - \cos\theta_{1,K+1}^{(m)} \cos\theta_{1,1}^{(m)}}, \tag{2.67}$$

$$B^{(m)} = \frac{1 - \cos\theta_{2,K+1}^{(m)} \cos\theta_{2,1}^{(m)}}{\sin\theta_{2,1}^{(m)}}, \tag{2.68}$$

$$C^{(m)} = x_{1,K+1}^{(m)} \cot\theta_{1,1}^{(m)}, \tag{2.69}$$

and

$$D^{(m)} = x_{2,K+1}^{(m)} \cot\theta_{2,1}^{(m)}. \tag{2.70}$$

Note that it can be shown that (2.66) can be reduced to (2.6) in the same way as is done in (2.53), if $\cos\theta_{2,K+1}^{(m)} = \cos\theta_{1,K+1}^{(m)} = 0°$. However, (2.66) - (2.70) can still only be used to calculate $r_1^{(m)}$ and $r_2^{(m)}$ for a transition section ending in a coaxial line: When a transition section ends in a coaxial line, $x_{1,K+1}^{(m)}$ and $x_{2,K+1}^{(m)}$ can be chosen independently from their position along the $z$-axis, whereas if the transition section ends in a conical line ($\theta_{1,K+1}^{(m)} \neq \theta_{2,K+1}^{(m)} \neq 0°$), $x_{1,K+1}^{(m)}$ and $x_{2,K+1}^{(m)}$ are dependent on their $z$-positions $z_{1,K+1}^{(m)}$ and $z_{2,K+1}^{(m)}$. Equations (2.66) - (2.70) are thus not sufficient to design a conical to conical transition, since $x_{1,K+1}^{(m)}$ and $x_{2,K+1}^{(m)}$ cannot be determined, and they are needed to calculate $r_1^{(m)}$ and $r_2^{(m)}$. This problem can be solved by adding the condition that

$$r_1^{(m)} \sin\theta_{1,K+1}^{(m)} - r_2^{(m)} \sin\theta_{2,K+1}^{(m)} = r_1^{(m+1)} \sin\theta_{1,K+1}^{(m)} - r_2^{(m+1)} \sin\theta_{2,K+1}^{(m)}, \tag{2.71}$$

which, when satisfied together with (2.66), results in

$$z_{1,K+1}^{(m)} = z_{1,1}^{(m+1)}, \tag{2.72}$$

$$z_{2,K+1}^{(m)} = z_{2,1}^{(m+1)}, \tag{2.73}$$

$$x_{1,K+1}^{(m)} = x_{1,1}^{(m+1)}, \tag{2.74}$$

and

$$x_{2,K+1}^{(m)} = x_{2,1}^{(m+1)}. \tag{2.75}$$

Equation (2.71) can be written in the following form for convenience:

$$r_1^{(m)} = A'^{(m)} B'^{(m)} r_2^{(m)} + A'^{(m)} \left( C'^{(m)} - D'^{(m)} \right), \tag{2.76}$$

where

$$A'^{(m)} = \text{cosec}\theta_{1,K+1}^{(m)}, \tag{2.77}$$
$$B'^{(m)} = \sin\theta_{2,K+1}^{(m)}, \tag{2.78}$$
$$C'^{(m)} = r_1^{(m+1)} \sin\theta_{1,K+1}^{(m)}, \tag{2.79}$$

and

$$D'^{(m)} = r_2^{(m+1)} \sin\theta_{2,K+1}^{(m)}. \tag{2.80}$$

Using (2.66) and (2.76) to solve simultaneously for $r_1^{(m)}$ and $r_2^{(m)}$ leads to

$$r_1^{(m)} = \frac{X^{(m)} - X'^{(m)}}{Y'^{(m)} - Y^{(m)}}, \tag{2.81}$$

and

$$r_2^{(m)} = \frac{Y'^{(m)} X^{(m)} - Y^{(m)} X'^{(m)}}{Y'^{(m)} - Y^{(m)}}, \tag{2.82}$$

where

$$X^{(m)} = A^{(m)} \left( C^{(m)} - D^{(m)} \right), \tag{2.83}$$
$$X'^{(m)} = A'^{(m)} \left( C'^{(m)} - D'^{(m)} \right), \tag{2.84}$$
$$Y^{(m)} = A^{(m)} B^{(m)}, \tag{2.85}$$

and

$$Y'^{(m)} = A'^{(m)} B'^{(m)}. \tag{2.86}$$

Equations (2.81) and (2.82) can now be used to calculate $r_1^{(m)}$ and $r_2^{(m)}$, given that the dimensions of the $(m+1)$-th section are known.

The problem can now be solved by starting from the last transition section ($m = M$), which ends in a coaxial line, by using (2.66) and then using (2.62) and (2.63) to determine the parameters for the preceding conical to conical transition section. Each $m$-th conical to conical transition section can then be designed by using (2.81) and (2.82) with the parameters of the $(m+1)$-th section and continuing this process to get to the first transition section where $m = 1$. This process will be discussed in more detail in the next section.

#### 2.3.2.2 Design Procedure

It is assumed that the conical and coaxial line impedances on either side of the transition are chosen, as well as any desired impedance levels throughout the transition and the transmission lengths of each constant radius transition section between them. For an $M$-section transition, $M-1$ impedance levels and $M$ lengths can be chosen besides the start and end impedances. This information will be used to design the radii of each of the constant radius transition sections. The design procedure involves calculating the radii for all the transition sections using some initial values, and repeating this calculation to find the correct values for each $\theta_{2,1}^{(m)}$, $r_1^{(m)}$, and $r_2^{(m)}$ which result in the desired transmission length for each section. The correct values can be found by minimizing an error function [such as (2.96)] using a suitable optimization algorithm with the $\theta_{2,1}^{(m)}$ angles as optimizable parameters.

The initial value for each $\theta_{2,1}^{(m)}$ can be found by dividing the angle of the entire transition into $M$ equal-angle sections:

$$\theta_{2,1}^{(m)} = \left(1 - \frac{m-1}{M}\right)\theta_{2,1}^{(1)}. \tag{2.87}$$

The next step is to calculate the corresponding $\theta_{1,1}^{(m)}$ angles of the conical line conductors at each of the points between the constant radius transition sections where the impedance levels have been chosen, using

$$\theta_{1,1}^{(m)} = 2\arctan\left[\frac{\tan(\theta_{2,1}^{(m)}/2)}{\mathrm{e}^{Z_1^{(m)}/60}}\right], \tag{2.88}$$

where $Z_1^{(m)}$ is the chosen impedance at the start of the $m$-th transition section. As explained in section 2.3.2.1, the dimensions of each transition section need to be determined starting from the last section, which ends in a coaxial line. The inner and outer conductor radii of the coaxial line, $x_{1,K+1}^{(M)}$ and $x_{2,K+1}^{(M)}$, need to be known in order to start the design procedure. Using $x_{1,K+1}^{(M)}$, $x_{2,K+1}^{(M)}$, and the values obtained from (2.87) and (2.88), the radius $r_2^{(M)}$ can be calculated by rearranging (2.66) so that

$$r_2^{(M)} = \frac{2\overline{r}^{(M)} - A^{(M)}\left(C^{(M)} - D^{(M)}\right)}{1 + A^{(M)}B^{(M)}}, \tag{2.89}$$

where

$$\overline{r}^{(m)} = \frac{l^{(m)}}{\overline{\theta}^{(m)}}, \tag{2.90}$$

with $l^{(m)}$ the chosen length of the $m$-th transition section, and

$$\overline{\theta}^{(m)} = \frac{\theta_{1,1}^{(m)} + \theta_{2,1}^{(m)}}{2} - \frac{\theta_{1,K+1}^{(m)} + \theta_{2,K+1}^{(m)}}{2}. \tag{2.91}$$

Note that for $m < M$,

$$\theta_{1,K+1}^{(m)} = \theta_{1,1}^{(m+1)}, \tag{2.92}$$

and

$$\theta_{2,K+1}^{(m)} = \theta_{2,1}^{(m+1)}, \tag{2.93}$$

and for $m = M$,

$$\theta_{1,K+1}^{(M)} = \theta_{2,K+1}^{(M)} = 0°. \tag{2.94}$$

The radius $r_1^{(M)}$ can then be calculated using

$$r_1^{(m)} = 2\overline{r}^{(m)} - r_2^{(m)}, \tag{2.95}$$

since $\overline{r}^{(m)}$ is the average of $r_1^{(m)}$ and $r_2^{(m)}$. Once $r_1^{(M)}$ and $r_2^{(M)}$ are known, we can calculate $r_1^{(M-1)}$ and $r_2^{(M-1)}$, followed by $r_1^{(M-2)}$ and $r_2^{(M-2)}$, etc. using (2.81) and (2.82) until the radii of all sections have been calculated. The design procedure this far yields angles ($\theta_{1,1}^{(m)}$ and $\theta_{2,1}^{(m)}$) and radii ($r_1^{(m)}$ and $r_2^{(m)}$) for all the transition sections that may result in transmission lengths for the transition sections that are not equal to the chosen lengths, except for the $M$-th section. This is due to the fact that the set of equations we are solving are underdetermined, and there are thus many possible combinations of parameters that may result in a smooth transition, but not necessarily with the impedance profile or transmission length that we desire. The correct angles and radii for the rest of the sections can be found by minimizing an error function such as

$$\epsilon = \sum_{m=M}^{1} \left( l^{(m)} - \overline{r}^{\,(m)} \overline{\theta}^{\,(m)} \right)^2 \tag{2.96}$$

with the angles $\theta_{2,1}^{(m)}$ as optimizable parameters, using an optimization algorithm such as a Nelder-Meade based Simplex search [47].

#### 2.3.2.3 Taper Characteristics

Unlike the single-section transition in Section 2.3.1, which could not have an explicitly designed impedance taper, the designer can now choose or optimize impedance levels throughout the transition. Three different impedance tapered transitions with total lengths of 25 mm are designed from 9 Ω conical lines with $\theta_{2,1}^{(1)} = 90°$ to 50 Ω coax-

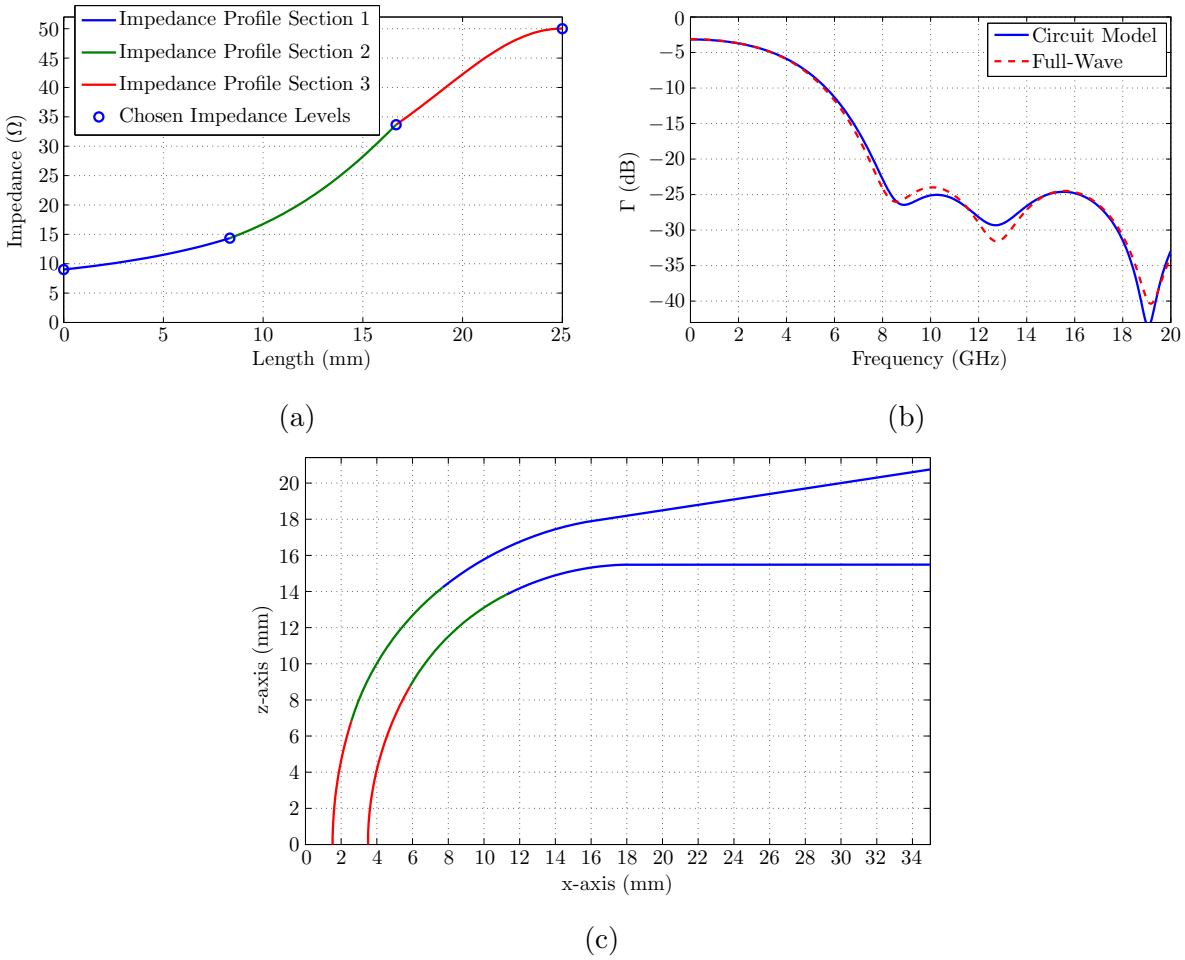


Figure 2.28: (a) The impedance profile of the first example, (b) its circuit model and full-wave simulated reflection coefficients, and (c) the physical profile of the transition. Note that (c) is rotationally symmetric around the $z$-axis.

ial lines with standard N-type inner and outer conductor radii of $x_{1,K+1}^{(M)} = 1.52$ mm and $x_{2,K+1}^{(M)} = 3.5$ mm, to illustrate some of the characteristics of the multi-section transition.

The first transition consists of three sections ($M = 3$), so that there are two impedance levels and three lengths that can be chosen or optimized. In this example, the values are obtained by optimization as part of the design of the conical combiner discussed in Section 2.3.2.4. The following values are obtained: $Z_{K+1}^{(3)} = 50\ \Omega$, $Z_1^{(3)} = 33.65\ \Omega$, $Z_1^{(2)} = 14.5\ \Omega$, $Z_1^{(1)} = 9\ \Omega$, $l^{(3)} = l^{(2)} = l^{(1)} = 8.33$ mm. The resulting impedance profile, physical profile, and reflection coefficient are shown in Fig. 2.28. The reflection coefficient of the transition is calculated using a circuit model and is in agreement to within 2 dB with its full-wave simulation result, as shown in Fig. 2.28(b).

The second transition also consists of three sections, with the same lengths for each of the sections as the first example and with the two variable impedance levels chosen to be almost equal. The chosen values are thus: $Z_{K+1}^{(3)} = 50\ \Omega$, $Z_1^{(3)} = 25\ \Omega$, $Z_1^{(2)} = 24.9\ \Omega$,

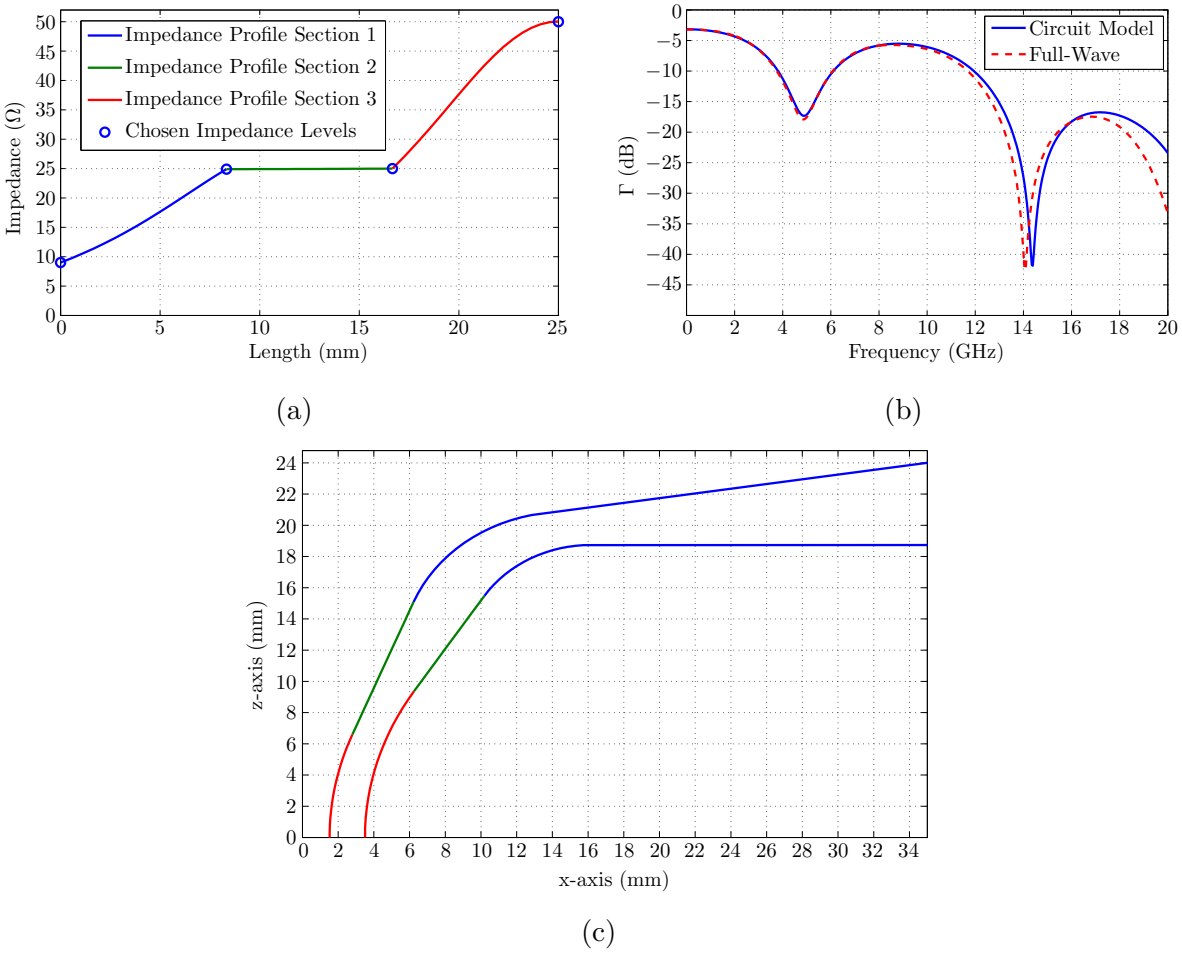


Figure 2.29: (a) The impedance profile of the second example, (b) its circuit model and full-wave simulated reflection coefficients, and (c) the physical profile of the transition. Note that (c) is rotationally symmetric around the $z$-axis.

$Z_1^{(1)} = 9\ \Omega$, $l^{(3)} = l^{(2)} = l^{(1)} = 8.33$ mm. The resulting impedance profile, physical profile, and reflection coefficient are shown in Fig. 2.29. The reflection coefficient of the transition is calculated using a circuit model and a full-wave simulation, and the results are in agreement to within 2 dB over most of the simulated band, but with larger differences where the reflection coefficient is below $-15$ dB, as shown in Fig. 2.29(b). This example illustrates the effect of a transition section with an almost constant impedance. The result is a section with very large radii $r_1^{(m)}$ and $r_2^{(m)}$. It is interesting to note here that this is due to the fact that if the impedance of the $m$-th section is chosen to be constant, it turns out that, for $\theta_{2,K+1}^{(m)} \neq 0°$ and $\theta_{1,K+1}^{(m)} \neq 0°$,

$$Y^{(m)} = Y'^{(m)}, \tag{2.97}$$

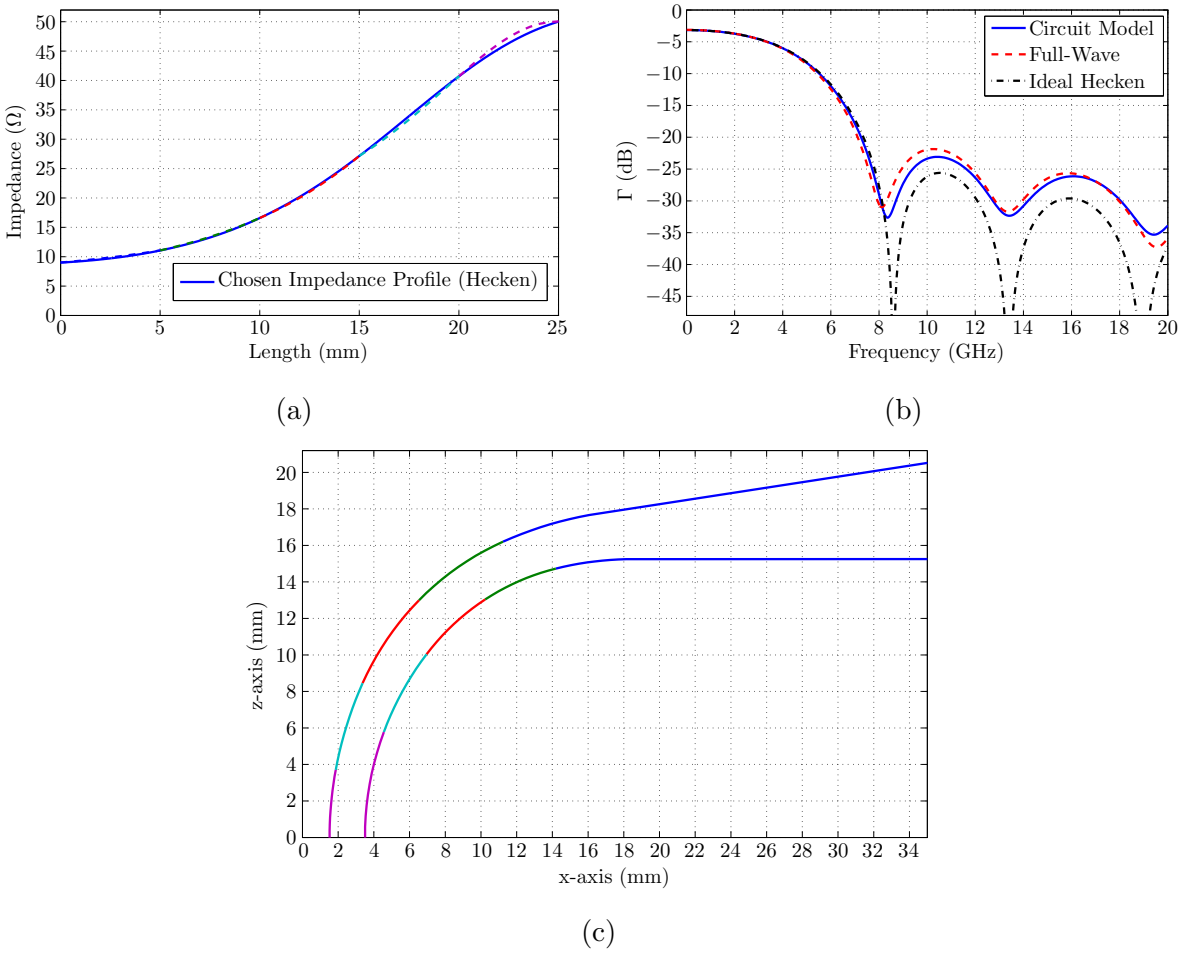


Figure 2.30: (a) The impedance profile of the third example, (b) its circuit model and full-wave simulated reflection coefficients, and (c) the physical profile of the transition. Note that (c) is rotationally symmetric around the $z$-axis.

and thus

$$\frac{\sin\theta_{1,1}^{(m)}\left(1-\cos\theta_{2,1}^{(m)}\cos\theta_{2,K+1}^{(m)}\right)}{\sin\theta_{2,1}^{(m)}\left(1-\cos\theta_{1,1}^{(m)}\cos\theta_{1,K+1}^{(m)}\right)}=\frac{\sin\theta_{2,K+1}^{(m)}}{\sin\theta_{1,K+1}^{(m)}}, \tag{2.98}$$

which causes singularities in both (2.81) and (2.82). This means that the proposed multi-section design method cannot be used for a transition containing any constant impedance sections.

The third example consists of five sections with impedance levels and lengths chosen to approximate a Hecken [45] impedance taper. The chosen impedances and lengths are: $Z_{K+1}^{(5)}=50\ \Omega$, $Z_1^{(5)}=40.75\ \Omega$, $Z_1^{(4)}=27.18\ \Omega$, $Z_1^{(3)}=16.6\ \Omega$, $Z_1^{(2)}=11.06\ \Omega$, $Z_1^{(1)}=9\ \Omega$, $l^{(5)}=l^{(4)}=l^{(3)}=l^{(2)}=l^{(1)}=5$ mm. The approximation is naive in the sense that no attempt was made to minimize the error between the obtained impedance profile of the transition and the desired impedance profile of an actual Hecken taper. The resulting impedance profile, physical profile, and reflection coefficient are shown in Fig. 2.30. The

reflection coefficient of the transition is calculated using a circuit model and a full-wave simulation, and the results agree to within 2 dB, as shown in Fig. 2.30(b). Better agreement between the transition and the ideal Hecken taper can be obtained by increasing the number of sections of the transition. This example shows that a known impedance taper can be approximated using the presented multi-section transition.

#### 2.3.2.4 Design Example

A 10-way conical combiner with a center frequency of 10 GHz is designed with exactly the same configuration as in Section 2.3.1, except that a multi-section conical to coaxial transition is used. Partially-filled coaxial lines of 65.4 Ω are used at the input ports, followed by 85.6 Ω air-filled coaxial lines that transition into the conical transmission line.

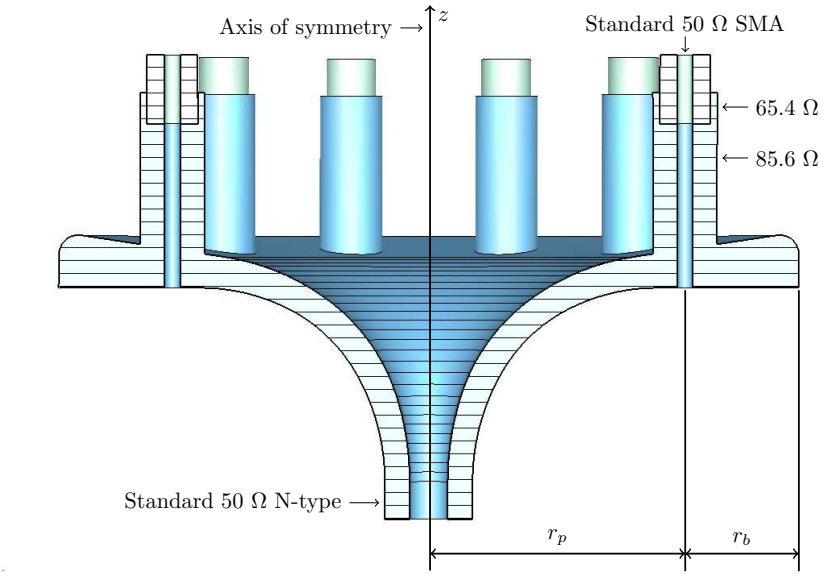


(a)

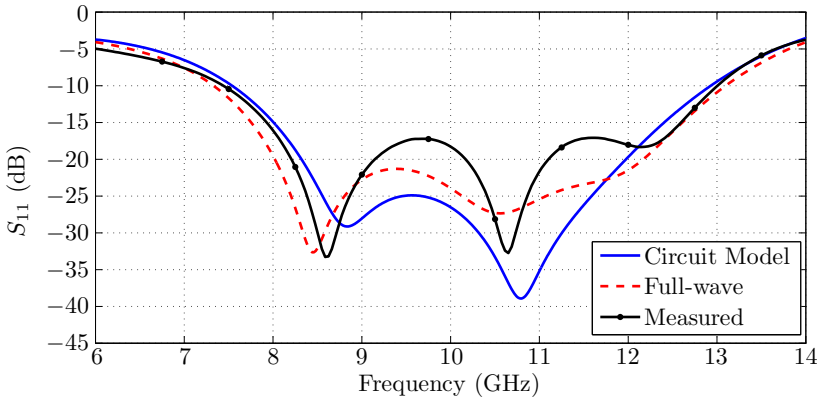


(b)

Figure 2.31: (a) A 3D CAD model of the conical combiner designed using the multi-section transition, and (b) its circuit model, full-wave simulation and measured results.

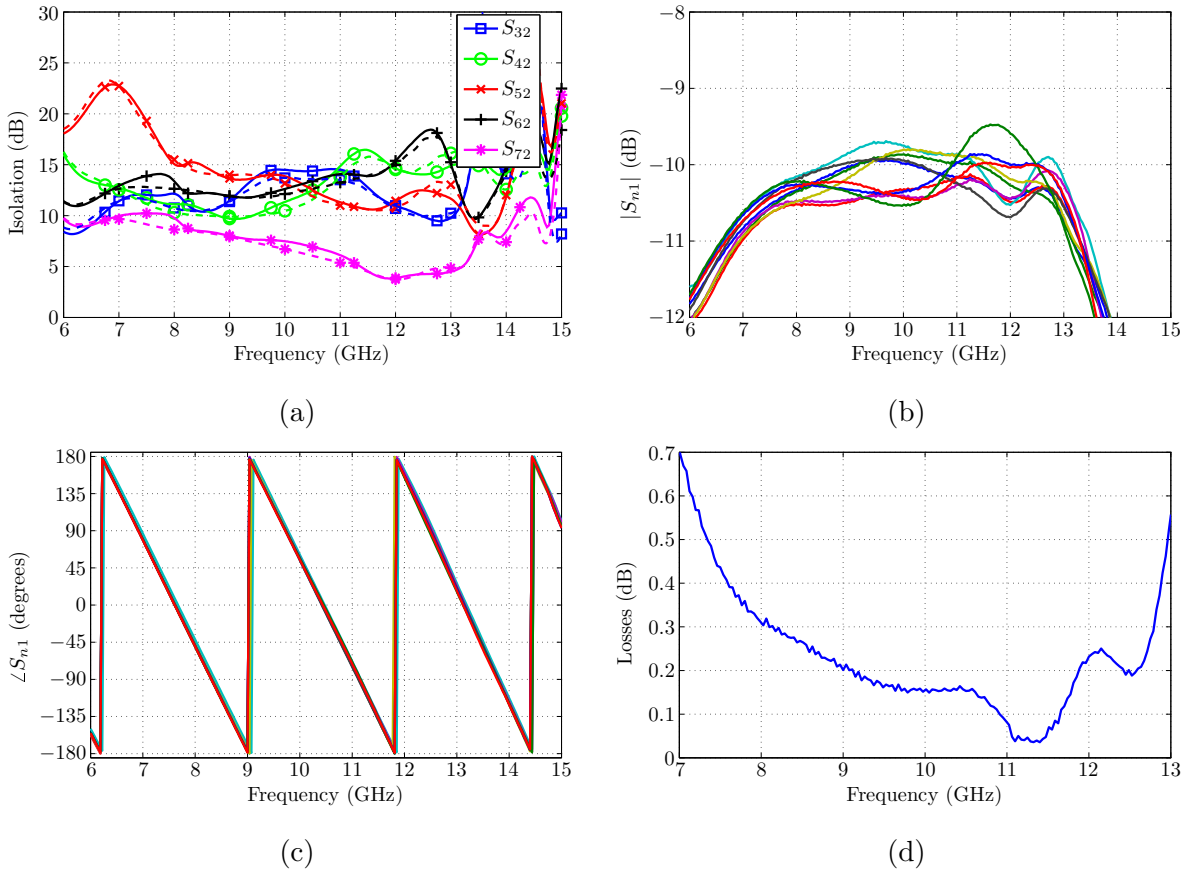


Figure 2.32: The measured isolation (solid lines) and full-wave simulated isolation (dashed lines) is shown in (a), the measured amplitude and phase balance in (b) and (c), and the measured total insertion loss of the combiner in (d).

The conical angle $\theta_{2,1}^{(1)}$ is fixed to 90°, the inner and outer conductor radii of the central output coaxial line are fixed to the standard 50 Ω N-type connector dimensions (1.52 mm and 3.5 mm), and the peripheral input ports are standard 50 Ω SMA connectors. The lengths of the 65.4 Ω and 85.6 Ω coaxial lines, their placement radius $r_p$, the conical line impedance $Z_1^{(1)}$, the length of the conical line back-short $r_b$, and two impedance levels in the transition $Z_1^{(2)}$ and $Z_1^{(3)}$ are optimized. The peripheral placement radius $r_p$ and back-short length $r_b$ are shown in Fig. 2.31(a). The obtained transition is shown as the first example in Section 2.3.2.3. An equivalent circuit model of the combiner is built in a circuit simulator using the information presented in Section 2.2, and the parameters optimized using a Nelder-Mead based Simplex search [47] to achieve the desired central port reflection coefficient ($S_{11}$). Fig. 2.31(a) shows a model of the resulting combiner.

A CNC lathe is used to machine the aluminium parts of the combiner shown in Fig. 2.33. Fig. 2.31(b) shows that the simulated and measured output port reflection coefficients ($S_{11}$) agree to within 3 dB, except where the reflection coefficients are below −17 dB. The measured input port isolation of the combiner is shown in Fig. 2.32(a). The minimum

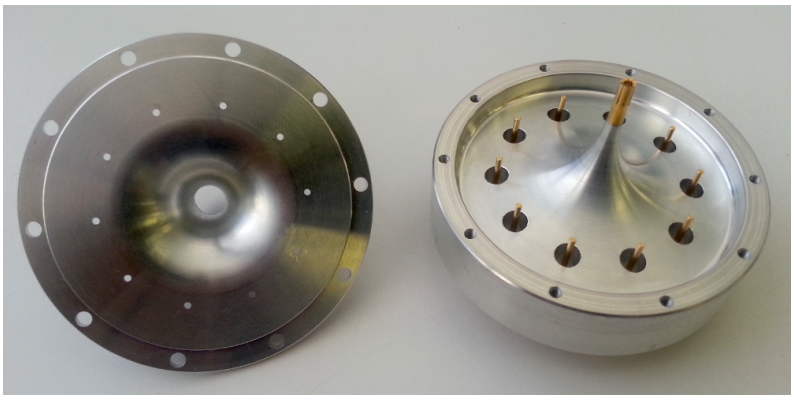

Figure 2.33: A photo of the manufactured top and bottom halves of the conical combiner.

measured input port isolation is 3.7 dB between ports on opposite sides of the combiner. The maximum measured amplitude and phase imbalance of the combiner is ±1 dB and ±8°, and the maximum insertion loss is 0.31 dB in the operating band of the combiner, as shown in Fig. 2.32. The measured $S_{11}$ is better than −17 dB over a 43% bandwidth around 10 GHz, compared to the design with the single-section transition in Section 2.3.1, where an $S_{11}$ of better than −23 dB over a bandwidth of 20% is obtained. The additional degrees of freedom that could be optimized in the multi-section transition have thus effectively allowed a wider matched bandwidth to be achieved in the output port reflection coefficient.

### 2.3.3 Conclusion

A method is presented for the design and analysis of an impedance tapered conical to coaxial transmission line transition that can be used to simplify the design and improve the manufacturability of conical combiners. The characteristics of both the simple single-section and more complex multi-section impedance tapered transitions are illustrated with some examples. The effectiveness of the transition is demonstrated by designing and manufacturing two conical combiners, one with a single-section and one with a multi-section transition. The work on the single-section transition (Section 2.3.1) has been peer-reviewed and accepted for oral presentation at an international conference, and is published in [14]. The work on the multi-section transition is presented in [15].

## 2.4 Conclusion

An equivalent circuit model for conical combiners with shorted coaxial peripheral input ports has been presented in this chapter with empirical equations that allow the circuit model elements to be calculated directly from the dimensions of the combiners and vice

Table 2.5: Comparison of Conical Combiners

| Ref. | $S_{11}$ (dB) | Bandwidth (%) | Loss (dB) | Diameter (mm) |
|---|---|---|---|---|
| Section 2.3.2 | −17 | 43 | 0.31 | 59.2 |
| Section 2.3.1 | −23 | 20 | 0.28 | 51.8 |
| Section 2.2 | −18 | 46 | 0.28 | 49.8 |
| [4] | −18.5 | 47 | 0.28 | 80.0 |
| [3] | −14.7 | 74 | 1.1 | 65.4 |

versa. This allows for rapid optimization of various dimensions of the combiner at a significantly reduced computational cost compared to full-wave simulations. A design procedure has been presented and used to design a conical combiner that is much smaller compared to previous designs while having similar performance. This chapter also presented an impedance tapered conical to coaxial transition that can be used to simplify the design of conical combiners and reduce the required manufacturing effort. Two conical combiners have been designed using the impedance tapered transition and manufactured, where good agreement was obtained between the simulated and measured results.

The comparison of conical combiners in Table 2.5 summarises the benefit in terms of size that the circuit based design method can offer. The design in [3] has the widest bandwidth performance, but has a much higher insertion loss than the other designs, and is difficult to manufacture due to the small spacing between in the inner and outer conductors of the coaxial output line. The problem of the small spacing was addressed in [4] by adding an impedance taper to the conical transmission line to increase the impedance and thus also the spacing at the central output transmission line. This design has better output port return loss than in [3], but is significantly larger. The design in Section 2.2 was designed using the presented circuit based method which lead to a significantly smaller combiner compared to both [3] and [4], with similar performance to [4]. The design in Section 2.3.1 utilized the single-section version of the new impedance tapered transition in order so simplify the design and improve the manufacturability. This design has the best output port return loss, the simplest design and consequently also the best agreement between the simulated and measured results, but at the cost of reduced bandwidth performance. The last design of this chapter, in Section 2.3.2, shows that the bandwidth performance could be recovered by adding some degrees of freedom to the impedance tapered transition design. This design has similar performance to the combiners in [4] and Section 2.2, while being significantly smaller than the design in [4], and replacing the tapered conical line and stepped impedance matching sections in the output coaxial transmission line used in Section 2.2 with a smooth impedance tapered transition.

In summary, the contributions of this chapter are:

1. The development of an equivalent circuit model of shorted peripheral coaxial feeding lines for conical transmission line power combiners [12].
2. The extraction of empirical equations that allow the equivalent circuit model element values to be calculated directly from the physical dimensions of the combiner and vice versa [13].
3. Techniques for the design of a single-section [14] and multi-section [15] impedance tapered conical to coaxial line transition.

# Chapter 3

# Input Port Isolation of Power Combiners

## 3.1 Background on Isolation Techniques

The isolation between input ports of power combiners in SSPAs is an important quality that is needed in order to achieve graceful degradation and prevent spurious oscillations. Isolation is also an important characteristic of combiners and dividers used in antenna array feeds, where a lack thereof may lead to fluctuations in the radiation pattern and input impedance as the scan angle is changed in phased arrays. The ability of a power combiner to act as both a combiner and a divider, and thus to be reciprocal, may not always be necessary in SSPAs, but is especially useful in antenna array feeds in transmit and receive applications. In both these applications high power handling capabilities may be required.

The input port isolation of corporate and chain combiners is dependent on the type of their underlying 2-way combiners: If they have isolated input ports, a corporate or chain network of them will also have isolated input ports. Achieving input port isolation in these types of combiners is therefore usually simple. However, in addition to high insertion losses when $N$ is large, the physical layout of corporate combiners may result in inconvenient isolation load placement. This is less of an issue in 2-way combiners where terminations can be used, however, it may significantly affect the power handling capability when combiners such as Wilkinson combiners are used, where floating isolation loads instead of terminations are needed. Floating isolation loads for microwave frequencies have the drawback of typically being much smaller than terminations, resulting poor power handling capabilities. Floating isolation loads are also typically difficult to move around in a network without affecting the behaviour of the network.

Axially symmetric combiners offer the advantages of significantly lower losses for large $N$, as well as improved amplitude and phase balance. Although axially symmetric combiners with input port isolation such as the $N$-way Wilkinson [5] have been developed, they usually have limited power handling capabilities due to small internal isolation resistors [6] or small spacings and sharp edges at central output ports such as in [7, 8], or are difficult to design due to a lack of information available in literature as well as being difficult to manufacture [9].

The Gysel combiner [6] addresses the issue of small internal isolation resistors in Wilkinson combiners, but there is no closed-form solution for the optimum design parameters, and similar to the Wilkinson combiner, it cannot be realised on a single layer planar structure for $N > 2$. Wilkinson and Gysel power combiners also have the drawback of requiring a node that joins $N$ transmission lines, which becomes increasingly difficult to realise at higher operating frequencies without allowing any higher order modes to propagate. The hybrid $N$-way combiner in [50] may also be difficult to construct due to the many connections needed at each of the input ports, as well as requiring $N(N-1)/2$ isolation loads.

An $N$-way hybrid combiner for reflection type amplifiers, such as diodes, is presented in [10], however, good isolation is not always achievable between all amplifier devices and the power handling may be limited by small isolation resistors. It is shown in [51] how similar hybrid combiners may be used with transmission type devices, but no information is given on the isolation between the input ports. Other $N$-way combiners utilizing radial, coaxial, and conical transmission lines with support for a large number of devices and high power handling capability have been developed. However, these combiners are mostly reactive (lossless) combiners which are reputed to have poor input port isolation, because they do not absorb unsymmetrical modes between input ports. For reactive power combiners, the only achievable isolation between the input ports is due to impedance mismatches.

A well-known method for improving the input port isolation of power combiners is to use ferrite isolators [52] or passive isolation devices [53] at each of the input ports. Besides adding to the size and cost of the system, isolators will make the combiner non-reciprocal which is unacceptable for combiners in, for example, the feeding networks of transmit and receive antenna arrays. Other methods for isolating input ports are presented in [11], but besides having a potentially detrimental impact on reliability in SSPAs, they are only applicable to amplifier networks where special amplifiers with repeatable output impedances are used, or with means to actively detect failures and modify the network by applying an open circuit, short circuit, or through connection in the appropriate locations.

For this chapter, a power combiner that is reciprocal and lossless with matched and isolated input ports will be referred to as an ideal combiner. It has been shown that such an ideal $N$-way combiner cannot be realised with a total of $N+1$ ports [54]: At least $N$ individual isolation loads are needed to realise a lossy passive network with $N$ matched and isolated ports. The $N$ individual isolation loads can be externalised by replacing them with $N$ additional ports, meaning that a lossless passive device with $N$ matched and isolated ports needs to have at least $2N$ ports.

It will be shown in this chapter how to realise an ideal combiner with $2N+2$ ports using a combination of power combiners and 3 dB 90° hybrid couplers. This method has the distinct advantages of being able to produce reciprocal power combiners where terminations can be used for the isolation loads. Additionally, unlike Wilkinson and Gysel combiners, there is no need with this method for a central node to which all input ports are connected, besides through the combiners themselves. This is a significant advantage, especially for large $N$ and at higher frequencies, where it becomes increasingly difficult to realise such a node, since higher order modes will tend propagate in the operating band. A design procedure for such a combiner will be given, as well as some simulated and measured design examples.

## 3.2 Isolation Technique Description

The basic principle of the isolation method is the excitation of two identical modes in two identical combiners with a 90° phase difference between them. Further 90° phase shifts are then added so that the signals are added on the output side and cancelled on the input side. Although 3 dB 90° hybrid couplers are used for the implementation of the isolation method throughout this chapter, the concept is more easily illustrated by using Wilkinson combiners and dividers with 90° delay lines. Fig. 3.1(a) shows a network that consists of two $N$-way power combiners and $N+1$ 3 dB 90° hybrid couplers, and will be referred to as a compound power combiner. Port 1 of the compound power combiner is its output port, ports 2 to $N+1$ are its input ports, and ports $N+2$ to $2N+2$ are where the isolation loads should be connected. Fig. 3.1(b) shows another implementation of the isolation method using two $N$-way power combiners, $N+1$ Wilkinson combiners, and $N+1$ 90° delay lines, where ports $N+2$ to $2N+2$ have been replaced by the isolation loads of the Wilkinson combiners. This implementation will be used for the description that follows.

The combiners $C_1$ and $C_2$ in Fig. 3.1(b) are identical reciprocal $N$-way power combiners with output ports numbered as port 1, and input ports numbered as ports 2 to $N+1$.

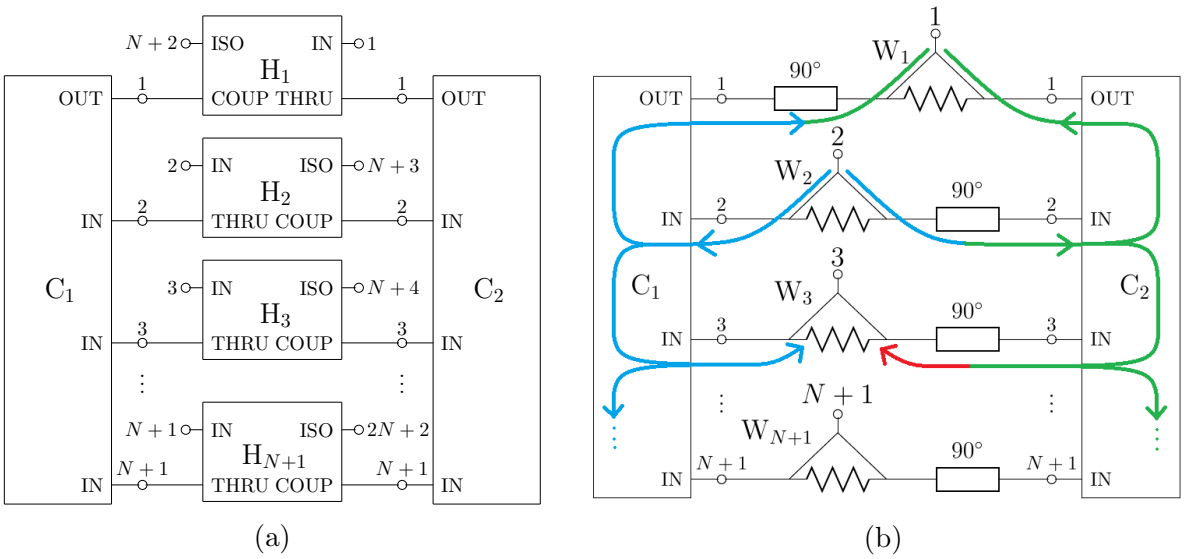


Figure 3.1: (a) An implementation of a compound power combiner using two $N$-way power combiners and $N+1$ 3 dB 90° hybrid couplers, and (b) an implementation using 2 $N$-way power combiners, $N+1$ Wilkinson combiners, and $N+1$ 90° delay lines. The coloured lines in (b) give an indication of the relative phases of the signals. Green lags blue by 90°, red lags green by 90°, and thus red lags blue by 180°.

Wilkinson combiners are used both as combiners and dividers, but will be referred to only as combiners for convenience. The Wilkinson combiners are numbered $W_1$ to $W_{N+1}$, and are all identical 3 dB 2-way combiners with isolated input ports and the same center frequency as $C_1$ and $C_2$. The unconnected ports of the network in Fig. 3.1(b) are numbered 1 to $N+1$, where port 1 is the output port and ports 2 to $N+1$ are input ports of the compound power combiner. Consider the path of a signal from an input port to the output port, as well as to any other input port. These signal paths are indicated using coloured lines in Fig. 3.1(b). Refer to the caption of Fig. 3.1 for a description of the colours. The signal from each of the input ports is split equally by a Wilkinson combiner and a 90° phase shift added on the path to $C_2$, whereas no phase shift is added on the path to $C_1$. This means that two identical modes are excited in $C_1$ (blue) and $C_2$ (green) by a signal at an input port, with the mode in $C_2$ lagging by 90°. A 90° phase shift is added at port 1 of $C_1$ (now also green), so that the output signals from $C_1$ and $C_2$ can be added in phase by $W_1$. In contrast, signals coming out of any of the input ports of $C_2$ get another 90° phase shift (red), whereas no phase shift is added at the input ports of $C_1$ (blue). This means that the signals at all of the Wilkinson combiners attached to input ports of $C_1$ and $C_2$ are 180° out of phase and are dissipated in the isolation loads of the Wilkinson combiners, isolating the input ports from each other. A similar argument can be made to show that the compound power combiner also works as a power divider, and is thus reciprocal, as long as the underlying combiners are reciprocal.

### 3.2.1 General S-parameter Proof

A proof using the S-parameter matrices of a general $N$-way power combiner and ideal 3 dB 90° hybrid coupler is presented in this section. The S-parameter matrix of the $N$-way combiner shown in Fig. 3.2(a) is given by

$$\mathbf{S_C} = \begin{bmatrix} S^{\mathrm{C}}_{11} & S^{\mathrm{C}}_{12} & S^{\mathrm{C}}_{13} & \cdots & S^{\mathrm{C}}_{1,N+1} \\ S^{\mathrm{C}}_{12} & S^{\mathrm{C}}_{22} & S^{\mathrm{C}}_{23} & \cdots & S^{\mathrm{C}}_{2,N+1} \\ S^{\mathrm{C}}_{13} & S^{\mathrm{C}}_{23} & S^{\mathrm{C}}_{33} & \cdots & S^{\mathrm{C}}_{3,N+1} \\ \vdots & \vdots & \vdots & \ddots & \vdots \\ S^{\mathrm{C}}_{1,N+1} & S^{\mathrm{C}}_{2,N+1} & S^{\mathrm{C}}_{3,N+1} & \cdots & S^{\mathrm{C}}_{N+1,N+1} \end{bmatrix}. \tag{3.1}$$

Ports 2 to $N+1$ are the input ports of the combiner, and port 1 is the output port. Note that $S^{\mathrm{C}}_{21}$ has been replaced with $S^{\mathrm{C}}_{12}$ and $S^{\mathrm{C}}_{32}$ with $S^{\mathrm{C}}_{23}$, etc. since it is assumed that the combiner is reciprocal. Also consider the S-parameter matrix of the 3 dB 90° hybrid coupler shown in Fig. 3.2(b) that is given by

$$\mathbf{S_H} = -\frac{1}{\sqrt{2}} \begin{bmatrix} 0 & j & 1 & 0 \\ j & 0 & 0 & 1 \\ 1 & 0 & 0 & j \\ 0 & 1 & j & 0 \end{bmatrix}. \tag{3.2}$$

A new component with $4N+4$ ports is created, as shown in Fig. 3.3(a), by using one coupler with the port mapping shown in Fig. 3.2(c) and $N$ copies of the coupler with the port mapping shown in Fig. 3.2(d), resulting in the following S-parameter matrix:

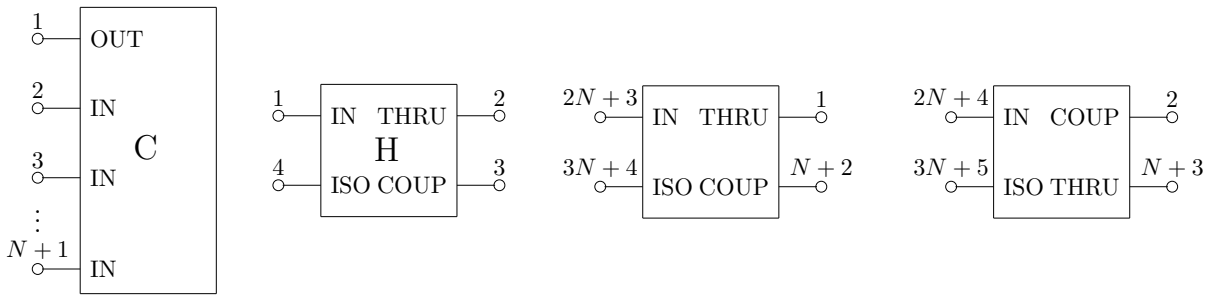


(a) (b) (c) (d)

Figure 3.2: A diagram of an $N$-way combiner (labelled C) is shown in (a) and a 90° hybrid coupler (labelled H) in (b). The hybrid coupler with the port mapping used with the output port of the combiner is shown in (c), and the hybrid coupler with the port mapping used for the input ports of the combiner is shown in (d).

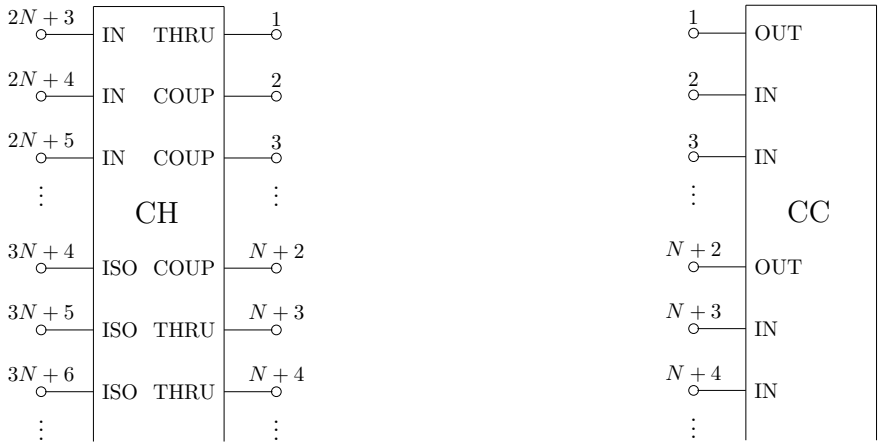


(a) (b)

Figure 3.3: The combination of $N+1$ hybrid couplers (labelled CH) is shown in (a), and the combination of two $N$-way combiners (labelled CC) is shown in (b).

$$\mathbf{S_{CH}} = \begin{bmatrix} \mathbf{0} & \mathbf{S_2} \\ \mathbf{S}_3 & \mathbf{0} \end{bmatrix} , \tag{3.3}$$

with

$$\mathbf{S_2} = \mathbf{S_3} = \begin{bmatrix} \mathbf{A} & \mathbf{B} \\ \mathbf{B} & \mathbf{A} \end{bmatrix} , \tag{3.4}$$

$$\mathbf{A} = -\frac{1}{\sqrt{2}} \begin{bmatrix} j & 0 & 0 & \cdots & 0 \\ 0 & 1 & 0 & \cdots & 0 \\ 0 & 0 & 1 & \cdots & 0 \\ \vdots & \vdots & \vdots & \ddots & \vdots \\ 0 & 0 & 0 & \cdots & 1 \end{bmatrix} , \tag{3.5}$$

and

$$\mathbf{B} = -\frac{1}{\sqrt{2}} \begin{bmatrix} 1 & 0 & 0 & \cdots & 0 \\ 0 & j & 0 & \cdots & 0 \\ 0 & 0 & j & \cdots & 0 \\ \vdots & \vdots & \vdots & \ddots & \vdots \\ 0 & 0 & 0 & \cdots & j \end{bmatrix} . \tag{3.6}$$

Similarly, a new component with $2N+2$ ports is created, as shown in Fig. 3.3(b), by using two copies of the combiner, resulting in the following S-parameter matrix:

$$\mathbf{S_{CC}} = \begin{bmatrix} \mathbf{S_C} & \mathbf{0} \\ \mathbf{0} & \mathbf{S_C} \end{bmatrix} . \tag{3.7}$$

The combination of the two combiners [Fig. 3.3(b)] can now be cascaded with the combination of hybrid couplers [Fig. 3.3(a)] to form the compound power combiner. This is accomplished by connecting port 1 of the combiners to port 1 of the couplers, etc. up to ports $2N+2$. The resulting device will have $2N+2$ unconnected ports. This operation is reflected in the S-parameters by cascading the S-parameter matrices using the method presented in [55]. The resulting S-parameter matrix of the compound power combiner is then equal to

$$\begin{aligned} \mathbf{S} &= \mathbf{S_3 S_{CC} S_2} \\ &= \begin{bmatrix} \mathbf{A} & \mathbf{B} \\ \mathbf{B} & \mathbf{A} \end{bmatrix} \begin{bmatrix} \mathbf{S_C} & \mathbf{0} \\ \mathbf{0} & \mathbf{S_C} \end{bmatrix} \begin{bmatrix} \mathbf{A} & \mathbf{B} \\ \mathbf{B} & \mathbf{A} \end{bmatrix} \\ &= \begin{bmatrix} \mathbf{S_D} & \mathbf{S_E} \\ \mathbf{S_E} & \mathbf{S_D} \end{bmatrix} , \end{aligned}$$

where

$$\mathbf{S_D} = \mathbf{A S_C A} + \mathbf{B S_C B} = j \begin{bmatrix} 0 & S_{12}^{\mathrm{C}} & S_{13}^{\mathrm{C}} & \cdots & S_{1,N+1}^{\mathrm{C}} \\ S_{12}^{\mathrm{C}} & 0 & 0 & \cdots & 0 \\ S_{13}^{\mathrm{C}} & 0 & 0 & \cdots & 0 \\ \vdots & \vdots & \vdots & \ddots & \vdots \\ S_{1,N+1}^{\mathrm{C}} & 0 & 0 & \cdots & 0 \end{bmatrix} , \tag{3.8}$$

and

$$\mathbf{S_E} = \mathbf{A S_C B} + \mathbf{B S_C A} = j \begin{bmatrix} S_{11}^{\mathrm{C}} & 0 & 0 & \cdots & 0 \\ 0 & S_{22}^{\mathrm{C}} & S_{23}^{\mathrm{C}} & \cdots & S_{2,N+1}^{\mathrm{C}} \\ 0 & S_{23}^{\mathrm{C}} & S_{33}^{\mathrm{C}} & \cdots & S_{3,N+1}^{\mathrm{C}} \\ \vdots & \vdots & \vdots & \ddots & \vdots \\ 0 & S_{2,N+1}^{\mathrm{C}} & S_{3,N+1}^{\mathrm{C}} & \cdots & S_{N+1,N+1}^{\mathrm{C}} \end{bmatrix} . \tag{3.9}$$

The complete S-parameter matrix of the compound power combiner is thus

$$\mathbf{S} = j \left[\begin{array}{ccccc|ccccc} 0 & S^{\mathrm{C}}_{12} & S^{\mathrm{C}}_{13} & \cdots & S^{\mathrm{C}}_{1,N+1} & S^{\mathrm{C}}_{11} & 0 & 0 & \cdots & 0 \\ S^{\mathrm{C}}_{12} & 0 & 0 & \cdots & 0 & 0 & S^{\mathrm{C}}_{22} & S^{\mathrm{C}}_{23} & \cdots & S^{\mathrm{C}}_{2,N+1} \\ S^{\mathrm{C}}_{13} & 0 & 0 & \cdots & 0 & 0 & S^{\mathrm{C}}_{23} & S^{\mathrm{C}}_{33} & \cdots & S^{\mathrm{C}}_{3,N+1} \\ \vdots & \vdots & \vdots & \ddots & \vdots & \vdots & \vdots & \vdots & \ddots & \vdots \\ S^{\mathrm{C}}_{1,N+1} & 0 & 0 & \cdots & 0 & 0 & S^{\mathrm{C}}_{2,N+1} & S^{\mathrm{C}}_{3,N+1} & \cdots & S^{\mathrm{C}}_{N+1,N+1} \\ \hline S^{\mathrm{C}}_{11} & 0 & 0 & \cdots & 0 & 0 & S^{\mathrm{C}}_{12} & S^{\mathrm{C}}_{13} & \cdots & S^{\mathrm{C}}_{1,N+1} \\ 0 & S^{\mathrm{C}}_{22} & S^{\mathrm{C}}_{23} & \cdots & S^{\mathrm{C}}_{2,N+1} & S^{\mathrm{C}}_{12} & 0 & 0 & \cdots & 0 \\ 0 & S^{\mathrm{C}}_{23} & S^{\mathrm{C}}_{33} & \cdots & S^{\mathrm{C}}_{3,N+1} & S^{\mathrm{C}}_{13} & 0 & 0 & \cdots & 0 \\ \vdots & \vdots & \vdots & \ddots & \vdots & \vdots & \vdots & \vdots & \ddots & \vdots \\ 0 & S^{\mathrm{C}}_{2,N+1} & S^{\mathrm{C}}_{3,N+1} & \cdots & S^{\mathrm{C}}_{N+1,N+1} & S^{\mathrm{C}}_{1,N+1} & 0 & 0 & \cdots & 0 \end{array}\right]. \quad (3.10)$$

Ports $2N+3$ to $4N+4$ of the combination of hybrid couplers [Fig. 3.3(a)] are now ports 1 to $2N+2$ of the compound power combiner. Since all the individual components used to construct the compound power combiner are lossless and reciprocal, the compound power combiner must also be lossless and reciprocal. Additionally, we can see from (3.10) that all ports are perfectly matched, and that there is perfect isolation between all combinations of the ports numbered from 2 to $N+1$, as well as between all combinations of the ports numbered from $N+3$ to $2N+2$. We have thus constructed an $N$-way combiner with $2N+2$ ports that has all the characteristics of an ideal combiner. Alternatively, we can terminate ports $N+2$ to $2N+2$ in matched loads and consider them to be internal losses, in which case the compound power combiner will now be lossy with an S-parameter matrix equal to $\mathbf{S_D}$ in (3.8).

## 3.3 Design Procedure

The design procedure simply consists of designing a power combiner and a 3 dB 90° hybrid coupler with the same port impedances and frequency bands, and connecting multiple copies of these components as shown in Fig. 3.1(a). However, it may be difficult to know when the individual components perform well enough to provide satisfactory isolation, since the power combiner and hybrid coupler are designed separately. It may be useful to the designer to have an estimate of the worst-case isolation that a given combination of combiner and coupler may have, as well as offer some insight into the impact of specific parameters on the overall performance of the compound power combiner.

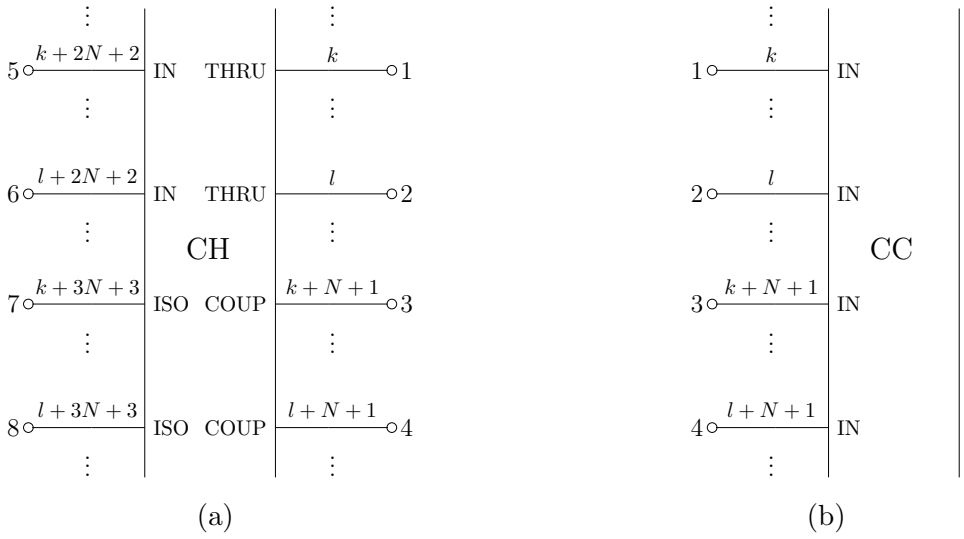


Figure 3.4: The combination of $N+1$ hybrid couplers is shown in (a), and the combination of two $N$-way combiners is shown in (b).

### 3.3.1 Worst-Case Performance Estimate

Consider Fig. 3.4, where the components labelled CH and CC are the same components as in Fig. 3.3, but with only the ports that are relevant to the inputs visible in the diagrams. Port $k$ of component CC is any input port of one of its underlying combiners, port $l$ is any other input port of the same underlying combiner, and ports $k+N+1$ and $l+N+1$ are the corresponding input ports of the other underlying combiner. Ports $k$, $l$, $k+N+1$, and $l+N+1$ of components CH and CC are renumbered to ports 1, 2, 3, and 4, and ports with the same numbers are connected to each other. Ports $k+2N+2$, $l+2N+2$, $k+3N+3$, and $l+3N+3$ of component CH are renumbered to ports 5, 6, 7, and 8, and are left unconnected – these ports will be ports 1, 2, 3, and 4 of the cascaded network. All other ports not shown in Fig. 3.4 are terminated in perfectly matched loads, reducing the entire network to a 4-port network, of which the S-parameter matrix can now more easily be determined.

Since component CC consists of two identical combiners with S-parameter matrices equal to (3.1), and shown in Fig. 3.2(a), the resulting S-parameter matrix for component CC is:

$$\mathbf{S_{CC}} = \begin{bmatrix} S^{\mathrm{C}}_{kk} & S^{\mathrm{C}}_{kl} & 0 & 0 \\ S^{\mathrm{C}}_{kl} & S^{\mathrm{C}}_{ll} & 0 & 0 \\ 0 & 0 & S^{\mathrm{C}}_{kk} & S^{\mathrm{C}}_{kl} \\ 0 & 0 & S^{\mathrm{C}}_{kl} & S^{\mathrm{C}}_{ll} \end{bmatrix} . \tag{3.11}$$

Component CH consists of $N+1$ hybrid couplers as shown in Fig. 3.2(b) with S-parameter

matrices equal to:

$$\mathbf{S_H} = \begin{bmatrix} S_{11}^{\mathrm{H}} & S_{12}^{\mathrm{H}} & S_{13}^{\mathrm{H}} & S_{14}^{\mathrm{H}} \\ S_{12}^{\mathrm{H}} & S_{22}^{\mathrm{H}} & S_{23}^{\mathrm{H}} & S_{24}^{\mathrm{H}} \\ S_{13}^{\mathrm{H}} & S_{23}^{\mathrm{H}} & S_{33}^{\mathrm{H}} & S_{34}^{\mathrm{H}} \\ S_{14}^{\mathrm{H}} & S_{24}^{\mathrm{H}} & S_{34}^{\mathrm{H}} & S_{44}^{\mathrm{H}} \end{bmatrix}. \tag{3.12}$$

By applying the port mapping as shown in Fig. 3.2(d), the S-parameter matrix of component CH can be written as:

$$\mathbf{S_{CH}} = \left[\begin{array}{cccc|cccc} S_{22}^{\mathrm{H}} & 0 & S_{23}^{\mathrm{H}} & 0 & S_{12}^{\mathrm{H}} & 0 & S_{24}^{\mathrm{H}} & 0 \\ 0 & S_{22}^{\mathrm{H}} & 0 & S_{23}^{\mathrm{H}} & 0 & S_{12}^{\mathrm{H}} & 0 & S_{24}^{\mathrm{H}} \\ S_{23}^{\mathrm{H}} & 0 & S_{33}^{\mathrm{H}} & 0 & S_{13}^{\mathrm{H}} & 0 & S_{34}^{\mathrm{H}} & 0 \\ 0 & S_{23}^{\mathrm{H}} & 0 & S_{33}^{\mathrm{H}} & 0 & S_{13}^{\mathrm{H}} & 0 & S_{34}^{\mathrm{H}} \\ \hline S_{12}^{\mathrm{H}} & 0 & S_{13}^{\mathrm{H}} & 0 & S_{11}^{\mathrm{H}} & 0 & S_{14}^{\mathrm{H}} & 0 \\ 0 & S_{12}^{\mathrm{H}} & 0 & S_{13}^{\mathrm{H}} & 0 & S_{11}^{\mathrm{H}} & 0 & S_{14}^{\mathrm{H}} \\ S_{24}^{\mathrm{H}} & 0 & S_{34}^{\mathrm{H}} & 0 & S_{14}^{\mathrm{H}} & 0 & S_{44}^{\mathrm{H}} & 0 \\ 0 & S_{24}^{\mathrm{H}} & 0 & S_{34}^{\mathrm{H}} & 0 & S_{14}^{\mathrm{H}} & 0 & S_{44}^{\mathrm{H}} \end{array}\right]. \tag{3.13}$$

In order to calculate the input reflection coefficient and isolation between any pair of input ports of the compound power combiner, the S-parameter matrices $\mathbf{S_{CH}}$ and $\mathbf{S_{CC}}$ need to be cascaded. This can be done by using the following matrix equation:

$$\mathbf{S} = \mathbf{S_3 S_5} \left(\mathbf{I} - \mathbf{S_1 S_5}\right)^{-1} \mathbf{S_2} + \mathbf{S_4}, \tag{3.14}$$

as given in [55]. The matrices in (3.14) are all $4 \times 4$ matrices, so that

$$\mathbf{S_{CH}} = \begin{bmatrix} \mathbf{S_1} & \mathbf{S_2} \\ \mathbf{S_3} & \mathbf{S_4} \end{bmatrix}, \tag{3.15}$$

$$\mathbf{S_5} = \mathbf{S_{CC}}, \tag{3.16}$$

and $\mathbf{I}$ is the $4 \times 4$ identity matrix. The S-parameter matrix of the cascaded network will have the following form:

$$\mathbf{S} = \begin{bmatrix} S_{11} & S_{12} & S_{13} & S_{14} \\ S_{21} & S_{22} & S_{23} & S_{24} \\ S_{31} & S_{32} & S_{33} & S_{34} \\ S_{41} & S_{42} & S_{43} & S_{44} \end{bmatrix}. \tag{3.17}$$

We only need to find expressions for $S_{11}$ ($S_{kk}$) and $S_{12}$ ($S_{kl}$) of the cascaded network, since ports 1 (previously port 5) and 2 (previously port 6) of the cascaded network are any two different input ports of the compound power combiner, and ports 3 (previously port 7) and 4 (previously port 8) are where their corresponding isolation loads should be

connected.

If we rewrite (3.14) as

$$\mathbf{S} = \mathbf{S_X}\mathbf{S_Y} + \mathbf{S_4}, \tag{3.18}$$

where

$$\mathbf{S_X} = \mathbf{S_3}\mathbf{S_5}, \tag{3.19}$$

and

$$\mathbf{S_Y} = (\mathbf{I} - \mathbf{S_1}\mathbf{S_5})^{-1}\mathbf{S_2}, \tag{3.20}$$

we can determine $S_{11}$ by multiplying row 1 of $\mathbf{S_X}$ with column 1 of $\mathbf{S_Y}$ and adding $(\mathbf{S_4})_{11}$, and $S_{12}$ by multiplying row 1 of $\mathbf{S_X}$ with column 2 of $\mathbf{S_Y}$ and adding $(\mathbf{S_4})_{12}$. We will first determine row 1 of $\mathbf{S_X}$:

$$\mathbf{S_{X(row1)}} = \begin{bmatrix} S_{kk}^{\mathrm{C}} S_{12}^{\mathrm{H}} & S_{kl}^{\mathrm{C}} S_{12}^{\mathrm{H}} & S_{kk}^{\mathrm{C}} S_{13}^{\mathrm{H}} & S_{kl}^{\mathrm{C}} S_{13}^{\mathrm{H}} \end{bmatrix} . \tag{3.21}$$

The next step is to determine columns 1 and 2 of $\mathbf{S_Y}$. The following approximation can be made using a truncated Neumann series expansion

$$(\mathbf{I} - \mathbf{S_1}\mathbf{S_5})^{-1} \approx \mathbf{I} + \mathbf{S_1}\mathbf{S_5}, \tag{3.22}$$

since the components used here are all passive components, and their S-parameter matrices thus

$$|\mathbf{S}| \leq 1. \tag{3.23}$$

We can then approximate $\mathbf{S_Y}$ using

$$\mathbf{S_Y} \approx (\mathbf{I} + \mathbf{S_1}\mathbf{S_5})\,\mathbf{S_2}. \tag{3.24}$$

Column 1 of $\mathbf{S_Y}$ is thus:

$$\mathbf{S_{Y(col1)}} \approx \begin{bmatrix} S_{12}^{\mathrm{H}} \left(1 + S_{kk}^{\mathrm{C}} S_{22}^{\mathrm{H}}\right) + S_{13}^{\mathrm{H}} S_{kk}^{\mathrm{C}} S_{23}^{\mathrm{H}} \\ S_{12}^{\mathrm{H}} S_{kl}^{\mathrm{C}} S_{22}^{\mathrm{H}} + S_{13}^{\mathrm{H}} S_{kl}^{\mathrm{C}} S_{23}^{\mathrm{H}} \\ S_{12}^{\mathrm{H}} S_{kk}^{\mathrm{C}} S_{23}^{\mathrm{H}} + S_{13}^{\mathrm{H}} \left(1 + S_{kk}^{\mathrm{C}} S_{33}^{\mathrm{H}}\right) \\ S_{12}^{\mathrm{H}} S_{kl}^{\mathrm{C}} S_{23}^{\mathrm{H}} + S_{13}^{\mathrm{H}} S_{kl}^{\mathrm{C}} S_{33}^{\mathrm{H}} \end{bmatrix} , \tag{3.25}$$

and column 2:

$$\mathbf{S_{Y(col2)}} \approx \begin{bmatrix} S_{12}^{\mathrm{H}} S_{kk}^{\mathrm{C}} S_{22}^{\mathrm{H}} + S_{13}^{\mathrm{H}} S_{kl}^{\mathrm{C}} S_{23}^{\mathrm{H}} \\ S_{12}^{\mathrm{H}} \left(1 + S_{ll}^{\mathrm{C}} S_{22}^{\mathrm{H}}\right) + S_{13}^{\mathrm{H}} S_{ll}^{\mathrm{C}} S_{23}^{\mathrm{H}} \\ S_{12}^{\mathrm{H}} S_{kl}^{\mathrm{C}} S_{23}^{\mathrm{H}} + S_{13}^{\mathrm{H}} S_{kl}^{\mathrm{C}} S_{33}^{\mathrm{H}} \\ S_{12}^{\mathrm{H}} S_{ll}^{\mathrm{C}} S_{23}^{\mathrm{H}} + S_{13}^{\mathrm{H}} \left(1 + S_{ll}^{\mathrm{C}} S_{33}^{\mathrm{H}}\right) \end{bmatrix} . \tag{3.26}$$

Now we can determine the input port reflection coefficient of the compound power com-

biner by performing the matrix multiplication as described earlier and simplifying:

$$\begin{aligned} S_{kk} = S_{11} &= \mathbf{S}_{\mathbf{X}(\text{row1})}\mathbf{S}_{\mathbf{Y}(\text{col1})} + (\mathbf{S_4})_{11} \\ &= [(S^{\text{C}}_{kk})^2 + (S^{\text{C}}_{kl})^2][2S^{\text{H}}_{12}S^{\text{H}}_{13}S^{\text{H}}_{23} + S^{\text{H}}_{22}(S^{\text{H}}_{12})^2 + S^{\text{H}}_{33}(S^{\text{H}}_{13})^2] \\ &\quad + S^{\text{C}}_{kk}\left[(S^{\text{H}}_{12})^2 + (S^{\text{H}}_{13})^2\right] + S^{\text{H}}_{11}. \end{aligned} \tag{3.27}$$

An upper limit can be found by taking the absolute value and using the triangle inequality:

$$\begin{aligned} |S_{kk}| \leq |(S^{\text{C}}_{kk})^2 + (S^{\text{C}}_{kl})^2||2S^{\text{H}}_{12}S^{\text{H}}_{13}S^{\text{H}}_{23} + S^{\text{H}}_{22}(S^{\text{H}}_{12})^2 + S^{\text{H}}_{33}(S^{\text{H}}_{13})^2| \\ + |S^{\text{C}}_{kk}||(S^{\text{H}}_{12})^2 + (S^{\text{H}}_{13})^2| + |S^{\text{H}}_{11}|. \end{aligned} \tag{3.28}$$

If the S-parameters of the combiner used in component CC are not known, (3.28) can be simplified and used for a worst-case estimate. This can be done by using values for $|S^{\text{C}}_{kk}|$ and $|S^{\text{C}}_{kl}|$ that will result in the highest possible value for $|S_{kk}|$, which is $|S^{\text{C}}_{kk}| = |S^{\text{C}}_{kl}| = 1$, since the combiner is a passive device and therefore $|S^{\text{C}}_{kk}|$ and $|S^{\text{C}}_{kl}|$ cannot be greater than 1. The upper limit then becomes

$$\begin{aligned} |S_{kk}| \leq 2|2S^{\text{H}}_{12}S^{\text{H}}_{13}S^{\text{H}}_{23} + S^{\text{H}}_{22}(S^{\text{H}}_{12})^2 + S^{\text{H}}_{33}(S^{\text{H}}_{13})^2| \\ + |(S^{\text{H}}_{12})^2 + (S^{\text{H}}_{13})^2| + |S^{\text{H}}_{11}|. \end{aligned} \tag{3.29}$$

Note that both $|S^{\text{C}}_{kk}|$ and $|S^{\text{C}}_{kl}|$ will typically be much smaller than 1, resulting in better performance than the worst-case estimate. If it can be assumed that ports $l$, $k+N+1$ and $l+N+1$ – ports 2, 3 and 4, formerly labelled 6, 7 and 8 in Fig. 3.4(a) – of the compound power combiner are terminated in perfectly matched loads, and the coupler that is used is symmetrical, i.e. its S-parameters remain unchanged if any other port is used as an input port, (3.29) can be simplified further by taking $S^{\text{H}}_{23} = S^{\text{H}}_{41}$ and $S^{\text{H}}_{22} = S^{\text{H}}_{33} = S^{\text{H}}_{11}$. This results in

$$|S_{kk}| \leq 4|S^{\text{H}}_{21}S^{\text{H}}_{31}S^{\text{H}}_{41}| + |1 + 2S^{\text{H}}_{11}||(S^{\text{H}}_{21})^2 + (S^{\text{H}}_{31})^2| + |S^{\text{H}}_{11}|, \tag{3.30}$$

for which the S-parameters can be determined from a single full-wave simulation with only one port stimulated.

The input port isolation of the compound power combiner can be determined in a similar way by performing the described multiplication and simplifying:

$$\begin{aligned} S_{kl} = S_{12} &= \mathbf{S}_{\mathbf{X}(\text{row1})}\mathbf{S}_{\mathbf{Y}(\text{col2})} + (\mathbf{S_4})_{12} \\ &= S^{\text{C}}_{kl}(S^{\text{C}}_{kk} + S^{\text{C}}_{ll})[2S^{\text{H}}_{12}S^{\text{H}}_{13}S^{\text{H}}_{23} + S^{\text{H}}_{22}(S^{\text{H}}_{12})^2 + S^{\text{H}}_{33}(S^{\text{H}}_{13})^2] \\ &\quad + S^{\text{C}}_{kl}[(S^{\text{H}}_{12})^2 + (S^{\text{H}}_{13})^2] + 0. \end{aligned} \tag{3.31}$$

An upper limit can be found by taking the absolute value and using the triangle inequality:

$$|S_{kl}| \leq |S^{\mathrm{C}}_{kl}||S^{\mathrm{C}}_{kk} + S^{\mathrm{C}}_{ll}||2S^{\mathrm{H}}_{12}S^{\mathrm{H}}_{13}S^{\mathrm{H}}_{23} + S^{\mathrm{H}}_{22}(S^{\mathrm{H}}_{12})^2 + S^{\mathrm{H}}_{33}(S^{\mathrm{H}}_{13})^2| + |S^{\mathrm{C}}_{kl}||(S^{\mathrm{H}}_{12})^2 + (S^{\mathrm{H}}_{13})^2|. \tag{3.32}$$

If the S-parameters of the combiner used in component CC are not known, (3.28) can be simplified by making the assumption that in the worst-case, $|S^{\mathrm{C}}_{kk}| = |S^{\mathrm{C}}_{kl}| = |S^{\mathrm{C}}_{ll}| = 1$. The upper limit then becomes

$$|S_{kl}| \leq 2|2S^{\mathrm{H}}_{12}S^{\mathrm{H}}_{13}S^{\mathrm{H}}_{23} + S^{\mathrm{H}}_{22}(S^{\mathrm{H}}_{12})^2 + S^{\mathrm{H}}_{33}(S^{\mathrm{H}}_{13})^2| + |(S^{\mathrm{H}}_{12})^2 + (S^{\mathrm{H}}_{13})^2|. \tag{3.33}$$

If it can be assumed that ports $k+N+1$ and $l+N+1$ – ports 3 and 4, formerly labelled 7 and 8 in Fig. 3.4(a) – of the compound power combiner are terminated in perfectly matched loads, and the coupler that is used is symmetrical, i.e. its S-parameters remain unchanged if any other port is used as an input port, (3.33) can be simplified further by taking $S^{\mathrm{H}}_{23} = S^{\mathrm{H}}_{41}$ and $S^{\mathrm{H}}_{22} = S^{\mathrm{H}}_{33} = S^{\mathrm{H}}_{11}$. This results in

$$|S_{kl}| \leq 4|S^{\mathrm{H}}_{21}S^{\mathrm{H}}_{31}S^{\mathrm{H}}_{41}| + |1 + 2S^{\mathrm{H}}_{11}||(S^{\mathrm{H}}_{21})^2 + (S^{\mathrm{H}}_{31})^2|, \tag{3.34}$$

for which the S-parameters can be determined from a single full-wave simulation with only one port stimulated.

### 3.3.2 Interpretation of the Worst-Case Performance Estimate

Equations that can be used to estimate the worst-case input port reflection coefficient, (3.28 - 3.30), and input port isolation, (3.32 - 3.34), have been derived. Note that while these equations are approximations and do not take any mismatches between the couplers and the isolation loads into account, they do offer some insight into the effects that specific parameters of a coupler may have on the performance of a compound power combiner. The input port reflection coefficient and isolation of the underlying power combiner also have an effect on the performance of the compound power combiner. However, the requirements for a design for a specific application may dictate the type of underlying power combiners to be used in the realisation of the compound power combiner, and these combiners may often have poor input port reflection coefficients and isolation, as is the case with reactive power combiners. We will thus focus on the specifications of the couplers for improved performance of the compound power combiner.

Consider (3.29), the equation for the input port reflection coefficient, where any depen-

dence on the underlying power combiner parameters has been removed by assuming a worst-case performance of $|S^{\mathrm{C}}_{kk}| = |S^{\mathrm{C}}_{kl}| = |S^{\mathrm{C}}_{ll}| = 1$. The equation is dependent on the $S^{\mathrm{H}}_{11}$, $S^{\mathrm{H}}_{22}$, $S^{\mathrm{H}}_{33}$, $S^{\mathrm{H}}_{23}$, $S^{\mathrm{H}}_{12}$, and $S^{\mathrm{H}}_{13}$ parameters of the coupler. If the coupler is designed reasonably well, we can expect $S^{\mathrm{H}}_{11}$, $S^{\mathrm{H}}_{22}$, $S^{\mathrm{H}}_{33}$, and $S^{\mathrm{H}}_{23}$ to be much smaller than $S^{\mathrm{H}}_{12}$ and $S^{\mathrm{H}}_{13}$. Equation (3.29) will thus be dominated by the term containing the squares of those two parameters: $|(S^{\mathrm{H}}_{12})^2 + (S^{\mathrm{H}}_{13})^2|$. For an ideal coupler we have $S^{\mathrm{H}}_{12} = \frac{-1}{\sqrt{2}}$ and $S^{\mathrm{H}}_{13} = \frac{-j}{\sqrt{2}}$, which results in $|(\frac{-1}{\sqrt{2}})^2 + (\frac{-j}{\sqrt{2}})^2| = 0$. In fact, it can be shown that as long as $S^{\mathrm{H}}_{12}$ and $S^{\mathrm{H}}_{13}$ have equal amplitude and a 90° phase shift between them, this term will always be zero. Therefore, if we can assume that $S^{\mathrm{H}}_{11}$, $S^{\mathrm{H}}_{22}$, $S^{\mathrm{H}}_{33}$, and $S^{\mathrm{H}}_{23}$ are sufficiently small, the performance of the compound combiner may be improved by focussing on achieving as close as possible to a 3 dB split and a phase difference of 90° between the coupled and through ports. A similar argument can be made to show that the same holds true for the input port isolation of the compound power combiner.

## 3.4 Design Examples

Some example designs are presented in this section in order to demonstrate the effectiveness of the new isolation method, and the simulated results for each design compared to theoretical predictions. The last design example is constructed and measured.

### 3.4.1 Design 1

The purpose of the first design example is to show that the isolation method can be used with axially symmetric reactive combiners, such as conical combiners. A full S-parameter block of the conical combiner in Section 2.3.2.4 is calculated using CST MWS and used in Applied Wave Research (AWR) Microwave Office (MWO) with ideal 3 dB 90° hybrid couplers to construct a compound power combiner. The ideal couplers have ports matched perfectly to 50 Ω, infinite isolation and infinite bandwidth. Port 1 of the conical combiner is the output port and ports 2 to $N + 1$ are input ports. Port 1 of the hybrid coupler is the input port, port 2 the through port, port 3 the coupled (and 90° phase shifted) port, and port 4 the isolated port.

The obtained reflection coefficients $S_{11}$ and $S_{22}$, the transmission coefficient $S_{12}$, and the input port isolation are shown in Fig. 3.5. The amplitudes of $S_{12}$, $S_{13}$, etc. are unchanged, but a 90° phase shift is added when compared to the S-parameters of the conical combiner on its own. An improvement of roughly 50 dB in reflection coefficients and isolation is observed in comparison to the conical combiner on its own. The resulting

reflection coefficients and isolation are not infinite, because the conical combiner does not have perfect 50 Ω ports. This example shows that the new isolation method can theoretically be used with conical combiners and significantly improve their performance. These results are, however, unrealistic since ideal 3 dB 90° hybrid couplers with perfectly matched ports, infinite isolation and infinite bandwidth are used.

### 3.4.2 Design 2

The second design example consists of two 4-way rectangular waveguide power combiners with E-plane bends and junctions, and Riblet couplers [56] designed to operate at X-band. The combiner and couplers used in this design will be modelled by full-wave simulation and will therefore be a much more realistic example of an implementation of a compound power combiner using the new isolation method.

The 4-way rectangular waveguide power combiner consists of a series of E-plane bends and junctions, as shown in Fig. 3.6(a), which are simple to design and will not be analysed here. The S-parameters including the isolation of the waveguide combiner are shown in Figs. 3.6(b) and 3.6(c). The combiner has a maximum output port reflection coefficient ($S_{11}$) of better than −15 dB from 9 to 11 GHz, and a maximum input port reflection coefficient ($S_{22}$) of better than −2 dB across the simulated frequency band. The isolation between all the input ports except ports 2 and 3 is roughly 12 dB, and the minimum isolation between ports 2 and 3 is slightly better than 2 dB across the frequency band.

The Riblet coupler is also a well-known component and its design will therefore not be covered here. A 3D model of the coupler used in this design and its S-parameters are shown in Figs. 3.7(a) and 3.7(b). The coupler has an $S_{11}$ and $S_{14}$ of better than −25 dB

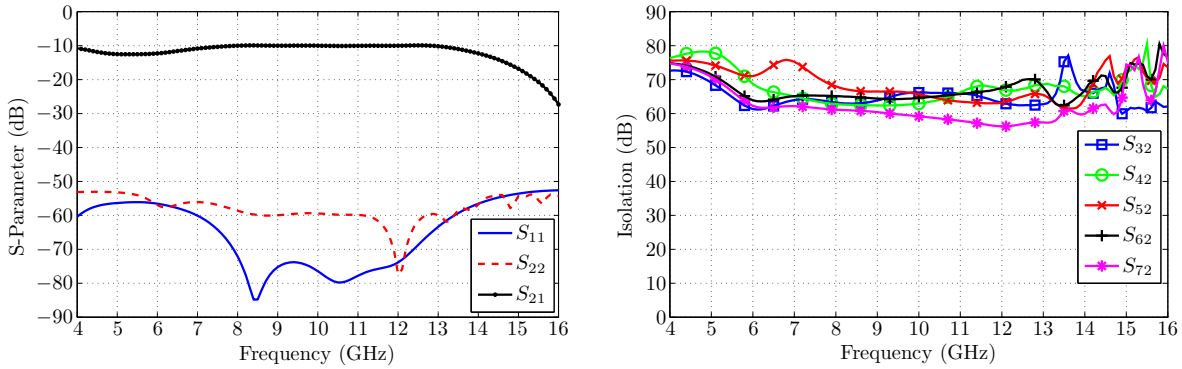


(a) (b)

Figure 3.5: (a) The reflection coefficients $S_{11}$ and $S_{22}$, and the transmission coefficient $S_{12}$; (b) the isolation.

and a maximum amplitude difference between ports 2 and 3 of less than 1 dB from 9 to 11 GHz. Fig. 3.7(c) shows the phase difference between ports 2 and 3, where a maximum deviation of less than 1.1° from 90° is achieved between 9 and 11 GHz. The worst-case input port reflection coefficient and isolation that the combination of this coupler and combiner may have is estimated using (3.30) and (3.34), and shown in Figs. 3.8(b) and 3.8(c). An estimated worst-case input port reflection coefficient and isolation of better than −14 dB and 15 dB between 9 and 11 GHz will be achieved, respectively.

After the combiner and coupler designs are completed, the next step is to simply connect the components together in the correct configuration, as shown in Fig. 3.1(a). A 3D model of the resulting structure and its full-wave simulation results are shown in Fig. 3.8. The simulated output port reflection coefficient ($S_{11}$) is better than −19 dB, the input port reflection coefficient ($S_{22}$) is better than −19 dB, and the minimum isolation is better than 23 dB from 9 to 11 GHz – a significant improvement on the 4-way waveguide combiner on its own. These simulated results are also in agreement with the estimated worst-case values $I_{\min}$ and $\Gamma_{\max}$.

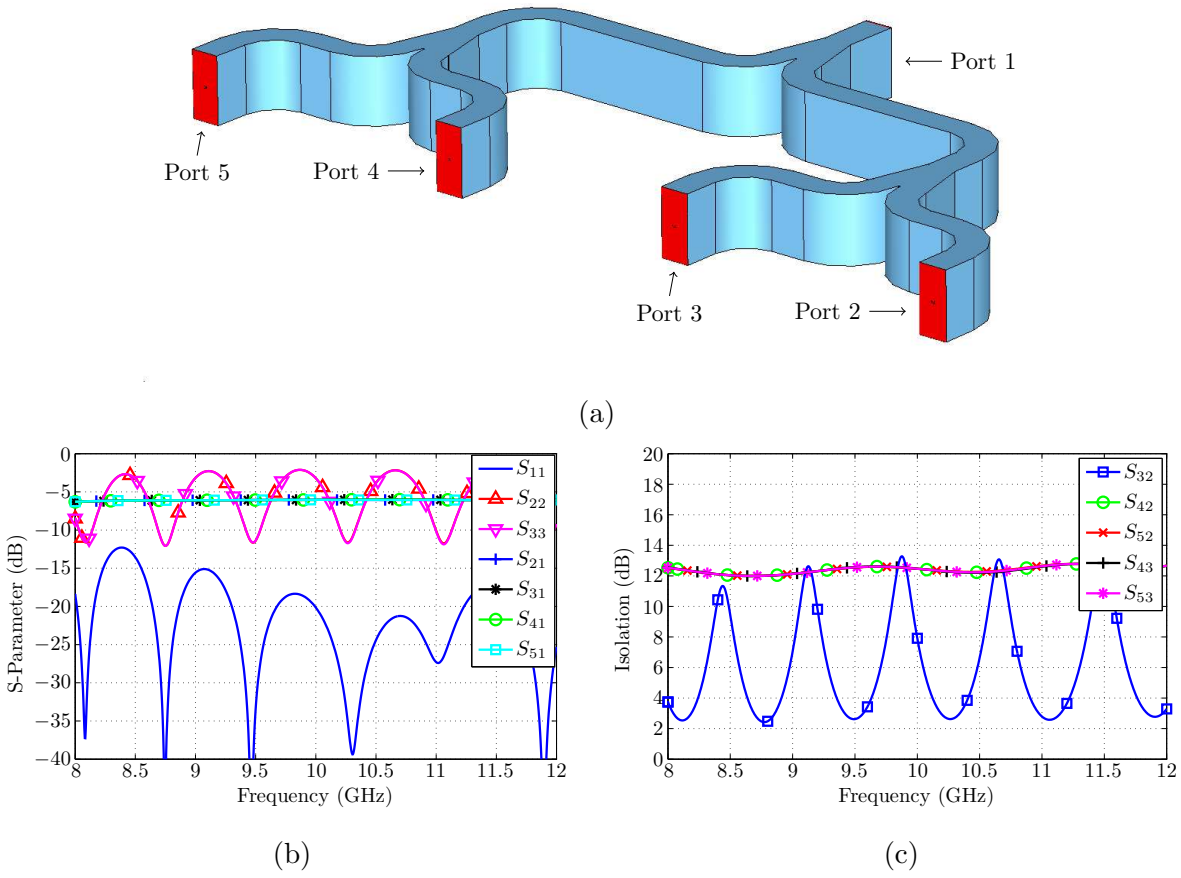


Figure 3.6: (a) A 3D CAD model of the waveguide combiner, and (b) and (c) its full-wave simulated results.

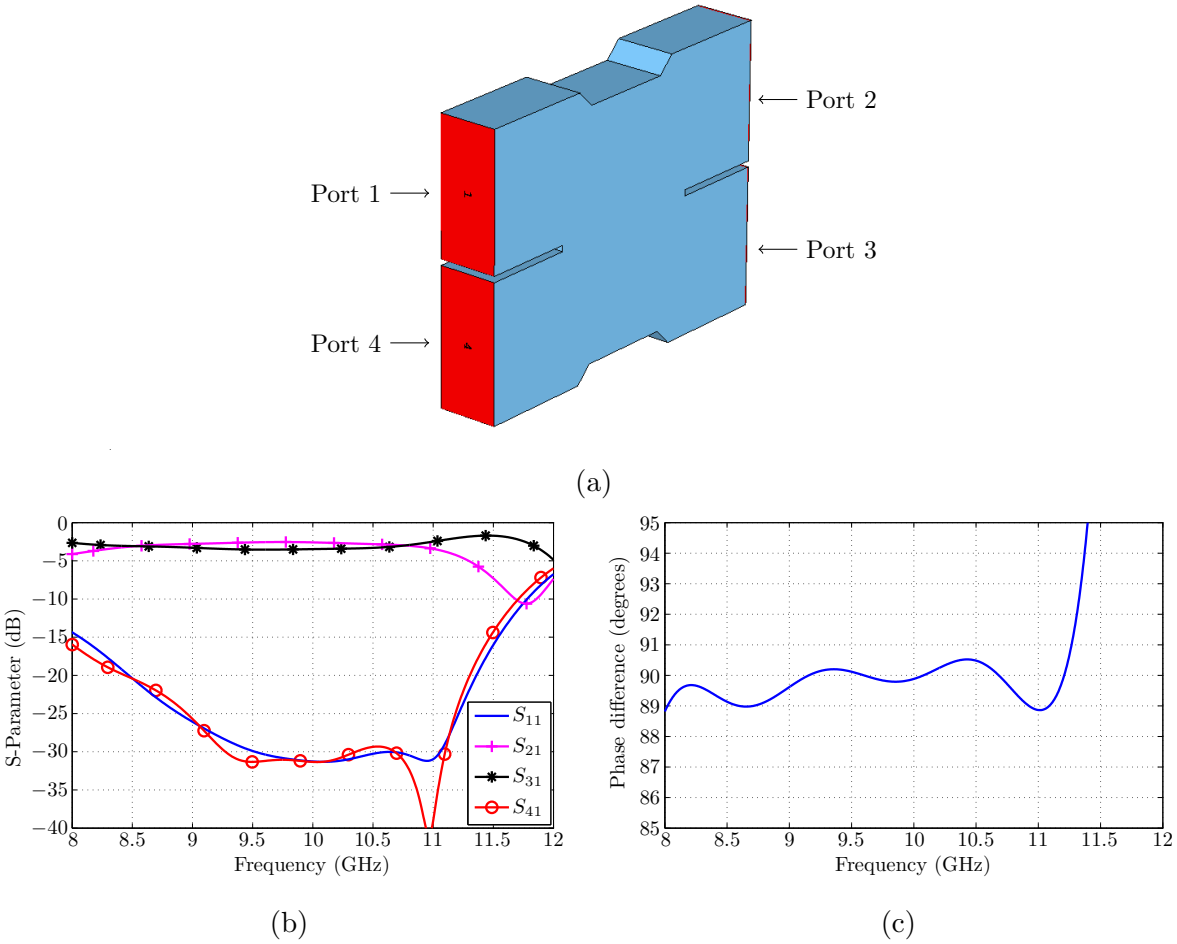


Figure 3.7: (a) A 3D CAD model of the Riblet coupler, and (b) and (c) its full-wave simulated results.

The ports in the full-wave simulation are all perfectly matched and do therefore not show the effect of using non-ideal isolation loads. It has been shown in [57] that waveguide terminations with reflection coefficients of better than −30 dB can be realised using resistive sheets. A similar rectangular waveguide absorbing termination is designed, as shown in Fig. 3.9(a), using the ECCOSORB MFS-124 material and a full-wave simulated reflection coefficient of better than −23 dB is obtained from 9 to 11 GHz, as shown in Fig. 3.9(b). Copies of the designed waveguide termination are attached to ports 7 to 10 of the compound power combiner and the entire structure simulated to include the effect of non-ideal isolation loads. The obtained results are shown in Fig. 3.10, where similar and at some frequencies superior performance is obtained compared to the case where perfectly matched ports are used. The input port reflection coefficients ($S_{22}$ and $S_{33}$) are better than −20 dB, the output port reflection coefficient ($S_{11}$) is better than −22 dB, and the isolation between all combinations of input ports is better than 20 dB from 9 to 11 GHz.

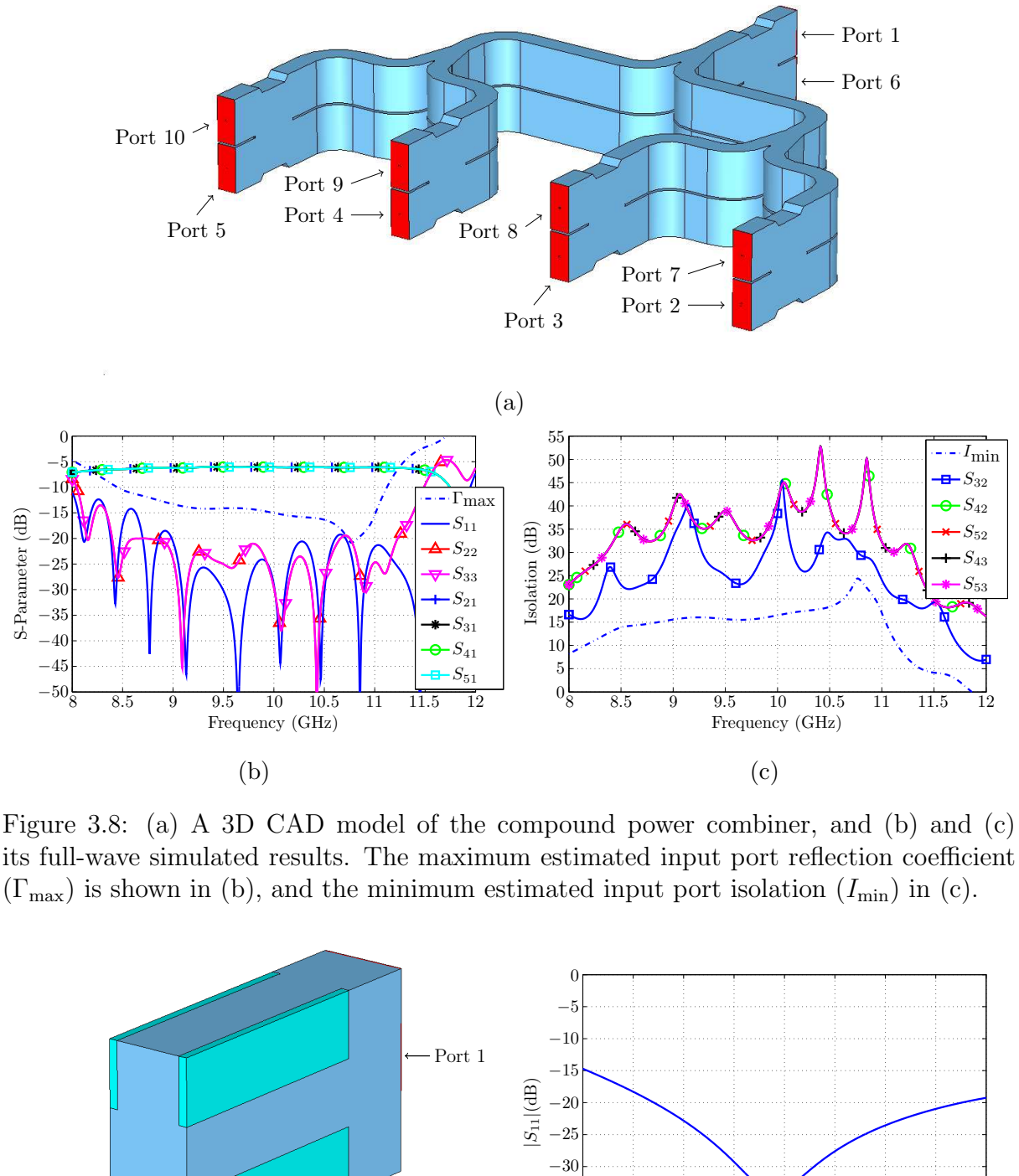


Figure 3.8: (a) A 3D CAD model of the compound power combiner, and (b) and (c) its full-wave simulated results. The maximum estimated input port reflection coefficient ($\Gamma_{\max}$) is shown in (b), and the minimum estimated input port isolation ($I_{\min}$) in (c).

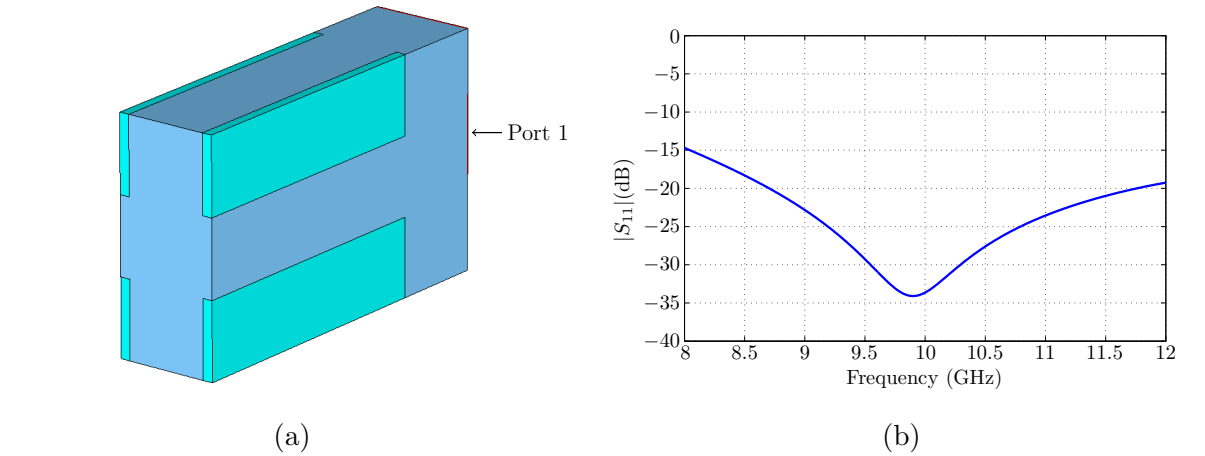


Figure 3.9: (a) A 3D CAD model of the waveguide termination, and (b) its full-wave simulated results. The blue colour represents vacuum and the cyan represents the EC-COSORB MFS-124 absorber material.

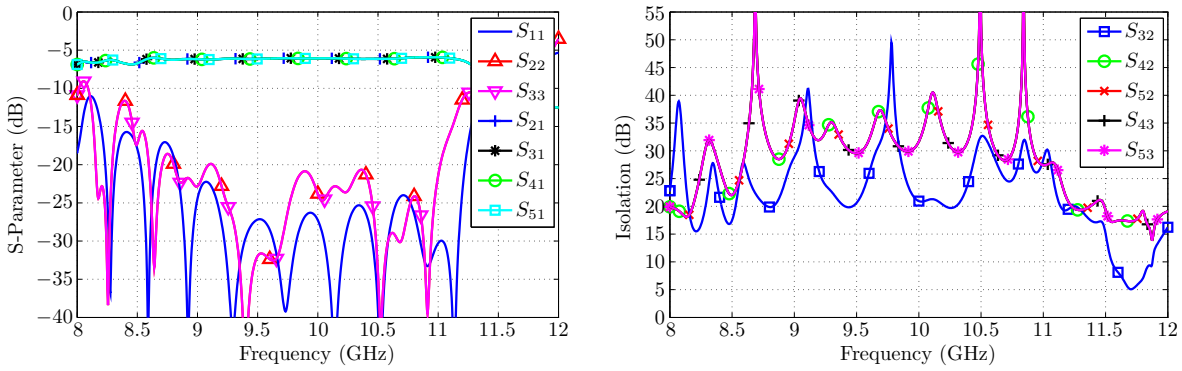


(a) (b)

Figure 3.10: (a) and (b) the full-wave simulated results of the compound power combiner with non-ideal isolation loads.

### 3.4.3 Design 3

The third design example consists of two 4-way microstrip power combiners and broadside coupled-line couplers designed to operate at around 4 GHz. The combiners and couplers used in this design will be modelled by full-wave simulation and will be manufactured and measured in order to validate the new isolation method. The microstrip combiners and couplers will be realised using a printed circuit board (PCB) with a standard 4-layer stackup as shown in Fig. 3.11, where one of the ground planes are omitted so that the two outer layers can be used for microstrip transmission lines with a shared ground plane. The two substrates are bonded together using a single FR-4 prepreg, which will cause the microstrip lines on either side of the PCB to be slightly different from each other. Standard SMA connectors will be used with dielectrics stepped to a diameter of 2.16 mm and center conductors stepped to a diameter of 0.25 mm in order to be compatible with the substrate thickness shown in Fig. 3.11.

The 4-way microstrip power combiner consists of quarterwave matching sections to create an impedance match between the output and input ports. The design of such a combiner

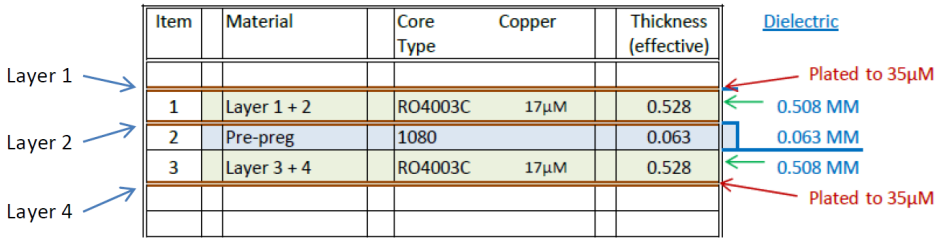


Figure 3.11: The material stackup of the printed circuit board (PCB) used to realise the microstrip combiners and couplers.

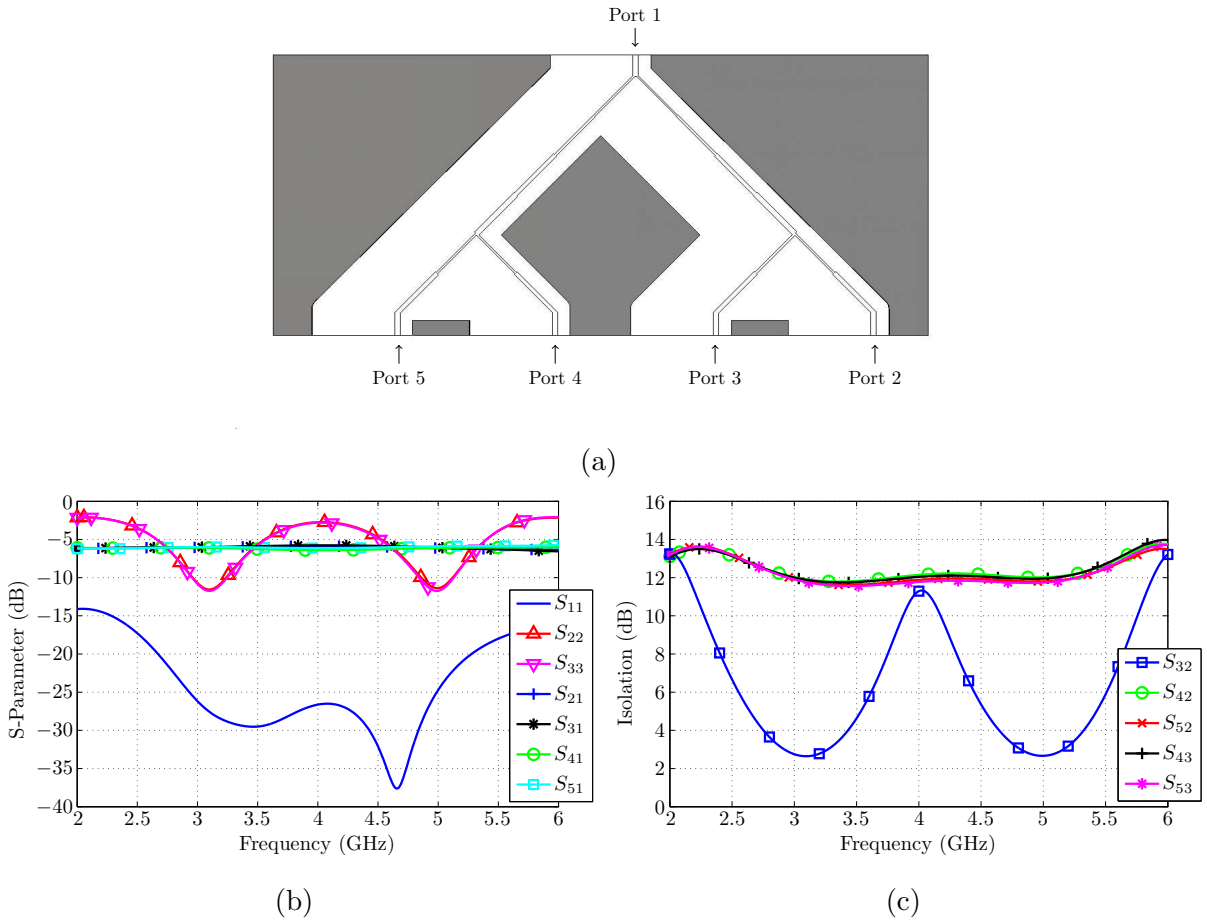


Figure 3.12: (a) A 3D CAD model of the microstrip combiner, and (b) and (c) its full-wave simulated results.

is well-known and will not be discussed here. A 3D CAD model of the combiner is shown in Fig. 3.12(a). Conducting walls are added around the microstrip lines to prevent higher order modes from propagating in the enclosure of the combiner. The walls are designed exactly as they will be used in the final structure where the couplers are added and a mirrored copy of the microstrip combiner will be added on the other side of the PCB. The walls are shorted to ground using vias with a diameter of 1 mm. The full-wave simulated S-parameters including the isolation of the microstrip combiner are shown in Figs. 3.12(b) and 3.12(c). The combiner has a maximum output port reflection coefficient ($S_{11}$) of better than $-25$ dB from 3 to 5 GHz, and a maximum input port reflection coefficient ($S_{22}$) of roughly $-2.5$ dB across the simulated frequency band. The isolation between all the input ports except ports 2 and 3 is roughly 12 dB, and the minimum isolation between ports 2 and 3 is slightly better than 2.5 dB across the frequency band.

The broadside coupled-line coupler is designed using the information presented in [53]. A 3D model of the resulting coupler is shown in Figs. 3.13(a) and 3.13(b). Note that the

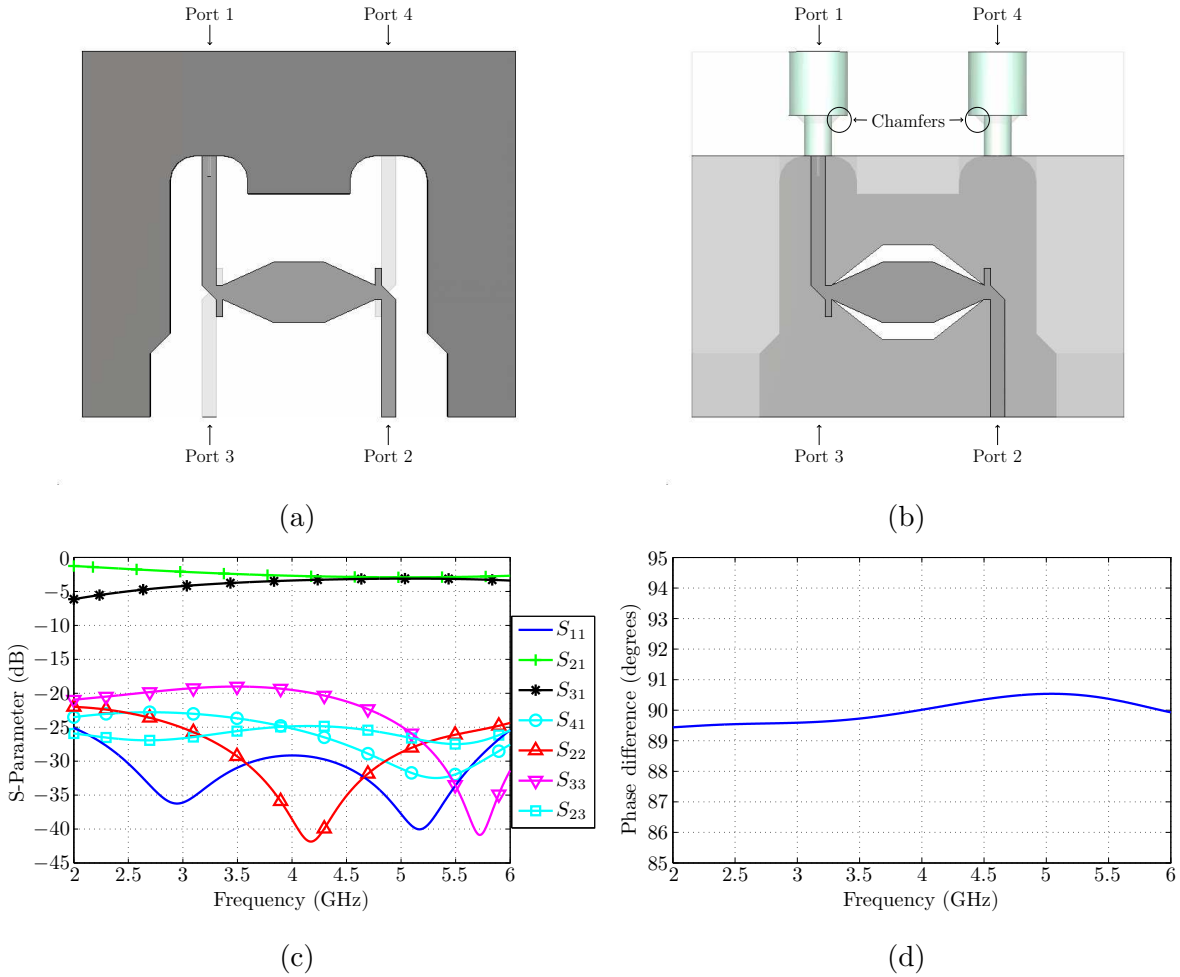


Figure 3.13: Different components in the 3D model of the coupler are shown in (a) and (b), and (c) shows its full-wave simulated results. The phase difference between the coupled port (port 3) and through port (port 2) is shown in (d).

isolation loads of the coupler in this design, and therefore of the compound combiner, are terminations instead of floating isolation resistors. The walls surrounding the coupler are shown in Fig. 3.13(a), as well as the microstrip lines on both outer layers of the PCB. The ground plane with the coupling slot is shown in Fig. 3.13(b) with the microstrip lines and dielectric components of the SMA connectors that will be used. A 45° chamfer of 0.7 mm is added to the outer conductors of each SMA port, as indicated in Fig. 3.13(b), in order to improve the performance of the SMA to microstrip transition. The full-wave simulated S-parameters of the coupler are shown in 3.13(c), and Fig. 3.13(d) shows the phase difference between ports 2 and 3, where a maximum deviation of less than 0.6° from 90° is achieved between 2 and 6 GHz. The coupler has an $S_{11}$ and $S_{41}$ of better than −22 dB from 2 to 6 GHz, and a maximum amplitude difference between ports 2 and 3 of less than 0.8 dB from 4 to 6 GHz. Note that by adding the walls and the SMA input ports on one side, the coupler is no longer symmetrical. The worst-case input port reflection

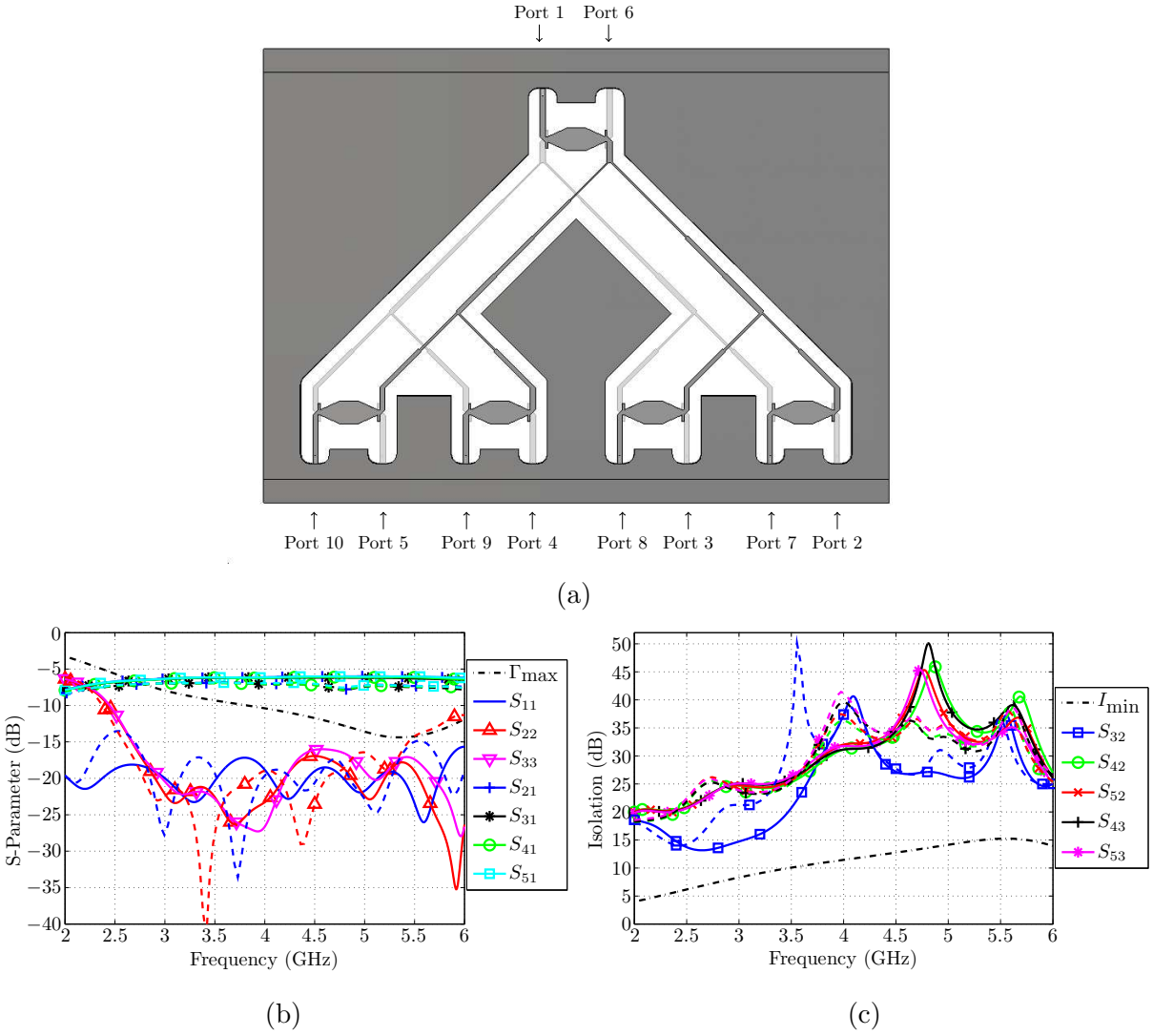


Figure 3.14: (a) A 3D CAD model of the microstrip combiner, and (b) and (c) its full-wave simulated (solid lines) and measured (dashed lines) results. The maximum estimated input port reflection coefficient $\Gamma_{\max}$ is shown in (b), and minimum estimated input port isolation $I_{\min}$ is shown in (c).

coefficient and isolation that the combination of this coupler and the 4-way microstrip combiner may have is thus estimated using (3.29) and (3.33), and shown in Figs. 3.14(b) and 3.14(c). An estimated worst-case input port reflection coefficient and isolation of better than $-10$ dB and 12 dB between 4 and 6 GHz will be achieved, respectively.

After the combiner and coupler designs are completed, the next step is to simply connect the components together in the correct configuration, as shown in Fig. 3.1(a). A 3D model of the resulting structure is shown in Fig. 3.14(a), and its full-wave simulation results are shown in Figs. 3.14(b) and 3.14(c). The simulated output port reflection coefficient ($S_{11}$) is better than $-17$ dB, the input port reflection coefficient ($S_{22}$) is better than $-15$ dB, and the minimum isolation is better than 20 dB from 3.5 to 6 GHz. These results indicate

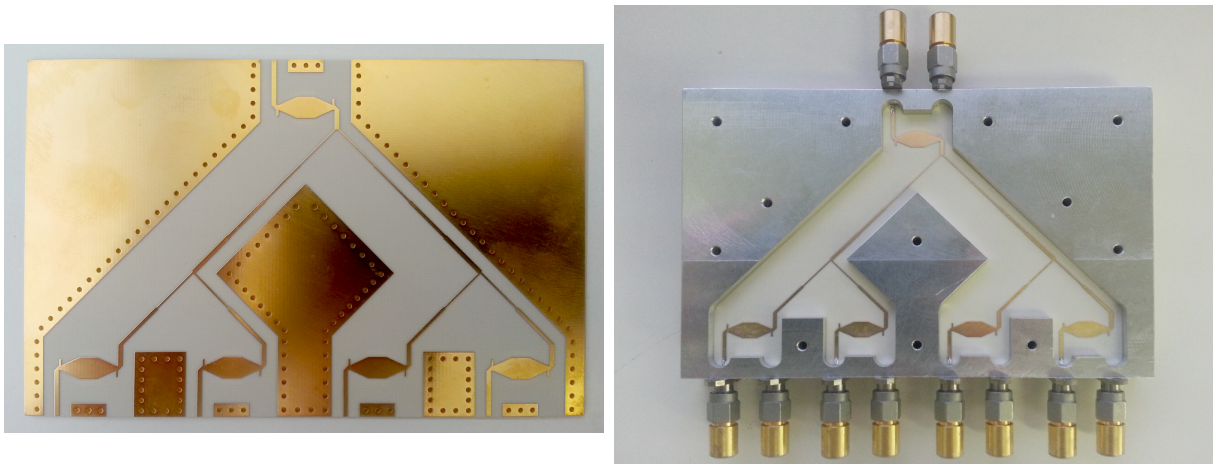

(a) (b)

Figure 3.15: (a) A photo of the manufactured PCB containing the combiners and couplers, and (b) a photo of the PCB sandwiched between the two machined aluminium plates that form the walls that are shorted to ground through vias.

a significant improvement in the input port reflection coefficient and isolation of the microstrip combiner on its own. These simulated results are also in agreement with the estimated worst-case values $I_{\min}$ and $\Gamma_{\max}$.

### 3.4.4 Construction and Measurement of Design 3

The microstrip compound power combiner in design 3 is manufactured and measured. The PCB containing the microstrip combiners and coupled-line couplers is manufactured and shown in Fig. 3.15(a). The port numbering is the same as shown in Fig. 3.14(a). The PCB is sandwiched between two identical machined aluminium plates which form the walls, as shown in Fig. 3.15(b). The walls are shorted to ground through vias with a diameter of 1 mm. The device as shown in Fig. 3.15(b) will look the same when turned over to reveal the microstrip lines on the other side of the PCB. Aluminium covers are added on both sides to form the enclosure of the structure. The measurements of the final structure are shown in Figs. 3.14(b) and 3.14(c) for comparison with the full-wave simulated results. Note that these measurements are performed using non-ideal terminations, as shown in Fig. 3.15(b), with reflection coefficients no better than $-30$ dB for the isolation loads, whereas ideal terminations are used in the full-wave simulations.

## 3.5 Conclusion

The new isolation method presented in this chapter has been proven to work with theoretically any type of power combiner with any number of input ports. A simple method is presented for estimating the worst-case performance that may be achieved given the S-parameters of the individual power combiner and coupler that will be used in the compound power combiner. Three example designs are completed with simulated results and one is manufactured and measured to confirm the validity of the new isolation method. The new isolation method presented in this chapter offers a means to realise an arbitrary reciprocal $N$-way power combiner with matched and isolated input ports using a simple design method, where terminations can be used for the isolation loads. The new isolation method is presented in [16].

# Chapter 4

# Conclusion

A circuit-based design technique that leads to benefits in terms of the physical size, manufacturability, and flexibility in the design of conical line power combiners is presented in this dissertation. Additionally, a new method is presented that can be used in general to improve the input port isolation of power combiners, including reactive power combiners, without affecting their reciprocity.

An equivalent model is extracted in order to analyse the effect of the tuning posts in the input ports of previous conical combiner designs. It is shown that the tuning posts effectively reduce the inductance and result in a much improved reflection coefficient compared to the shorted feeding pin input port transition. However, the shorted feeding pin is chosen over the tuning post in order to simplify the manufacturing of the combiner. After the extraction of empirical equations for the equivalent circuit model, it is demonstrated that the inductance of the shorted feeding pins can be compensated for in other parts of the combiner and similar performance compared to previous designs can be achieved, while also achieving a significant reduction in physical size. The design of conical combiners is further improved by replacing the section of impedance tapered conical transmission line, which was required in order to increase the spacing in the central output port transition, as well as the coaxial stepped impedance matching sections or tapers in previous designs by a single impedance tapered conical to coaxial transition.

A total of three 10-way X-band conical combiners are manufactured and measured with significantly smaller diameters compared to the previous designs found in literature. The first combiner is designed using only the equivalent circuit model and empirical equations without the need for any full-wave simulations except for one in order to validate the design before being manufactured. An output port reflection coefficient of better than $-18$ dB with a bandwidth of 46% is achieved with a diameter of 49.8 mm. The second combiner utilized the single-section impedance tapered conical to coaxial transition and is designed

using the equivalent circuit model and empirical equations. An output port reflection coefficient of better than $-23$ dB over a bandwidth of 20% is achieved with a diameter of 51.8 mm. The third combiner utilized the multi-section impedance tapered conical to coaxial transition and is also designed using the equivalent circuit model and empirical equations. A reflection coefficient of better than $-17$ dB over a bandwidth of 43% was achieved with a diameter of 59.2 mm. This design demonstrates that the bandwidth that was lost in the single-section transition design can be recovered by adding optimizable degrees of freedom to the design of the transition.

The new isolation method is described followed by a proof based on S-parameters to show that the method can be used in general to improve the isolation of power combiners, and allow terminations to be used for isolation loads. Equations are derived that may be used to calculate worst-case performance estimates given the parameters of the power combiner and coupler used in the design. A simple design method is presented, followed by three design examples with three different combiner and coupler technologies using full-wave simulations. The final design, which is based on microstrip transmission lines and broadside coupled line couplers, is manufactured and measured. A much improved input port reflection and isolation performance of $-15$ dB and 20 dB is achieved, respectively, compared to an input port reflection coefficient of $-2.5$ dB and isolation of 2.5 dB before the isolation was improved.

Possible expansions on this work may include:

- Extracting empirical equations for the peripheral feeding ports of conical combiners with tuning posts, so that the circuit model based design method can be used for combiners with these types of input ports.
- Using the impedance tapered conical to coaxial transition to reduce the size of coaxial power combiners. This could be done by designing a transition from the coaxial output line to a conical transmission line with $\theta_2 = 90^\circ$ followed by a slightly modified version of the transition that bends the other way to a larger coaxial transmission line with a large enough radius to accommodate the input ports.
- The implementation of a high power SSPA using conical line power combiners.
- Integrating the new isolation method into various high performance power combiners which currently have poor input port isolation, such as the conical line power combiner.
- Constructing an antenna array feed utilizing the new isolation method to demonstrate any improvement in terms of power handling, input port impedance and radiation pattern that may be achieved by the antenna system.

# Bibliography

[1] J. P. Quine, J. G. McMullen, and D. D. Khandelwal, "Ku-Band IMPATT amplifiers and power combiners," in *Microwave Symposium Digest, 1978 IEEE-MTT-S International*, June 1978, pp. 346–348.

[2] R. S. Harp and K. J. Russel, "Conical power combiner," U.S. Patent 4 188 590, Feb. 1980.

[3] D. I. L. de Villiers, P. W. van der Walt, and P. Meyer, "Design of a ten-way conical transmission line power combiner," *Microwave Theory and Techniques, IEEE Transactions on*, vol. 55, no. 2, pp. 302–308, Feb. 2007.

[4] D. I. L. de Villiers, P. W. van der Walt, and P. Meyer, "Design of conical transmission line power combiners using tapered line matching sections," *Microwave Theory and Techniques, IEEE Transactions on*, vol. 56, no. 6, pp. 1478–1484, June 2008.

[5] E. J. Wilkinson, "An N-way hybrid power divider," *Microwave Theory and Techniques, IRE Transactions on*, vol. 8, no. 1, pp. 116–118, Jan. 1960.

[6] U. H. Gysel, "A new N-way power divider/combiner suitable for high-power applications," in *Microwave Symposium, 1975 IEEE-MTT-S International*, May 1975, pp. 116–118.

[7] A. E. Fathy, S.-W. Lee, and D. Kalokitis, "A simplified design approach for radial power combiners," *Microwave Theory and Techniques, IEEE Transactions on*, vol. 54, no. 1, pp. 247–255, Jan. 2006.

[8] D. S. Beyragh, S. Abnavi, and S. R. Motahari, "Implementation of N-way Gysel combiners using back to back microstrip structure," in *Ultra-Wideband (ICUWB), 2010 IEEE International Conference on*, Sept. 2010, vol. 2, pp. 1–4.

[9] M. H. Chen, "A 19-way isolated power divider via the $TE_{01}$ circular waveguide mode transition," in *Microwwave Symposium Digest, 1986 IEEE MTT-S International*, June 1986, pp. 511–513.

[10] A. A. M. Saleh, "Planar multiport quadrature-like power dividers/combiners," *Microwave Theory and Techniques, IEEE Transactions on*, vol. 29, no. 4, pp. 332–337, Apr. 1981.

[11] A. A. M. Saleh, "Improving the graceful-degradation performance of combined power amplifiers," *Microwave Theory and Techniques, IEEE Transactions on*, vol. 28, no. 10, pp. 1068–1070, Oct. 1980.

[12] R. D. Beyers and D. I. L. de Villiers, "Analysis of shorted coaxial peripheral feeding networks for conical line power combiners," in *Microwave Conference Proceedings (APMC), 2013 Asia-Pacific*, Nov. 2013, pp. 285–287.

[13] R. D. Beyers and D. I. L. de Villiers, "Compact conical-line power combiner design using circuit models," *Microwave Theory and Techniques, IEEE Transactions on*, vol. 62, no. 11, pp. 2650–2658, Nov. 2014.

[14] R. D. Beyers and D. I. L. de Villiers, "Design and analysis of an impedance tapered conical to coaxial transmission line transition," *Microwave Conference Proceedings (EUMC), 2014 European*, Oct. 2014, pp. 307-310.

[15] R. D. Beyers and D. I. L. de Villiers, "A general conical to coaxial transmission line transition," *to be submitted, IEEE Microwave and Wireless Components Letters.*

[16] R. D. Beyers and D. I. L. de Villiers, "A general input port isolation network for $N$-way power combiners/dividers," *accepted, International Microwave Symposium 2015.*

[17] K. Takagi *et. al*, "Ku-band AlGaN/GaN HEMT with over 30W," in *Microwave Integrated Circuit Conference (EuMIC), 2007 European*, Oct. 2007, pp. 169–172.

[18] K. Kanto *et. al*, "An X-band 250W solid-state power amplifier using GaN power HEMTs," in *Radio Wireless Symposium, 2008 IEEE*, Jan. 2008, pp. 77–80.

[19] H. Shigematsu *et. al*, "C-band 340-W and X-band 100-W GaN power amplifiers with over 50-% PAE," in *Microwave Symposium Digest, 2009 IEEE MTT-S International*, June 2009, pp. 1265–1268.

[20] M. Nishihara *et. al*, "X-band 200W AlGaN/GaN HEMT for high power application," in *Microwave Integrated Circuits Conference (EuMIC), 2011 European*, Oct. 2011, pp. 65–68.

[21] H. Noto *et. al*, "X- and Ku-band internally matched GaN amplifiers with more than 100W output power," in *Microwave Conference (EuMC), 2012 42nd European*, Oct. 2012, pp. 1075–1078.

[22] H. Ashoka *et. al*, "An X-band 2 kW CW GaAs FET power amplifier for continuous wave illuminator application," in *Microwave Symposium Digest, 1998 IEEE MTT-S International*, June 1998, vol. 2, pp. 1149–1152

[23] K. J. Russell, "Microwave power combining techniques," *Microwave Theory and Techniques, IEEE Transactions on*, vol. 27, no. 5, pp. 472–478, May 1979.

[24] R. A. York, "Some considerations for optimal efficiency and low noise in large power combiners," *Microwave Theory and Techniques, IEEE Transactions on*, vol. 49, no. 8, pp. 1477–1482, Aug. 2001.

[25] M. E. Bialkowski and V. P. Waris, "Electromagnetic model of a planar radial-waveguide divider/combiner incorporating probes," *Microwave Theory and Techniques, IEEE Transactions on*, vol. 41, no. 6, pp. 1126–1134, June 1993.

[26] T.-I. Hsu and M. D. Simonutti, "A wideband 60 GHz 16-way power divider/combiner network," in *Microwave Symposium Digest, 1984 IEEE MTT-S International*, May 1984, pp. 175–177.

[27] S. Nogi, F. Okazaki, and K. Fukui, "A broadband conical-radial wave power divider/combiner," in *Microwave Conference Proceedings (APMC), 1994 Asia-Pacific*, Dec. 1994, pp. 507–510.

[28] J.-P. Fraysse *et. al*, "A 20W Ka-band radial solid-state power amplifier with 20% associated power-added efficiency," in *Microwave Conference (EuMC), 2013 European*, Oct. 2013, pp. 688–691.

[29] K. Song, F. Zhang, S. Hu, and Y. Fan, "Ku-band 200-W pulsed power amplifier based on waveguide spatially power-combining technique for industrial applications," *Industrial Electronics, IEEE Transactions on*, vol. 61, no. 8, pp. 4274–4280, Aug. 2014.

[30] M. Amjadi and E. Jafari, "Design of a Broadband Eight-Way Coaxial Waveguide Power Combiner," *Microwave Theory and Techniques, IEEE Transactions on*, vol. 60, no. 1, pp. 39–45, Nov. 2012.

[31] R. Lehmensiek and P. W. van der Walt, "A compact, high-power, low-loss, L-band coaxial 18-way power divider/combiner," *Microwave and Optical Technology Letters*, vol. 16, no. 4, pp. 241–243, Nov. 1997.

[32] Q. Xue, K. Song, and C.-H. Chan, "China: Power combiners/dividers," *Microwave Magazine, IEEE*, vol. 12, no. 3, pp. 96–106, May 2011.

[33] P. W. der Walt, "A novel matched conical line to coaxial line transition," in *Communications and Signal Processing (COMSIG), Proceedings of the 1998 South African Symposium*, Sept. 1998, pp. 431–434.

[34] D. I. L. de Villiers, "Analysis and design of conical transmission line power combiners," Ph.D. dissertation, Department of Electrical and Electronic Engineering, Stellenbosch University, Stellenbosch, South Africa, 2007.

[35] D. I. L. de Villiers, P. W. van der Walt, and P. Meyer, "Design constraints in conical line power combiners," in *Microwave Symposium (MMS), 2010 Mediterrean*, Aug. 2010, pp. 148–151.

[36] D. I. L. de Villiers, "Higher order modal interactions in conical power combiners," in *Electromagnetics in Advanced Applications (ICEAA), 2012 International Conference on*, Sept. 2012, pp. 345–348.

[37] D. I. L. de Villiers and R. D. Beyers "Comments on "ultra-wideband ring-cavity multiple-way parallel power divider"," in *Industrial Electronics, IEEE Transactions on, submitted*.

[38] D. I. L. de Villiers and P. Meyer, "Numerical calculation of analytical solutions for higher order modes in conical lines," *RF and Microwave Computer-Aided Engineering, International Journal of*, vol. 19, pp. 99–109, Jan. 2009.

[39] R. W. Klopfenstein, "A transmission line taper of improved design," *Proceedings of the IRE*, vol. 44, no. 1, pp. 31–35, Jan. 1956.

[40] G. W. Swift and D. I. Stones, "A comprehensive design technique for the radial wave power combiner," in *Microwave Symposium Digest, 1988 IEEE MTT-S International*, May 1988, vol. 1, pp. 279–281.

[41] K. Song and Q. Xue, "Planar probe coaxial-waveguide power combiner/divider," *Microwave Theory and Techniques, IEEE Transactions on*, vol. 57, no. 11, pp. 2761–2767, Nov. 2009.

[42] K. Song and Q. Xue, "Ultra-wideband ring-cavity multiple-way parallel power divider," *Industrial Electronics, IEEE Transactions on*, vol. 60, no. 10, pp. 4737–4745, Oct. 2013.

[43] J. Whinnery, H. Jamieson, T. Robbins, "Coaxial-line discontinuities," *Proceedings of the IRE*, vol. 32, no. 11, pp. 695–709, Nov. 1944.

[44] G. Kwan and N. Das, "Coaxial-probe to parallel-plate dielectric waveguide transition: analysis and experiment," *Microwave Symposium Digest, 1998 IEEE MTT-S International*, Jun. 1998.

[45] R. P. Hecken, "A near-optimum matching section without discontinuities," *Microwave Theory and Techniques, IEEE Transactions on*, vol. 20, no. 11, pp. 734–739, Nov. 1972.

[46] Computer Simulation Technology, CST Studio Suite 2011, Darmstadt, Germany. [Online]. Available: http://www.cst.com

[47] J. A. Nelder and R. Mead, "A simplex method for function minimization," *Computer Journal*, vol. 7, no. 4, pp. 308–313, 1965. [Online]. Available http://comjnl.oxfordjournals.org/content/7/4/308.abstract

[48] J. W. Bandler, R. Biernacki, S. H. Chen, P. A. Grobelny, and R. H. Hemmers, "Space mapping technique for electromagnetic optimization," *Microwave Theory and Techniques, IEEE Transactions on*, vol. 42, no. 12, pp. 2536–2544, Dec. 1994.

[49] P. I. Somlo, "The computation of coaxial line step capacitances," *Microwave Theory and Techniques, IEEE Transactions on*, vol. 15, no. 1, pp. 48–53, Jan. 1967.

[50] G. Luzzatto, "An N-way hybrid combiner," *Proceedings of the IEEE*, vol. 55, no. 3, pp. 470–471, Mar. 1967.

[51] J. Yao and S. Bo, "Mirrored coupling structures for microwave signal splitting and combining," *Microwave Theory and Techniques, IEEE Transactions on*, vol. 61, no. 10, pp. 3551–3557, Oct. 2013.

[52] A. Clavin, "High-power ferrite load isolators," *Microwave Theory and Techniques, IRE Transactions on*, vol. 3, no. 5, pp. 38–43, Oct. 1955.

[53] C.-H. Mou and C.-H. Tseng, "A new passive isolation component using slot-coupled microstrip lines for simultaneously transmitting and receiving applications," in *Microwave Conference Proceedings (APMC), 2012 Asia-Pacific*, Dec. 2012, pp. 1193–1195.

[54] A. A. M. Saleh, "Theorems on match and isolation in multiport networks (Short Papers)," *Microwave Theory and Techniques, IEEE Transactions on*, vol. 28, no. 4, pp. 428–429, Apr. 1980.

[55] G. R. Simpson, "A generalized n-port cascade connection," in *Microwave Symposium Digest, 1981 IEEE MTT-S International*, June 1981, pp. 507–509.

[56] H. J. Riblet, "The short-slot hybrid junction," *Proceedings of the IRE*, vol. 40, no. 2, pp. 180–184, Feb. 1952.

[57] T. Stander, P. W. van der Walt, P. Meyer, and W. Steyn, "A comparison of simple low-power wedge-type X-band waveguide absorbing load implementations," in *AFRICON 2007*, Sept. 2007, pp. 1–4.